# STUDY OF CONVECTIVE DIFFUSIVE IRREVERSIBILITY IN REVERSING CHAOTIC AND NON-CHAOTIC STOKES FLOWS

A Dissertation

Presented to the Faculty of the Graduate School

of Cornell University

In Partial Fulfillment of the Requirements for the Degree of

Doctor of Philosophy

by

Pavithra Sundararajan

Aug 2016

# STUDY OF CONVECTIVE DIFFUSIVE IRREVERSIBILITY IN REVERSING CHAOTIC AND NON-CHAOTIC STOKES FLOWS

Pavithra Sundararajan, Ph. D.

Cornell University 2016

We revisit the classic reversibility experiment of G.I. Taylor in Stokes flow and the long standing debate on the role of chaos in controlling the loss of reversibility of trajectories. The central technical advance of our work is the introduction of a theoretical framework with which to extract and compare rate-independent properties of the reversal process in equivalent chaotic and non-chaotic flows with well-defined levels of tracer diffusivity. This approach allows us to elucidate a significant unity in the evolution of reversibility across both chaotic and non-chaotic flows: i) all linear flows lead to a universal decay of reversibility when viewed in an appropriately scaled time domain, and ii) a simple analysis that accounts for the distribution of strain rates successfully captures the decay in both chaotic and non-chaotic, nonlinear flows. We further show that, in the limit of infinitesimal diffusivity, a qualitative distinction between chaotic and non-chaotic flows does emerge, with a complete loss of sensitivity of reversibility to differences in the strength of diffusive noise for the chaotic case. We discuss these insights in the context of the broader debate on chaos and reversibility and of a technological solution to separation of diffusive solutes that could benefit from this understanding. We translate the application of our theoretical framework for studying reversing time dependent two dimensional chaotic and non-

chaotic flows to three-dimensional chaotic and non-chaotic flows with fore-aft symmetry. We explored the impact of flow characteristics and inlet conditions on convective diffusive irreversibility in the context of utilizing the three dimensional model system for separation of pair of diffusive solutes. We experimentally show proof of concept of convective-diffusive irreversibility by implementing the reversal process in a microchannel with fore-aft symmetrical grooves. We explore inertial reversibility in the chaotic and non-chaotic flows experimentally and discuss the manifestation of inertial irreversibility as a function of Re. Finally, we compare and contrast the convective diffusive irreversibility in a forward mixing flow and a reversal flow using the established theoretical framework and test its ability to predict mixing characteristics.

# BIOGRAPHICAL SKETCH

Pavithra Sundararajan was born on 25th September 1984, in Tiruchirapalli, Tamil Nadu, India. She spent her early childhood in Chennai, before going back to Tiruchirapalli for the next decade of her life. Prof. Hemalatha Thiagarajan, Dr. N Rajagopal and Dr. Pattabhiraman sharpened her interest and knowledge in the fields of science and engineering. She went on to obtain her Bachelors of Technology in mechanical engineering at the Indian Institute of Technology in Madras. She joined the MS/Ph.D program in Mechanical and Aerospace Engineering at Cornell University. Prof. Abraham Stroock and Prof. Donald Koch advised and guided her throughout her Ph.D. She will always be grateful to Cornell University for the wonderful opportunites and academically and socially active environment.

Dedicated to her parents, Dr. N Sundararajan and Mrs. Rajni Sundararajan

# ACKNOWLEDGMENTS

We acknowledge support from the National Science Foundation (CTS-0529042) and the Department of Energy (DE-FG02-05ER46250). This research was conducted using the resources of the Cornell Center for Advanced Computing, which receives funding from Cornell University, the National Science Foundation, and other leading public agencies, foundations, and corporations. We thank Dr. Scott Verbridge and Dr. Emmanuel Villermaux for valuable suggestions.

Device microfabrication was performed in part at the Cornell NanoScale Facility, a member of the National Nanotechnology Infrastructure Network, which is supported by the National Science Foundation (Grant ECS-0335765). We also acknowledge the fabrication support from Lurie Nanofabrication Facility at the University of Michigan, and the Penn State University Nanofabrication facility. We thank Dr. Warren Zipfel, Dr. Rebecca Williams, Dr. Johanna Cruz, Dr. Kevin Hurtz and Glen Swann for technical support in experiments.

## TABLE OF CONTENTS

LIST OF FIGURES

**Chapter1**

**Chapter 2**

Fig 2: Separation by convective diffusive irreversibility (SCDI) (SCDI) in model two-dimensional linear flows (a,b) Chaotic and non-chaotic laminar flows realized using Baker's transformation, idealized stirring processes achieved with repeated sequences of (i) deformation in a linear flow, (ii) cutting, and (iii) reassembly. Pure extension captures the characteristic exponential stretching that occurs in chaotic flows (a). Simple shear captures the power law stretching observed in non-chaotic flows (b). (c) The same initial concentration distribution of a diffusive solute (red) in (a, b) is represented in the Lagrangian frame of reference of the strand $(x', y')$. (d) Concentration profile $c(\xi,\tau)$ predicted by the Ranz model (solution to equation 10) initially ($\tau = 0$; blue curve), after stirring, ( $\tau_{stir} = 0.02$ ; green curve), and after unstirring ($\tau_{unstir} = 0.04$ ; red curve)

**Chapter 3**

**Chapter 4**

# INTRODUCTION

Many large scale natural transport phenomena occur in turbulent systems. However, several industrial processes use laminar transport theory because the dimensions of these packed columns, boundary regions of macroscopic systems, analytical instruments are small. The fate of micro scale systems and macroscopic systems with small characteristic dimension is strongly tied with advances of transport in laminar flows in the direction of making them faster and efficient. One means to approach the goal of improving transport processes in laminar flows emerged in the 1960's when V.I. Arnold [1] identified a class of steady, three-dimensional flows in which the trajectories of fluid elements displayed chaotic dynamics [2]. Subsequently, H. Aref [3] clarified the relationship between these chaotic trajectories in a flow and showed that time-dependent, two-dimensional flows could also exhibit chaos. The hallmark of dynamical chaos is the so-called sensitivity to initial conditions, or, more precisely, the exponential separation in time of neighboring trajectories in the dynamical phase spaces [4]. Another characteristic of chaos is its ergodicity, as observed in the Poincare maps of chaotic flows; a trajectory in an ergodic system has the tendency to visit within a very small neighborhood of all points in the chaotic phase space. These characteristics make chaotic laminar flows a very ideal candidate for mixing [5] and mass transport. A problem closely related to mixing is separation. Aref and Jones, followed the work of Heller [6] and Taylor [7] on coupling of time reversibility of Stokes flows and diffusive irreversibility, to propose a separation technique utilizing the exponential stretching character of chaos [8]. This study by Aref and Jones holds the motivation for the work presented here.

Chaos and irreversibility have been tied together since the time of Boltzmann, with the proposal of the assumption of molecular chaos resulting in the arrow of time, and breaking symmetry. However, since then, Prigogine and others have proposed that even deterministic low dimensional chaos is source of irreversibility [9]. Further, the work by Gaspard shows that chaotic systems like the multi-baker's map exhibits loss of time correlation and diffusive-like dynamics, when running forward in time [10]. On the other hand, chaos is not intrinsically irreversible, in that, with infinite precision and in the absence of sources of random noise, chaotic trajectories will return to their original locations in phase space if the dynamics is reversed [11]. It is here that Stokes flows, which exhibit reversibility due to the linearity and quasi steady nature of the governing equation and reversible boundary conditions, could prove to be a valuable tool in the study of reversibility and chaos. These flows provide the opportunity to test if for chaotic Stokes flow, the sensitivity to initial conditions and exponential divergence of fluid trajectories, are sufficient to ensure irreversibility [12], such that the original state of scalar field, even in the limit of zero diffusion, can never be restored by un-stirring once it is chaotically stirred. In this definition, stirring is the effect of the flow alone, whereas mixing is the result of action of stirring and diffusion together.

In this thesis, we address the following challenges in the context of reversibility and chaos in a structured manner in the three chapters. The first chapter focuses on deriving the fundamental links between low dimensional chaos and reversibility. We clarify the notion of irreversibility associated with the rate of a chaotic process, i.e. chaos is irreversible because it amplifies any small error exponentially fast. We then shift the focus to understanding the link between chaos and irreversibility in two ways: by using a rate independent observable, and by rescaling the dynamics to treat all processes, chaotic and non-chaotic in on the same ground with respect to

irreversibility. We choose diffusion as the source of irreversibility and study the impact of chaos on reversibility. We find an interesting interplay between the sensitivity and the ergodicity of chaos in the limit of infinitesimal diffusion.

The second chapter focuses on the application of the linear flow model, first introduced by Ranz to general three-dimensional duct flows to study the reversal process, in the context of separation. We focus on extensive treatment of the reversal process by developing modifications to the model under different conditions. For describing the influence of chaotic and non-chaotic flows on reversibility and separation, we find that there are few important characteristics: a) identifying the local linear flow in these general non-linear flows, b) presence of distribution of strain rates, c) ergodicity of flow. Additionally, guidelines for implementing a passive continuous separation device in practice are discussed.

The third chapter focuses on the experimental implementation of reversal process with a promise of technological impact in the context of separation of solutes based on differences in their diffusivity. The highlight of these experiments is the strategy of implementation of reversal in a microchannel: we employ fore-aft symmetry to reverse only the transverse flow during un-stirring while allowing unidirectional axial flow. We explored inertial reversibility in the chaotic and non-chaotic flows experimentally to identify the limiting Reynolds number for the Stokes approximation and discuss the manifestation of inertial irreversibility as a function of Re. We conclude with identification of a chaotic mixer that could make this technique of separation an attractive strategy to achieve fast separation, in a short length scale, with a high separation efficiency and yield.

In the final chapter, we focus on the key finding of our adaptation of the Ranz model: is that the reversal process (stirring and un-stirring diffusive solutes) is an equivalent mixing process (combined action of stirring and diffusion). We attempt to capture the mixing characteristics in the two classes of flows. Our adaptation of a linear flow model captures the average characteristics of chaotic and non-chaotic flows, but failure to include the non-linear processes prevents it from capturing the details of the mixing process in a chaotic flow.

**References**


[1] V. I. Arnold, and A. Avez, *Ergodic Problems of Classical Mechanics* (Addison-Wesley, Boston, 1968),

[2] T. Dombre, U. Frisch, J. M. Greene, M. Henon, A. Mehr, and A. M. Soward, Journal of Fluid Mechanics **167**, 353 (1986).

[3] H. Aref, Journal of Fluid Mechanics **143**, 1 (1984).

[4] S. H. Strogatz, *Nonlinear Dynamics And Chaos: With Applications To Physics, Biology, Chemistry, And Engineering* (Westview Press, Cambridge, MA, 2001),

[5] A. D. Stroock, S. K. W. Dertinger, A. Ajdari, I. Mezic, H. A. Stone, and G. M. Whitesides, Science **295**, 647 (2002).

[6] J. P. Heller, American Journal of Physics **28**, 348 (1960).

[7] G. I. Taylor, *Illustrated Experiments in Fluid Mechanics* (MIT Press Cambridge, 1972), p.47-54.

[8] H. Aref, and S. W. Jones, Physics of Fluids A-Fluid Dynamics **1**, 470 (1989).

[9] B. Misra, I. Prigogine, and M. Courbage, Proceedings of the National Academy of Sciences of the United States of America **76**, 3607 (1979).

[10] P. Gaspard, *Chaos, scattering and statistical mechanics* (Cambridge Univ. Press, New York, 1998), p.250-253.

[11] D. Levesque, and L. Verlet, Journal of Statistical Physics **72**, 519 (1993).

[12] J. Gollub, and D. Pine, Physics Today **59**, 8 (2006).

# CHAPTER 1

# IMPACT OF CHAOS AND BROWNIAN DIFFUSION ON IRREVERSIBILITY IN STOKES FLOWS

## *Introduction*

A debate persists on whether dynamical chaos is the origin of irreversibility in the contexts of statistical mechanics [1-2] and transport phenomena [3-4]. On the one hand, running forward in time, chaotic systems, like the multi-baker mapping exhibit loss of time correlation and diffusive-like dynamics [5]. On the other hand, chaos is not intrinsically irreversible, in that, with infinite precision and in the absence of sources of random noise, chaotic trajectories will return to their original locations in phase space if the dynamics is reversed [6]. Experimental studies indicate that non-Brownian spheres in oscillatory shear exhibit irreversible chaotic dynamics [3-4], but the relative importance of chaos and solid body contacts in preventing Stokes flow reversibility in these systems is not clear [7]. A challenge in defining the impact of chaos on irreversibility arises from the well-appreciated fact that chaotic flows accelerate the loss of reversibility in the presence of noise or finite precision relative to non-chaotic flows. In this Letter, we adapt an analytical treatment of mixing (simultaneous convection and diffusion) put forth by Ranz [8] to scale the dynamics of diffusive tracers in a reversal experiment with respect to the characteristic rate of mixing. This approach elucidates a unity in the evolution of convective diffusive irreversibility in all linear flows and shows how this unity is disrupted by the presence of the distribution of strain rates in both chaotic and non-chaotic flows.

The reversal experiment that we consider is based on Heller's proposal [9-10] to use diffusive irreversibility in time-reversible Stokes flows as a means to separate solutes of distinct Brownian diffusivity from a mixture.

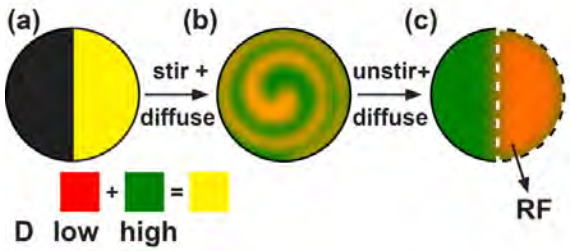


**Fig. 1:** Schematic representation of Separation by Convective Diffusive Irreversibility (SCDI). Concentration profiles of a one-to-one mixture (yellow) of two solutes of different diffusivities (green = high diffusivity, red = low diffusivity) **(a-c)** State of mixture (a) initially segregated from miscible carrier fluid (black) before stirring, (b) after stirring in a Stokes flow and (c) after reversing the flow ("unstirring"). The white dashed line in (c) represents the original volume occupied by the mixture in which return fraction *RF* is evaluated.

Figure 1 illustrates his proposal for a mixture of two solutes: i) stir the mixture [yellow region in Fig.1 (a)] until the distribution of the solute with higher diffusivity (green) has been largely homogenized into a carrier fluid [black region in Fig.1 (a)], ii) "unstir" (reverse the flow) to completely undo the deformation [Fig.1(c)], and iii) collect the fluid from the original volume. The collected fluid will be partially purified of the tracers of higher diffusivity. We call this process separation by convective diffusive irreversibility, SCDI. In considering SCDI, Aref and Jones [11] defined return fraction *RF* – the fraction of diffusive tracers that return to the original volume [Fig.1(c)] – as a measure of reversibility. They showed that *RF* decays faster in chaotic flows relative to non-chaotic flows for any amplitude of diffusivity and concluded that chaotic dynamics could, in this sense, enhance separation of diffusive solutes. Ottino [12] and others [13] have demonstrated experimentally this acceleration of the decay of reversibility by chaotic dynamics.

We now extend this investigation to ask further how chaotic flows impact the efficiency of SCDI relative to pure diffusion and non-chaotic flows. For this purpose, we define the maximum differential reversibility:

$$\phi\left(D_{high}, D_{low}\right) = Max\left(\frac{RF\left(t_{stir}, D_{low}\right)}{RF\left(t_{stir}, D_{high}\right)}\right)_{\forall t_{stir}} . \qquad \ldots 1$$

This function is the maximum ratio of return fractions of tracers of distinct diffusivities $D_{high}$ and $D_{low}$ with respect to stirring time. This differential reversibility measures the sensitivity of reversal to differences in diffusive noise (a higher value of $\phi$ indicates greater sensitivity) and can serve as a figure of merit for its efficiency for SCDI; $\phi$ also provides a rate independent observable with which to compare the reversal process in the presence and absence of chaos.

***Model***

To pursue this question, we first consider SCDI in three simple cases – (i) no flow such that the tracers evolve by pure diffusion; (ii) pure extensional flow such that the fluid undergoes deformation at an exponential rate; and (iii) simple shear flow such that the fluid undergoes deformation at an algebraic rate. Pure extension and simple shear are

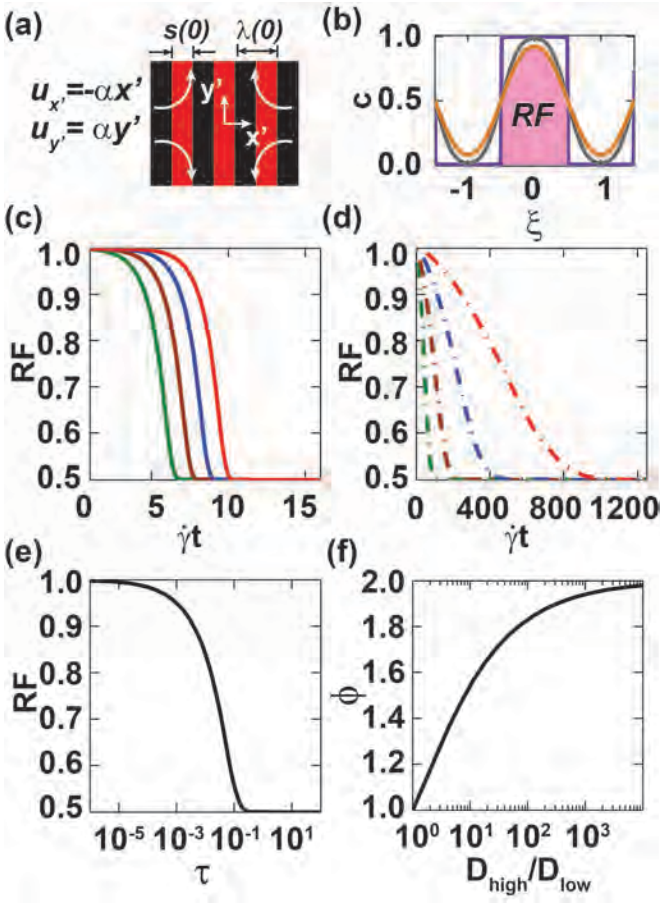


**Fig.2** SCDI in linear flows. **(a)** Initial concentration distribution of a diffusive solute (red) in the frame of reference of the strand $(x', y')$. **(b)** Concentration profile $c(\xi, \tau)$ predicted by the Ranz model [Eq. (5)] initially ( $\tau = 0$; violet curve), after stirring, ( $\tau_{stir} = 0.02$ ; gray curve), and after unstirring ( $\tau_{unstir} = 0.04$ ; orange curve). Return fraction $RF$ is defined as the area of shaded region. **(c-d)** Decay of $RF$ for (c) extension (solid lines) and (d) simple shear (dash dot lines) as a function of total strain, $\dot{\gamma}t$, for four different diffusivities (green – $5.7 \times 10^{-7}$, brown – $5.7 \times 10^{-8}$, blue – $5.7 \times 10^{-9}$, red – $5.7 \times 10^{-10}$). **(e)** The master return curve $RF(\tau_{stir})$ for all linear flows and pure diffusion. **(f)** The master curve of maximum differential reversibility, $\phi$ [Eq. (1)] for all linear flows plotted as a function of the ratio of diffusivities.

linear flows [14]. The work of Ranz [8] indicates that, for weak diffusion, mixing of a periodic array of bands of solute in linear flows [Fig. 2(a)] can capture mixing in the more general nonlinear flows because 1) the folding by a general flow typically results in an approximate

spatial periodicity $(\lambda)$ in the concentration field over short distances, and 2) the flow is approximately linear over short distances. In the case of pure extension, the evolution of these periodic strands represent mixing by the baker's transformation, a canonical model of chaotic dynamics [15]. These strands, when observed in the local frame of reference $(x', y')$ [Fig. 2(a); in which we translate and rotate with the strand] experience an effective rate of extension along $y'$ of $\alpha(t,\dot{\gamma}) = -d\ln[(s(t)/s(0))]/dt$ where $s(t)$ is the width of the strand at time $t$ and $\dot{\gamma}$ is the actual strain rate in the flow. For simple shear flow, $\alpha = \dot{\gamma}^2 t/\left[1+(\dot{\gamma}t)^2\right]$ and for extensional flow, $\alpha = \dot{\gamma}$. In this local frame $(x', y')$, the convection diffusion equation has the form:

$$\frac{\partial c}{\partial t} - \alpha x' \frac{\partial c}{\partial x'} = D\frac{\partial^2 c}{\partial x'^2}. \qquad \ldots 2$$

We non-dimensionalize time and position using the Ranz transformation:

$$\xi = x'/s(t) \text{ and } \tau = \int_0^t Ddt'/s(t')^2 . \qquad \ldots 3$$

The mixing time for extension $\tau_{ext}$, simple shear $\tau_{ss}$, and pure diffusion $\tau_d$ are

$$\tau_{ext} = \frac{D[\exp(2\dot{\gamma}t)-1]}{2\dot{\gamma}s_0^2},\ \tau_{ss} = \frac{D\left[\dot{\gamma}t+(\dot{\gamma}t)^3/3\right]}{\dot{\gamma}s_0^2}, \text{ and } \tau_d = \frac{Dt}{s_0^2}. \qquad \ldots 4$$

Physically, the mixing time, $\tau$ represents the time required for a distribution of solute undergoing pure diffusion to reach the same state as the distribution would in the flow under consideration after a dimensional time, $t$.

The non-dimensionalization in Eq. (3) reduces the convection-diffusion equation (2) to a transient diffusion equation:

$$\frac{\partial c}{\partial \tau} = \frac{\partial^2 c}{\partial \xi^2}. \qquad \ldots 5$$

The transformation to Eq. (5) indicates that the full dynamics of convection-diffusion in linear flows can be captured by a purely diffusive process in the $\xi\tau$-domain with a non-dimensional diffusivity of one.

We can treat SCDI in these flows in a simple manner: using Eq. (5), we model the stirring phase by tracking the evolution of the initial distribution, $c(\xi, \tau = 0)$ for $\tau_{stir}(\dot{\gamma} t_{stir}, D)$, and the un-stirring phase by tracking the evolution of the stirred distribution, $c(\xi, \tau_{stir})$ for an additional $\tau_{unstir}(\dot{\gamma}_{unstir}\ t_{unstir}, D)$. Using the conditions for complete un-stirring, $t_{stir} = t_{unstir}$, and $\dot{\gamma}_{\boldsymbol{unstir}} = -\dot{\gamma}$, we find that $\alpha(t_{unstir}, \dot{\gamma}_{unstir}) = \alpha(t_{stir}, -\dot{\gamma}) = -\alpha(t_{stir}, \dot{\gamma})$. Upon integrating Eq. (3), we find that $\tau_{stir} = \tau_{unstir}$. Hence the final distribution after stirring and un-stirring is simply $c(\xi, 2\tau_{stir})$. Figure 2(b) shows analytical solutions of Eq. (5) during the evolution of the initial square wave distribution. We evaluate $RF(\tau_{stir})$ in the $\xi\tau$-domain as the ratio of the integrated concentration $c(\xi, 2\tau_{stir})$ [shaded area in Fig. 2(b)] within the interval $(-0.5 \le \xi \le 0.5)$ to the integrated initial concentration $c(\xi, \tau = 0)$ within the same interval. Further, $\phi(D_{high}, D_{low})$ can be evaluated from $RF$ with Eq. (1). Given the same initial condition and governing equation, the solutions and measures of reversibility are the same for all linear flows. Thus, using the Ranz transformation [Eq. (3)], we elucidate a unity in the decay of reversibility, $RF$ and of the maximum differential reversibility, $\phi(D_{high}, D_{low})$ in all convection-diffusion processes that are governed by Eq. (5). To appreciate the impact of the Ranz transformation, Fig. 2(c) and 2(d) show the rapid decay of return fraction as a function of total strain $\dot{\gamma} t$ in an extensional flow relative to that in a simple

shear as observed by Aref and Jones [11]. Transforming to the $\tau$-domain in figure 2(e) [using Eq. (4)], the decay of return fraction collapses into a single master return curve and this collapse results in a single master curve for differential reversibility [Fig. 2(f)]. We conclude that the exponential separation and the resulting sensitivity to noise in chaotic flows accelerate the decay of reversibility, but do not, on their own, disrupt the universality observed with the Ranz transformation or change differential reversibility relative to other linear flows.

***Simulation***

We now turn to studying SCDI in nonlinear velocity fields; we use the chaotic sine flow [16] and the non-chaotic steady Taylor-Green vortex flow [17] as examples (Fig. 3). In the chaotic case [Fig. 3(b), first row], the flow switches between two orthogonal

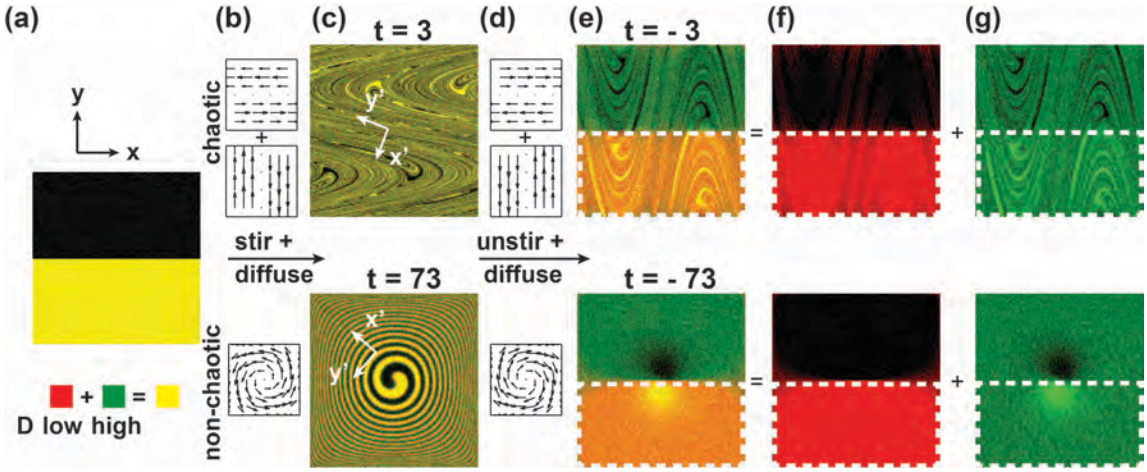


**Fig.3** SCDI in nonlinear Stokes flows. Evolution of concentration profiles of a one-to-one mixture of two tracers of different diffusivities $D_{high} = 5.7 \times 10^{-7}$ (green) and $D_{low} = 5.7 \times 10^{-10}$ (red), (diffusion is non-dimensionalized by $\left[H^2 / T_{cyc}\right]$, where $H$ is the height of the flow domain, $T_{cyc}$ is the time period of the chaotic flow) in the chaotic (first row) and the non-chaotic (second row) flows. **(a)** Initial concentration profile. **(b)** Schematic representation of the velocity fields used for stirring. **(c)** Concentration profile after stirring for $t$ cycles ($t = 3$ for chaotic, $t = 73$ for non-chaotic) equivalent to the same mixing time $\tau$ of 0.24 and 0.00024 for the two diffusivities in both flows. **(d)** Velocity fields used for un-stirring. **(e)** Concentration profiles after un-stirring for the $t$ cycles. The

white dashed line indicates the region where the solutes were present initially in (a). **(f-g)** Individual concentration profiles after unstirring of (f) low diffusivity solute and (g) the high diffusivity solute. These distributions in (f) and (g) add up to give (e).

sine flows with a period, $T_{cyc} \equiv 1$ as given in Eqs. (6) and (7); in the non-chaotic case [Fig. 3(b), second row], the two sine flows operate continuously as given in Eq. (8).

$$u_x = 1.75\sin(2\pi x); u_y = 0; nT_{cyc} \le t < 0.5(2n+1)T_{cyc}; n = 0,1,2... \quad \ldots 6$$

$$u_x = 0; u_y = 1.75\sin(2\pi y); 0.5(2n+1)T_{cyc} \le t < (n+1)T_{cyc}; \quad \ldots 7$$

$$u_x = 0.6125\sin(\pi x)\cos(\pi y); u_y = 0.6125\sin(\pi y)\cos(\pi x); \quad \ldots 8$$

The flows evolve forward [stirring, Fig. 3(b)] for a time, $t$ (number of cycles for chaotic case) and then backward [un-stirring, Fig. 3(d)] for the same time, $t$. We note that this chaotic sine flow does not contain any non-chaotic islands. We simulate the evolution of the concentration profiles of a mixture of solutes of different diffusivities [Fig. 3(a)] with Lagrangian diffusive particle tracking as shown in figure 3. Briefly, the Lagrangian diffusive particle tracking method involves the following [18]: (a) populate the initial flux of solutes [Fig. 3(a)] using $10^6$ particles; (b) track the positions of the particles $\vec{x}$ in the chaotic and non-chaotic flows by solving for the particle trajectories $\frac{d\vec{x}}{dt} = \vec{u} + \vec{B}(t)$, where $\vec{u}$ is the velocity [as shown in Fig. 3(b) and 3(d)], and $\vec{B}(t)$ is the stochastic contribution to the velocity that represents diffusion; (c) obtain the concentration profiles [Fig. 3(a)] by binning particle positions at chosen times.

***Results and Discussion***

In figure 4(a) and 4(b), we plot $RF(\dot{\gamma}t, D)$ calculated with respect to the original volume bounded by the dashed white lines in figure 3(e) for each flow. Noting the similarity in $RF(\dot{\gamma}t, D)$ in figure 4(a, b) (chaotic and non-chaotic flows) and figure 2(c, d) (extension and simple shear), we plot the *RF* as a function of the mixing time, $\tau$. For this purpose, we use $\tau_{<\dot{\gamma}>}$ defined for linear flows in Eq. 4 ( $\tau_{ext}$ for chaotic and $\tau_{ss}$ for non-chaotic flows, with two parameters, the mean strain rate, $\langle\dot{\gamma}\rangle$ that we calculate independently and the initial strand thickness, $s_0$ as an adjustable fitting parameter).

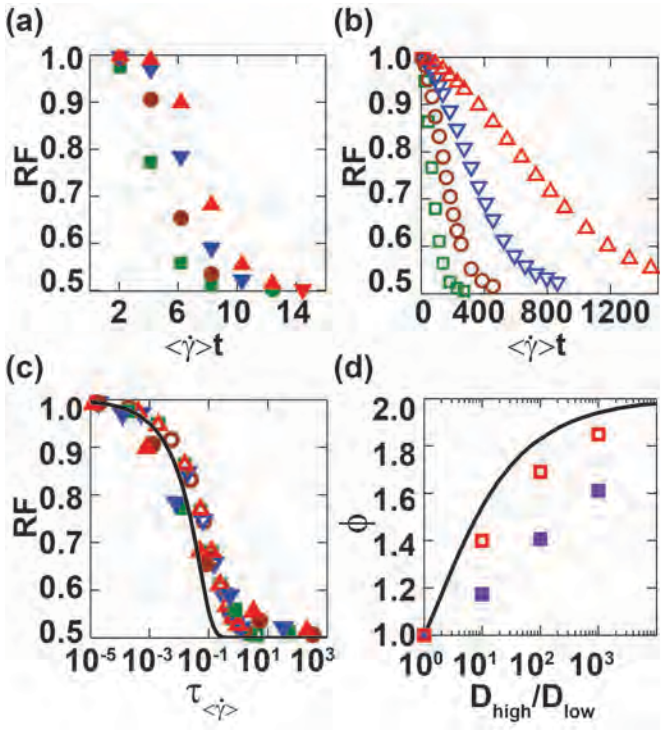


**Fig.4** Characteristics of SCDI in nonlinear Stokes flows. **(a-b)** *RF* as a function of total strain (the mean strain rate $<\dot{\gamma}>$ is 2.07 for the chaotic flow and 2.275 for the non-chaotic flow) for (a) the chaotic flow [D=5.7x10$^{-7}$(■), 5.7x 10$^{-8}$ (●), 5.7x 10$^{-9}$(▼), 5.7x 10$^{-10}$(▲)] and (b) the non-chaotic flow [D=5.7x10$^{-7}$(□), 5.7x 10$^{-8}$ (○), 5.7x 10$^{-9}$(▽), 5.7x 10$^{-10}$(△)]. **(c)** *RF* as a function of mixing time $\tau_{<\dot{\gamma}>}$ [with mean strain rates as in (b) and

adjusted strand widths $s_0$ =0.375 H for the chaotic ( $r^2 > 0.99$ ) and 1.25 H for the non-chaotic flow ( $r^2 > 0.99$ )]. **(d)** Maximum differential reversibility $\phi$ as a function of the ratio of diffusivities for pure diffusive case [black line, same as Fig. 2(e)], chaotic flow (■), and non-chaotic flow (□).

Figure 4(c) shows that $RF\left(\tau_{<\dot{\gamma}>}\right)$ appear to collapse for each class of flow for a range of diffusivities $\left(D = 5.7\times10^{-7} - 5.7\times10^{-10}\right)$, but not onto the master return curve for linear flows [black line replotted from Fig. 2(e)]. We also find that the evolution of $\phi\left(D_{high}, D_{low}\right)$ in chaotic flows and that in non-chaotic flows are distinct from each other and from that in linear flows [Fig. 4(d)]. The universal behavior of *RF* and $\phi$ observed for linear flows does not generalize to nonlinear flows. Interestingly, the maximum differential reversibility is the smallest for the chaotic case. This observation indicates that, while chaos accelerates the absolute rate of decay of reversibility due to diffusion, it reduces the sensitivity to differences in diffusivity for nonlinear flows.

We turn our attention to the origin of the distinct evolution of reversibility in linear and nonlinear flows seen in figure 4(c, d). Strands in nonlinear flows experience a distribution of local strain rates which lead to a distribution of local mixing times $g(\tau)$. We generate the distribution of Lagrangian strain rates as follows: We track the length $r$ of $10^4$ line elements (with initial length $r_0 \equiv 1$) in these nonlinear flows by solving $\frac{d\vec{r}}{dt} = \vec{r}.\vec{\nabla}\vec{u}$ along the trajectory of the center of the line elements. The Lagrangian strain rate is extracted for each line element using its relation to growth of line element in an extensional flow, $\dot{\gamma}(t) = \frac{1}{t}\log\left(\frac{r}{r_0}\right)$ for chaotic flows, and in a

simple shear flow, $\dot{\gamma}(t)=\frac{1}{t}\left[\sqrt{\left(\frac{r}{r_0}\right)^2-1}\right]$ for non-chaotic flows. The distribution of strain rates at any time is extracted from the ensemble of Lagrangian strain rates at that time. Finally, using Eq. (4) ( $\tau_{ext}$ for chaotic and $\tau_{ss}$ for non-chaotic flow), we calculate the distribution of mixing times $g(\tau)$. Figure 5(a) presents $g(\tau)$ for the chaotic and non-chaotic cases. We note that the width of $g(\tau)$ grows exponentially with decreasing diffusivity in the chaotic flow whereas $g(\tau)$ reaches an asymptotic form in the non-chaotic flow.

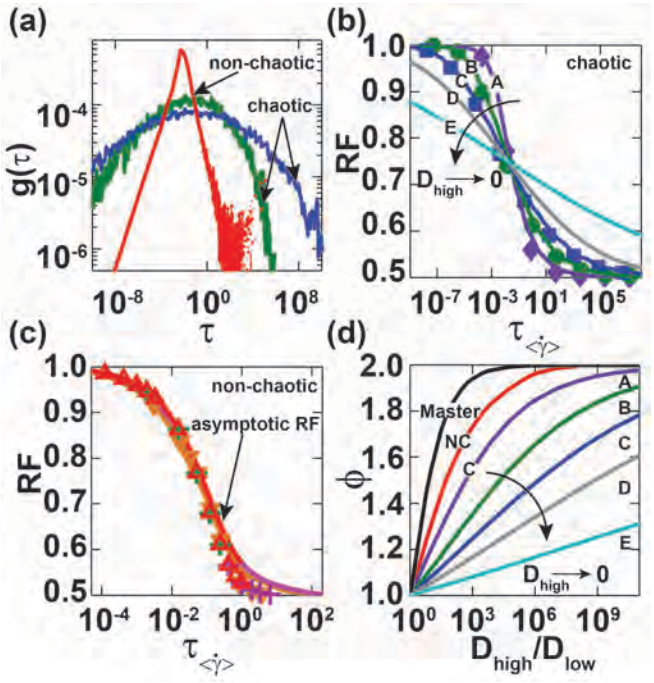


**Fig.5** SCDI in the limit of infinitesimal diffusion using the modified Ranz model. **(a)** Mixing time distribution $g(\tau)$ in the chaotic flow for two diffusive solutes (D = 5.7 x $10^{-16}$ (●), D = 5.7 x $10^{-31}$ (●)) and in the non-chaotic flow for a diffusive solute (D = 5.7 x $10^{-16}$ (●)), for $\tau_{<\dot{\gamma}>}=0.024$. **(b-c)** Return fraction *RF* obtained from numerical simulation as a function of mixing time $\tau_{<\dot{\gamma}>}$ for (b) the chaotic flow (diffusivities 5.7 x $10^{-7}$ (◆), 5.7 x $10^{-16}$ (●) and 5.7 x $10^{-31}$ (■)) and (c) the non-chaotic flow (5.7 x $10^{-4}$(▽), 5.7 x $10^{-7}$(✚), 5.7 x $10^{-10}$(△)). Comparison with the return fraction based on modified Ranz model $RF_{MR}\left(\tau_{<\dot{\gamma}>}\right)$ is shown using solid lines of the corresponding color for each diffusivity and

flow [$s_0$ values in Fig. 3(c)]. In addition, in (b), return fraction $RF_{MR}\left(\tau_{<\dot{\gamma}>}\right)$ corresponding to diffusivities D = 5.7 x $10^{-65}$ (–;D) and D=5.7 x $10^{-257}$ (–;E) are plotted indicating the trend in *RF* as $D \to 0$. **(d)** Maximum differential reversibility $\phi$ as a function of ratio of the diffusivities. The master $\phi$ curve for pure diffusion (–) , the asymptotic $\phi$ curve for non-chaotic flow as predicted by the modified Ranz model (–), and trends for the chaotic case for $D_{high}$ of 5.7 x$10^{-7}$ (–;A), 5.7 x$10^{-16}$(–;B), 5.7 x$10^{-31}$ (–;C), 5.7 x$10^{-65}$ (–;D) and 5.7 x$10^{-257}$ (–;E)) as predicted by the modified Ranz model.

To account for the impact of the distribution of strain rates on the decay of reversibility, we propose a modified Ranz model wherein we compute the weighted average return fraction $RF_{MR}\left(\tau_{<\dot{\gamma}>}\right)=\int_0^\infty RF(\tau)g(\tau)d\tau$. Figures 5(b) and 5(c) indicate that the modified Ranz model captures the observed decay of $RF\left(\tau_{<\dot{\gamma}>}\right)$ for both flows over an extensive range of diffusivities. Thus, the modified Ranz model provides a unified treatment of both chaotic and non-chaotic flows. We note that return fraction in a chaotic flow with islands would decay faster initially due to exponential stretching of the chaotic regions as predicted above, followed by slower diffusive decay due to the islands [19].

To understand if there is a fundamental distinction between chaotic and non-chaotic flows in the context of SCDI, we explore the evolution of return fraction in chaotic and non-chaotic flows using the modified Ranz model in the limit $D \to 0$. Exploration of this limit is motivated by the observation that, while $RF_{MR}$ in non-chaotic flows has already reached an asymptotic curve (distinct from the master return curve of linear flows) for $D = 5.7\times10^{-10}$ [Fig. 5(c)], the dependence of $RF_{MR}$ on $\tau_{<\dot{\gamma}>}$ in chaotic flows becomes increasingly weak [Fig. 5(b)]. Based on our modified Ranz model, we can identify the origin of this distinction of the nonlinear chaotic flow in the persistent growth of the tails of $g(\tau)$; this growth arises from the strong exponential

dependence of the local mixing time $\tau_{ext}$ on the strain of the fluid element. As a result of these tails, $RF_{MR}$ of the global flow is the combined effect of many fluid elements that are fully mixed, many that are unmixed for any finite $D$, and a small fraction (vanishingly small in the limit $D \to 0$) with an intermediate state of mixing that is sensitive to the precise value of $D$. When this weak dependence $RF_{MR}$ on $\tau_{<\dot{\gamma}>}$ for chaotic flows is expressed in terms of differential reversibility [Fig. 5(d), Appendix A.1], the trend indicates that the efficiency of reversal becomes completely insensitive to differences in diffusivity (i.e., $\phi \to 1$ as $D \to 0$). In comparison, the asymptotic form of the RF curve for non-chaotic flows results in an asymptotic form of differential reversibility [red line in Fig. 5(d); different from the master differential reversibility curve (black line)] at finite values of diffusivity. Thus, in the limit of infinitesimal diffusion, the underlying chaotic dynamics leads to complete insensitivity to different levels of diffusion, in distinct contrast to the non-chaotic case.

***Conclusion***

We have shown that, beneath the dramatically different rates of decay of reversibility observed in chaotic and non-chaotic flows, there exists significant unity in the evolution: i) all linear flows lead to a universal decay of reversibility (*RF*) when viewed in an appropriately scaled time domain, and ii) a simple analysis that accounts for the distribution of strain rates successfully captures the decay in both chaotic and non-chaotic, nonlinear flows. Interestingly though, in the limit of infinitesimal diffusion, our analysis predicts a qualitative distinction between chaotic and non-chaotic, nonlinear flows with respect to differential reversibility. We emphasize that the distinction in this asymptotic behavior arises due to the interplay of dynamics, the distribution of rates, and diffusion, and not due to chaos acting as an intrinsic source of irreversibility. Finally,

we note that our study indicates that a baker's transformation (with a single rate of strain) would be the optimal flow with which to implement Heller's separation strategy with respect to both rate and efficiency.

## Appendix

### A.1 Limit of infinitesimal diffusivity for chaotic flows

Modified Ranz model prediction for return fraction for a periodic strand, with a Gaussian distribution of strain rates [following Eq.(22-23)] is given by

$$\begin{aligned} RF &= 0.5 + \frac{4}{\pi^2}\sum_n \int_{-\infty}^{\infty} \frac{1}{n^2}\exp\left(-2n^2\pi^2\tau\right)\exp\left(-\frac{\left(\gamma-\gamma_m\right)^2 t}{2\gamma_m}\right)\frac{d\gamma\sqrt{t}}{\sqrt{2\pi\gamma_m}} \\ &= 0.5 + \frac{4}{\pi^2}\sum_n \int_{-\infty}^{\infty} \frac{1}{n^2}\exp\left(-2n^2\pi^2\frac{\tau}{\tau_m}\tau_m - \frac{\left(\gamma-\gamma_m\right)^2 t}{2\gamma_m}\right)\frac{d\gamma\sqrt{t}}{\sqrt{2\pi\gamma_m}} \end{aligned} \qquad \text{A2.1}$$

Set $\gamma = \gamma_m + k\sqrt{\frac{\gamma_m}{t}}, d\gamma = dk\sqrt{\frac{\gamma_m}{t}}$, and we get

$$\begin{aligned} RF &= 0.5 + \frac{4}{\pi^2}\sum_n \int_{-\infty}^{\infty} \frac{\sin^2\left(n\pi/2\right)}{n^2}\exp\left(-2n^2\pi^2\tau_m\frac{\exp\left(2k\sqrt{\gamma_m t}\right)}{1+k/\sqrt{\gamma_m t}} - \frac{k^2}{2}\right)\frac{dk}{\sqrt{2\pi}} \\ &\approx 0.5 + \frac{4}{\pi^2}\sum_n \int_{-\infty}^{\infty} \frac{\sin^2\left(n\pi/2\right)}{n^2}\exp\left(-2n^2\pi^2\tau_m\exp\left(2k\sqrt{\gamma_m t}\right) - \frac{k^2}{2}\right)\frac{dk}{\sqrt{2\pi}} \end{aligned} \qquad \text{A2.2}$$

This uses the assumption that $\gamma_m t \gg 1$. In the next stage of calculation, we split the integral into 3 different intervals.

$$RF = 0.5 + \frac{4}{\pi^2}\sum_n \int_{-\infty}^{-n_1/\sqrt{\gamma_m t}} \frac{\sin^2(n\pi/2)}{n^2}\exp\left(-2n^2\pi^2\tau_m \exp\left(2k\sqrt{\gamma_m t}\right) - \frac{k^2}{2}\right)\frac{dk}{\sqrt{2\pi}}$$
$$+\frac{4}{\pi^2}\sum_n \int_{-n_1/\sqrt{\gamma_m t}}^{n_2/\sqrt{\gamma_m t}} \frac{\sin^2(n\pi/2)}{n^2}\exp\left(-2n^2\pi^2\tau_m \exp\left(2k\sqrt{\gamma_m t}\right) - \frac{k^2}{2}\right)\frac{dk}{\sqrt{2\pi}} \qquad \text{A2.3}$$
$$+\frac{4}{\pi^2}\sum_n \int_{n_2/\sqrt{\gamma_m t}}^{\infty} \frac{\sin^2(n\pi/2)}{n^2}\exp\left(-2n^2\pi^2\tau_m \exp\left(2k\sqrt{\gamma_m t}\right) - \frac{k^2}{2}\right)\frac{dk}{\sqrt{2\pi}}$$

In the first interval, the dominant term is the Gaussian integral. In the second interval, both terms within the exponential dominate, and in the 3rd interval, the Gaussian term drops out. The choice of interval depends on $\gamma_m t$

$$RF = 0.5 + \frac{4}{\pi^2}\sum_n \int_{-\infty}^{-n_1/\sqrt{\gamma_m t}} \frac{\sin^2(n\pi/2)}{n^2}\exp\left(-\frac{k^2}{2}\right)\frac{dk}{\sqrt{2\pi}} +$$
$$\frac{4}{\pi^2}\sum_n \int_{-n_2/\sqrt{\gamma_m t}}^{n_1/\sqrt{\gamma_m t}} \frac{\sin^2(n\pi/2)}{n^2}\exp\left(-2n^2\pi^2\tau_m \exp\left(2k\sqrt{\gamma_m t}\right) - \frac{k^2}{2}\right)\frac{dk}{\sqrt{2\pi}} \qquad \text{A2.4}$$
$$+\frac{4}{\pi^2}\sum_n \int_{n_2/\sqrt{\gamma_m t}}^{\infty} \frac{\sin^2(n\pi/2)}{n^2}\exp\left(-2n^2\pi^2\tau_m \exp\left(2k\sqrt{\gamma_m t}\right)\right)\frac{dk}{\sqrt{2\pi}}$$

Upon solving the first and the 3rd integral individually, RF can be simplified to give

$$RF = 0.5 + \frac{2}{\pi^2}\sum_n \left(\frac{\sin^2(n\pi/2)}{n^2}\left(1 - erf\left(n_1/\sqrt{2\gamma_m t}\right)\right)\right)$$
$$+\frac{4}{\pi^2}\sum_n \int_{-n_1/\sqrt{\gamma_m t}}^{n_2/\sqrt{\gamma_m t}} \frac{\sin^2(n\pi/2)}{n^2}\exp\left(-2n^2\pi^2\tau_m \exp\left(2k\sqrt{\gamma_m t}\right) - \frac{k^2}{2}\right)\frac{dk}{\sqrt{2\pi}} \qquad \text{A2.5}$$
$$+\frac{4}{\pi^2}\sum_n \frac{\sin^2(n\pi/2)\,Ei\left(2n^2\pi^2\tau_m \exp(n_2)\right)}{\sqrt{2\pi\gamma_m t}}$$

In the limit of $\gamma_m t \to \infty, \frac{n_1}{\sqrt{\gamma_m t}}, \frac{n_2}{\sqrt{\gamma_m t}} \to 0$. Exponential integral term goes to 0. Limits of the second integral go to zero. Only the first term remains.

$$RF = 0.5 + \frac{2}{\pi^2} \sum_n \frac{\sin^2(n\pi/2)}{n^2} \qquad \text{A2.6}$$
$$= 0.75$$

**References**


[1] B. Misra, I. Prigogine, and M. Courbage, Proc. Nat. Acad. Sci. USA **76**, 3607 (1979).

[2] J. L. Lebowitz, Phys. Today **46**, 32 (1993).

[3] G. Drazer, J. Koplik, B. Khusid, and A. Acrivos, J. Fluid Mech. **460**, 307 (2002).

[4] D. J. Pine, J. P. Gollub, J. F. Brady, and A. M. Leshansky, Nature **438**, 997 (2005).

[5] P. Gaspard, *Chaos, scattering and statistical mechanics* (Cambridge Univ. Press, New York, 1998), p.250-253.

[6] D. Levesque, and L. Verlet, J. Stat. Phys. **72**, 519 (1993).

[7] L. Corte, P. M. Chaikin, J. P. Gollub, and D. J. Pine, Nat. Phys. **4**, 420 (2008).

[8] W. E. Ranz, Aiche J. **25**, 41 (1979).

[9] J. P. Heller, Am. J. Phys. **28**, 348 (1960).

[10] G. I. Taylor, *Illustrated Experiments in Fluid Mechanics* (MIT Press, Cambridge, 1972), p.47-54.

[11] H. Aref, and S. W. Jones, Phys. Fluids A: Fluid Dynamics **1**, 470 (1989).

[12] J. M. Ottino, *The kinematics of mixing : stretching, chaos, and transport* (Cambridge Univ. Press, Cambridge, 1997), p.213-214.

[13] P. Dutta, and R. Chevray, Experimental Thermal and Fluid Science **11**, 1 (1995).

[14] G. L. Leal, *Laminar Flow and Convective Transport Processes: Scaling principles and asymptotic analysis* (Butterworth-Heinemann Stoneham, 1992), p.77,171-172.

[15] T. Tél, M. Gruiz, and K. Kulacsy, *Chaotic dynamics: an introduction based on classical mechanics* (Cambridge University Press, Cambridge, 2006), p.262-263.

[16] M. M. Alvarez, F. J. Muzzio, S. Cerbelli, A. Adrover, and M. Giona, Phys. Rev. Lett. **81**, 3395 (1998).

[17] G. I. Taylor, and A. E. Green, Proc. R. Soc. Lond. A-Math. Phys. Sci. **158**, 0499 (1937).

[18] J. D. Kirtland, G. J. McGraw, and A. D. Stroock, Phys. Fluids **18**, 13 (2006).

[19] P. B. Rhines, and W. R. Young, J. Fluid Mech. **133**, 133 (1983).

# CHAPTER 2

# SEPARATION BY CONVECTIVE DIFFUSIVE IRREVERSIBILITY IN THREE DIMENSIONAL FLOWS

## *Introduction*

Laminar transport processes are deterministic in nature, and hence, they are reliable but less efficient means of transferring mass, momentum and energy relative to turbulent `systems. Laminar flows are also inevitable and ubiquitous at small scales or when the viscosity of the fluid is high. So, an important engineering challenge is make laminar flows more efficient for transport processes while benefiting from their simplicity and reliability. Arnold (1) introduced, and subsequently, Aref (2) and Ottino (3) explored chaotic dynamics in laminar flows. Chaotic flows are a special class of deterministic laminar flows whose defining characteristic is that separation between neighboring fluid elements increases exponentially with time within the flow domain. This characteristic has important consequences on the transfer of heat and mass within such a flow because the characteristic distance over which diffusion must act to eliminate differences in concentration or temperature decreases exponentially with time and the interfacial area separating zones of distinct composition grows exponentially in time. This characteristic of chaotic flows has been extensively explored to design systems that use chaotic flows for enhancing mass and energy transfer. There is another potential application of such a system, studied by Aref and Jones (4), and further explored by us (5).

The time-reversibility of Stokes flows was famously demonstrated by Taylor (6). He observed the forward and reversing rotational motion of a dyed volume within a viscous solution in the annular region of a cylindrical Couette cell. He found that the distribution of the solute returned

approximately to its original form and position except for small deviations. Based on Taylor's un-stirring experiment, Heller (7) observed that only the motion governed by the flow field is reversed, displacements due to Brownian diffusion does not reverse. Based on this observation, he proposed a technique for separation, which utilizes the differences in the rate of mixing of solutes of different diffusivities. When a mixture of solutes of different diffusivities is stirred in a carrier fluid for long enough, such that the solute of high diffusivity is mixed (homogenized) while the solute of lower diffusivity is still stirred (segregated), then, upon un-stirring, the solute of lower diffusivity returns approximately where it started; while the solute of higher diffusivity having mixed, does not return. Thus, the original volume occupied by the mixture is partially purified of the higher diffusivity solute. We will call this technique, Separation by Convective Diffusive Irreversibility (SCDI).

Aref and Jones (4) extended the work of Heller to consider the effect of chaotic flow on SCDI. They implemented SCDI using time-reversible chaotic and non-chaotic Stokes flows and identified return fraction (*RF*) as a measurable quantity for comparing the two classes of flows. Return fraction (*RF*) is the fraction of solute that returns to the original volume after un-stirring. They observed that return fraction decreased faster and the rate of separation of solutes increased faster in chaotic flows relative to non-chaotic flows. Subsequently, Dutta and Chevray (8) studied the reversal process numerically and experimentally, with the aim of understanding the effects of inertia on the reversal process. Picking these themes of Aref and Jones, we (5) studied SCDI in chaotic and non-chaotic flows using two dimensional sine flows and proposed an analytical model. Adapted from Ranz's (9) analytical treatment of mixing (simultaneous convection and diffusion), we answered our questions: a) Does the character of Stokes flow influence mass transport during reversal? b) What happens in the limit of infinitesimal diffusion?

We found that the evolution of convective diffusive irreversibility in all linear flows can be unified in the scaled spatial and temporal coordinates proposed by Ranz. However, this unity is disrupted by the presence of the distribution of strain rates in both chaotic and non-chaotic flows.

In this paper, we focus on three dimensional chaotic and non-chaotic flows and explore a continuous separation technique using these flows. We utilize the Ranz model to identify the similarities and differences in the behavior of these classes of flows and understand how flow characteristics and inlet conditions can influence separation efficiency observed in these systems. Finally, we provide guidance towards designing technologies with high separation efficiencies and yields.

***Model System for studying SCDI***

To implement SCDI as a technology, we need to establish the following: the Stokes flow regime, flow reversal and ease of extraction of the purified product. Microfluidics offers channel flows with low Reynolds number due to the small channel size. To implement the reversing flow in microfluidic channels, we identified a practical solution - a fore-aft symmetric channel flow, as depicted in figure 1. A fore-aft symmetric flow refers to the symmetry in the flow field within a fore-aft symmetric physical domain; the transverse, secondary flow shares the same plane of mirror symmetry as the physical domain. Analogous to time-reversibility in the Stokes regime, the flow adopts the fore-aft symmetry of the boundary due to the quasi-steady nature of the flow and the linearity of the governing Stokes equations (6). The fore-aft symmetric channel has the advantage of being a steady, unidirectional and continuous flow system that could allow for practical implementation of this separation technique with ease of collection of the partially purified solute.

In figure 1(a), we sketch the concept of SCDI using fore-aft symmetry in a micro-channel. We will use a microchannel in which stirring and un-stirring are achieved by grooves on the floor for implementing SCDI. Grooves oriented transverse to the channel's axis (*z*) result in transverse secondary flow; this secondary flow stirs the fluid as it flows axially. Stroock et al (10) showed that chaotic and non-chaotic flows can be obtained in a microchannel with staggered herringbone grooves [figure 1(b)i] and oblique grooves [figure 1(c)i], respectively. They termed a set of 6 grooves a half cycle, and 12 grooves a full cycle, and changed the length of stirring by changing the number of cycles. The chaotic flow as shown in figure 1(b)ii consists of two counter rotating vortices, one larger than the other, and the transverse positions of the vortices are switched every half cycle. The non-chaotic flow has a single vortex as shown in figure 1(c)ii.

Stroock et al (11-13) showed that lid-driven cavity flows obtained by solving the biharmonic equation for the stream function (equation 1), coupled with axial poiseuille flow in a rectangular channel can reasonably approximate the three dimensional flow in the chaotic and non-chaotic channel flows in the microchannel with grooves. The details of the axial and transverse velocity fields are discussed in (11-12). Using the flow field solution, the Lagrangian simulation of diffusive tracers in the transversely slipping lid-driven cavity flow is superimposed on axial poiseuille flow in the channel.

$$\nabla^4 \psi = 0, \quad \frac{\partial \psi}{\partial y} = u_x, \quad \frac{\partial \psi}{\partial x} = -u_y \qquad \ldots 1$$

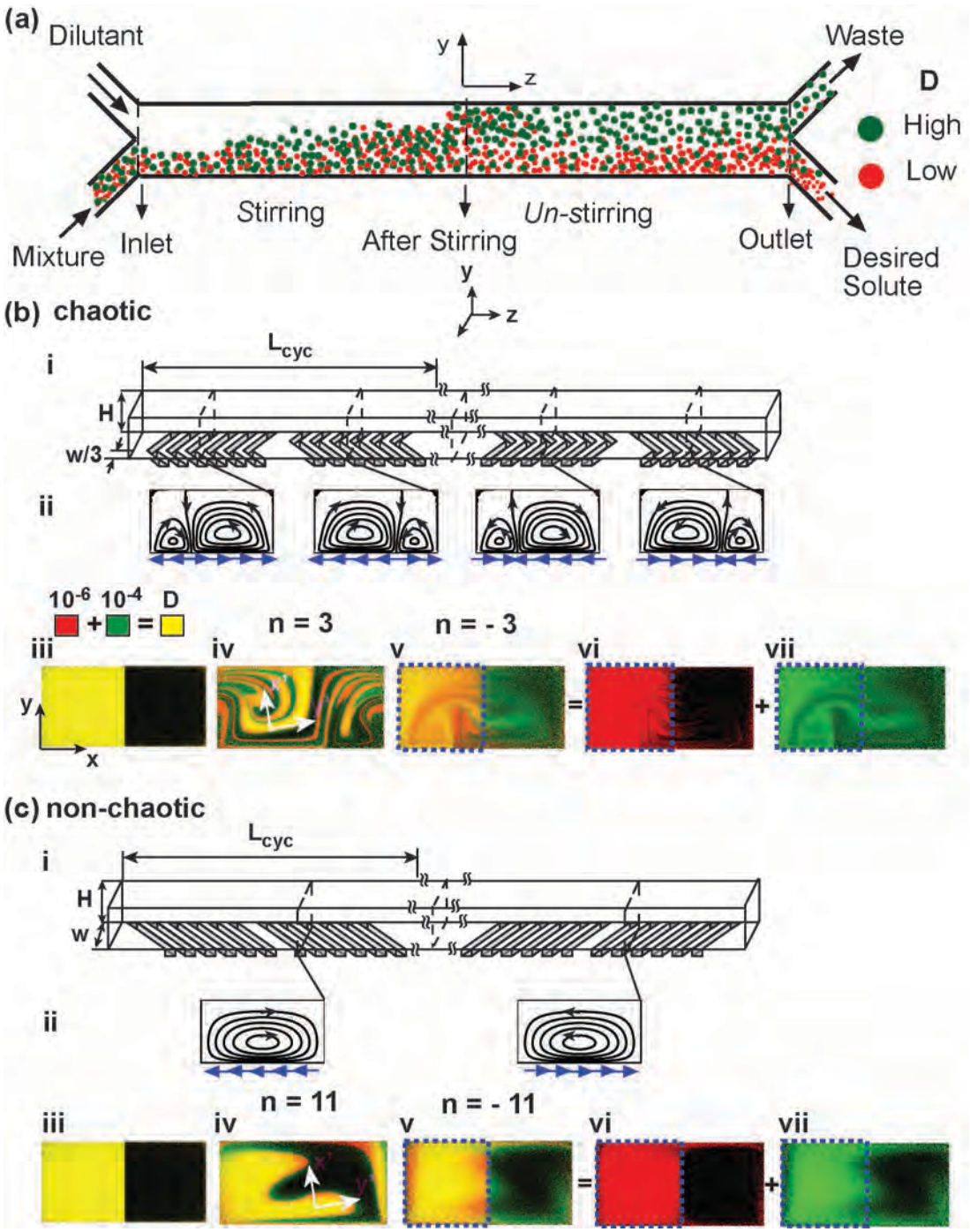


**Fig 1:** Separation by convective diffusive irreversibility (SCDI) using fore-aft symmetric Stokes flows. **(a)** Schematic depicting separation of two solutes (green – high diffusivity, red – low diffusivity) from a mixture by feeding the solution into a channel along with a dilutant, stirring the streams in the stirring section of the channel, un-stirring the streams in the un-stirring section of the channel, and collecting the partially purified solute at one of the outlets. **(b-c)** Numerical simulation of separation using b) chaotic flow and c) non-chaotic flow. The simulation approximates the impact of the grooves with slipping boundaries. The

blue arrows indicate the direction of the slip. **i** Schematic of the fore-aft symmetric micro-channels with grooves on the floor (staggered herringbone – chaotic, oblique – non-chaotic). **ii** The transverse velocity field induced by transverse slip boundary condition. **iii** Inlet concentration profile of a one-to-one mixture (yellow) of solutes of two diffusivities (green $-10^{-4}$, red $-10^{-6}$). **iv** Concentration profile after stirring for *n* cycles ($n=3$ for chaotic, $n=11$ for non-chaotic) . **v** Concentration profiles after un-stirring for the *n* cycles. The blue dashed line indicates the region where the solutes were present at the inlet in iii. The cases shown represent the maximum selectivity, as set by the number of cycles (*n*). **(vi-vii)** Individual concentration profiles after un-stirring of low diffusivity solute(vi) and the high diffusivity solute (vii). These distributions add up to give the distribution in (v).

Following the techniques described in (11) and (12) here, we simulate the Lagrangian diffusive trajectories through the stirring and un-stirring sections of the channel. For the un-stirring section, we capture fore-aft symmetry about the plane $(z=0)$ by setting $u_x(x,y,z)=-u_x(x,y-z)$, $u_y(x,y,z)=-u_y(x,y,-z)$, $u_z(x,y,z)=u_z(x,y,-z)$, where $u_x$, $u_y$ and $u_z$ are the velocity along *x*, *y* and *z* axis. The axial flow in the channel is not reversed during un-stirring. We switch the velocity instantaneously at the end of every half cycle for the chaotic case, and at the end of the stirring half of the channel for the non-chaotic case. This approximation is reasonable since the transition flow (after every switch) occurring within a length $L_{trans} \sim \mathrm{Re}\,H$ lasts for a small length in the Stokes regime.

For a solute with diffusivity *D*, we seeded $10^6$ particles into the flow at the inlet of the channel. The positions of the particles at the inlet were chosen randomly to simulate an axial flux profile corresponding to a uniform inlet concentration in a fully developed Poiseuille flow. The positions of the particles were tracked by integrating the equation 2 using a fifth order Runge Kutta scheme with an adaptive time step. Here, $\vec{u}$ is the velocity field, and $d\vec{B}(t)=\sqrt{2D\Delta t}\hat{\zeta}$ is a

stochastic Wiener process that models random walk due to Brownian diffusion using a standard normal random number generator $\hat{\xi}$.

$$d\vec{\boldsymbol{x}} = \vec{\boldsymbol{u}}dt + d\vec{B}(t) \qquad \ldots 2$$

The evolution of cross-sectional concentration profiles at different axial positions is obtained in the following way: i) dividing the cross sectional area into 64 x 128 squares or finer, ii) at the inlet cross-section, assigning a weight of 1 to particles originating in region with solute and -1 to particles originating in region with only dilutant (without solute), iii) evaluating the flux distribution as the number of particles with weight 1 ($N_+$) and -1 ($N_-$) crossing through each bin of all the cross-sections, and, iv) evaluating the concentration distribution using the equation 3. In equation 3, $u_{bin}$ is the axial velocity at the center of each bin, $a_{bin}$ is the area of the bin, $U_{ave}$ is the average axial velocity of the cross section, $A$ is the cross-sectional area of the channel and $N$ is the total number of particles (total flux).

$$c = \left[ \left( \frac{N_+ - N_-}{u_{bin} a_{bin}} \frac{U_{ave} A}{N} \right) + 1 \right] \Big/ 2 \qquad \ldots 3$$

Data from numerical experiments with individual solutes (identified by their diffusivities) can be combined to evaluate the performance of each flow in the context of SCDI, because the convection and diffusion of solutes do not interfere with each other in the dilute limit. Differential mixing and un-stirring of two solutes is shown in figure 1(b, c) by associating each diffusivity with a different primary color, and combining the colors to yield new shades of secondary colors based on the concentration of two solutes in each bin. Progression of SCDI is computed in the following way. The inlet is fed a solution with two dissolved solutes (red – high diffusivity solute, green – low diffusivity solute) alongside a stream of diluent as seen in figures

1(b)iii and 1(c)iii. The 1:1 mixture of red and green solutes gives yellow color and the black region represents absence of solutes. As the streams progress in the first half of the channel, the solution is stirred into the diluent. The difference in the evolution of the high diffusivity and low diffusivity solutes is visible in figure 1(b)iv and 1(c)iv, at the plane of symmetry of the channel ($z = 0$). The number of cycles of stirring and un-stirring is different for the two flows and is chosen to show the maximum potential to separate the two solutes. As the streams progress through the second half of the channel, the transverse secondary flow is reversed; the streams are unstirred. As seen in figure 1(b)v and 1(c)v, the low diffusivity solute substantially returned to the original area occupied by the stream of solution, while the high diffusivity solute has been dispersed across the entire cross-section. Figure 1(b)vi-vii and 1(c)vi-vii show the distributions of high and low diffusivity solutes independently. At the outlet, the flow is split along the original boundary between the solution and the diluent. The solution stream is partially purified with respect to the high diffusivity solute; we retrieve a solution with a higher ratio of red to green solute than what we started with at the inlet.

To quantify the performance of different flow fields and inlet conditions during SCDI, we define two important parameters, return fraction and maximum selectivity. We denote the cross-sectional area where the solute is present at the inlet as the region of interest (ROI). Return Fraction (*RF*) is defined as the ratio of the flux of solute that returned to the region of interest at the outlet [area inside the blue dashed line Figure 1(b, c) v] to the flux of the solute in the region of interest at the inlet [area inside the blue dashed line in Figure 1(b, c) iii].

$$RF = \frac{\int_{ROI} N^{out} dxdy}{\int_{ROI} N^{in} dxdy} \qquad \ldots 4$$

where ( $N^{in}$, $N^{out}$) are the flux distribution of solute at the inlet and outlet respectively. *RF* represents the yield obtained after the separation process and is a function of the length of stirring section of the channel, and the diffusivity of the solute. The second parameter, maximum selectivity $\phi_{\max}$ is the figure of merit that quantifies the utility of the separation process. We define $\phi_{\max}$ for a pair of solutes, for a given distribution of concentration at the inlet as the maximum of the ratio of return fraction of solutes of two diffusivities with respect to the stirring time:

$$\phi_{\max}\left(D_{high}, D_{low}\right) = Max(\phi) = Max\left(\frac{RF\left(t_{stir}, D_{low}\right)}{RF\left(t_{stir}, D_{high}\right)}\right)_{\forall t_{stir}} \quad \ldots 5$$

$\phi_{max}$ takes a minimum value of 1 in the case when no separation of solutes is achieved, and a maximum value defined by ratio of the channel's cross-sectional area to the area occupied by the mixture of solutes at the inlet. Unlike *RF*, $\phi_{\max}$ is a rate independent quantity, thus providing an unbiased comparison of flows with different mixing characteristics for its utility for implementing SCDI.

Having established the background, the flow system and the figures of merit to study SCDI, we turn to describe the theoretical framework which forms the center-piece of the paper. Following this description, we adapt the model for chaotic and non-chaotic flows, explore the impact of different flow characteristics on SCDI and propose ways to enhance the yield and selectivity achieved using this technique.

***Ranz model***

The general yet simple description of the flow suggested by Ranz (9) points us towards understanding the interplay between convection and diffusion in the context of SCDI. This model describes mixing by studying the Lagrangian dynamics of strands or filaments of diffusive solute in local linear flow of general flows. Batchelor suggested that there exists a tendency of two dimensional flows in the microscales of turbulence (14). Villermaux and others have used the local linear flow model to define local concentration of strands that undergo 'merging' during chaotic mixing (15-16). We (5) have shown the current adaptation of the Ranz model to study SCDI. Here, we elaborate and explore the adaptation of the Ranz model in greater detail.

In the chaotic and non-chaotic flows described in figure 1(b)iv and 1(c)iv, we notice several thin strands of dye whose strand widths are much smaller than the dimensions of the cross-section of the channel. Ranz (9) discusses mixing in various flows. He points out that, for weak diffusion, mixing of a periodic array of bands of solute in linear flows can capture mixing in the more general nonlinear flows. The basis of this argument is that stretching and folding by a general flow typically results in an approximate spatial periodicity (of wavelength $\lambda$) in the concentration field over short distances. Additionally, over short distances, the flow is approximately linear.

Chaotic flows are characterized by the sensitivity to initial conditions or more precisely the exponential separation in time of neighboring trajectories in the flow domain. This behavior is captured in one of the simplest linear flows, pure extension (Figure 2ai). To make this flow bounded, we can periodically halt the extension, cut along the contractile axis (Figure 2aii), and reassemble the fluid into its original geometry (Figure 2aiii). This process mimics the manipulation of dough by a baker and is thus called a baker's transformation. The extensional

baker's transformation provides a useful model flow with which to consider the impact of chaos on transport processes. We can similarly construct a shearing baker's transformation by deforming the fluid with simple shear, cutting it, and reassembling it (Figure 2b). As suggested by Ranz (9), this shear deformation can serve as a simple model of general, non-chaotic flows. Importantly, these models capture the distinct evolution of the characteristic distance, s(t), over which diffusion must act to eliminate differences in concentration or temperature. In pure extension, s(t) decreases exponentially with time; in simple shear, s(t) varies algebraically with time, with decreasing rates.

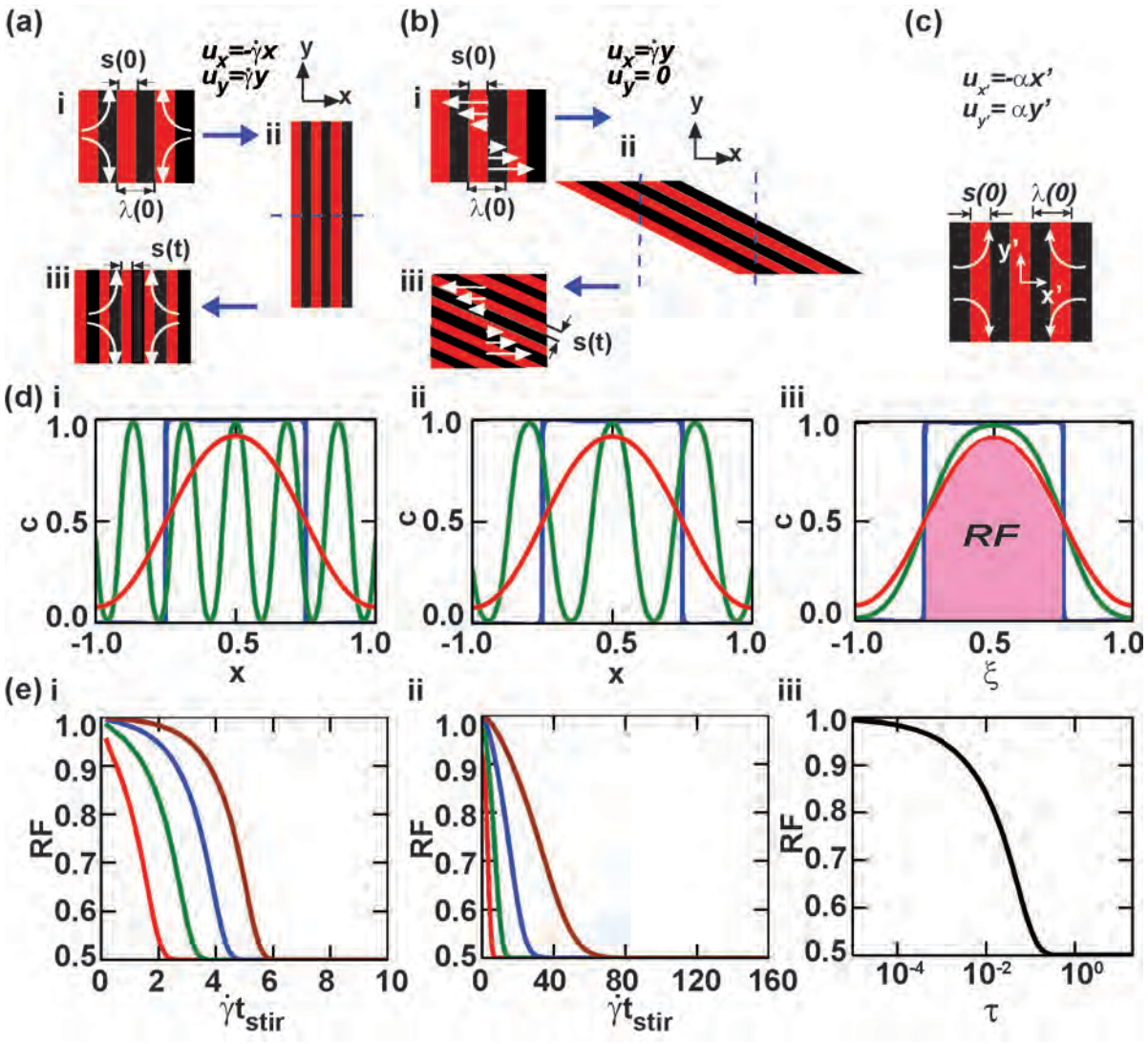


**Fig 2:** Separation by convective diffusive irreversibility (SCDI) (SCDI) in model two-dimensional linear flows **(a,b)** Chaotic and non-chaotic laminar flows realized using Baker's transformation, idealized stirring processes achieved with repeated sequences of (i) deformation in a linear flow, (ii) cutting, and (iii) reassembly. Pure extension captures the characteristic exponential stretching that occurs in chaotic flows (a). Simple shear captures the power law stretching observed in non-chaotic flows (b). **(c)** The same initial concentration distribution of a diffusive solute (red) in (a, b) is represented in the Lagrangian frame of reference of the strand $(x', y')$. **(d)** Concentration profile $c(\xi,\tau)$ predicted by the Ranz model (solution to equation 10) initially ( $\tau = 0$; blue curve), after stirring, ( $\tau_{stir} = 0.02$ ; green curve), and after unstirring ( $\tau_{unstir} = 0.04$ ; red curve) in **i** extensional, **ii** simple shear flow, and **iii** transformed space $\xi$. Return fraction $RF$ is defined as the area of shaded region illustrated in (iii). **(E)** Decay of $RF$ in i extension and ii simple shear as a function of total shear, $\dot{\gamma}t$ for four different diffusivities (red – $10^{-4}$, green – $10^{-5}$, blue –$10^{-6}$, brown –$10^{-7}$). **iii.** $RF$ is plotted as a function of the mixing

time, $\tau$ . It represents the master return curve $RF(\tau_{stir})$ for convection-diffusion in all linear flows, including the limit of pure diffusion (no flow).

Having described the simple two dimensional linear flow models for chaotic and non-chaotic flow, we study SCDI in these flows. In addition, we will consider a third system: pure diffusive system in which there is no flow. In the flow systems, when the deforming strands are observed in the local Lagrangian frame (*x', y'*) that translates with the strand and rotates along with the strand's extensional axis, we observe the strands as shown in figure 2(c). In this frame, the strand experiences an effective rate of extension along $y'$ of $\alpha(t,\dot{\gamma}) = -d\ln[(s(t)/s(0))]/dt$ where $s(t)$ is the width of the strand at time $t$, $s(0) = s_0$ is the width of the strand at the inlet and $\dot{\gamma}$ is the actual strain rate in the flow. Note that in the Lagrangian frame of reference, the strand does not align with the extensional axis for the simple shear flow, but eventually aligns in the flow direction. The effective strain rates in a simple shear flow and extensional flow are shown in equation 6 and 7, respectively. We note that a strand in a simple shear flow experiences an effective strain rate that increases linearly at early times, but at late times, the effective strain rate decreases inversely with time as the strand orients along the flow direction.

$$\alpha_{ss} = \dot{\gamma}^2 t/\left[1+(\dot{\gamma}t)^2\right] \qquad \ldots 6$$

$$\alpha_{ext} = \dot{\gamma} \qquad \ldots 7$$

The evolution of concentration ($c$) is governed by the convection-diffusion equation. In the local reference frame (*x', y'*), the convective-diffusive equation is as shown in equation 8:

$$\frac{\partial c}{\partial t} - \alpha x' \frac{\partial c}{\partial x'} = D\frac{\partial^2 c}{\partial x'^2} \qquad \ldots 8$$

Using the transformation (equation 9) suggested by Ranz to non-dimensionalize time and space, we transform the convective diffusion equation in equation 8 to pure diffusion equation in equation 10.

$$\xi = x'/s(t) \text{ and } \tau = \int_0^t D dt'/s(t')^2 . \qquad \ldots 9$$

$$\frac{\partial c}{\partial \tau} = \frac{\partial^2 c}{\partial \xi^2} \qquad \ldots 10$$

The transformation to equation 10 indicates that the full dynamics of convection-diffusion in linear flows can be completely captured by a purely diffusive process in the $\xi\tau$-domain with a non-dimensional diffusivity of one. The mixing time for extension $\tau_{ext}$, simple shear $\tau_{ss}$, and pure diffusion $\tau_d$ are

$$\tau_{ext} = \frac{D[\exp(2\dot{\gamma}t) - 1]}{2\dot{\gamma}s_0^2},\ \tau_{ss} = \frac{D[\dot{\gamma}t + (\dot{\gamma}t)^3/3]}{\dot{\gamma}s_0^2}, \text{ and } \tau_d = \frac{Dt}{s_0^2}. \qquad \ldots 11$$

Physically, the mixing time, $\tau$ represents the non-dimensional time required for a distribution of solute undergoing pure diffusion to reach the same state as the distribution would in the flow under consideration after a dimensional time, *t* (non-dimensionalized by the diffusive time scale $\frac{s_0^2}{D}$). Mixing time $\tau$ represents the 'direction of time' in a mixing process. It can never decrease with time. For a stirring process without diffusion, $\tau$ = 0 for all times. This understanding of $\tau$ is fundamental to the definition of a diffusively irreversible process.

In linear flows, stirring involves stretching the strand along its extensional axis, and un-stirring involves contraction along the same axis. We can treat SCDI in these flows in a simple manner: Starting with the initial concentration distribution $c(\xi, \tau = 0)$, using Eq. (10), we model the

stirring phase by tracking the evolution of $c(\xi,\tau=0)$ for a mixing time $\tau_{stir}(\dot{\gamma}t_{stir},D)$, and the un-stirring phase by tracking the evolution of the concentration distribution at the end of stirring, $c(\xi,\tau_{stir})$ for an additional $\tau_{unstir}(\dot{\gamma}_{unstir}\ t_{unstir},D)$. Using the conditions for complete un-stirring, $t_{stir}=t_{unstir}$ , and $\dot{\gamma}_{\boldsymbol{unstir}}=-\dot{\gamma}$ , we find using equation (6-7) that $\alpha(t_{unstir},\dot{\gamma}_{unstir})=\alpha(t_{stir},-\dot{\gamma})=-\alpha(t_{stir},\dot{\gamma})$ . Upon integrating equation for $\tau_{stir}$ and $\tau_{unstir}$ in equation 9, we find that $\tau_{stir}=\tau_{unstir}$ . Hence the final distribution after stirring and un-stirring is simply $c(\xi,2\tau_{stir})$.

This use of the Ranz model shows that the convective diffusive interplay in a reversal process is equivalent to mixing in the forward direction for $2\tau_{stir}$ indicating that the mixing occurs even during the un-stirring. However, we note that mixing for $2\tau_{stir}$ in the mixing time domain is not the same as forward mixing for $2t_{stir}$ in the real time domain expect for a pure diffusive system. In fact, going from $\tau_{stir}$ to $2\tau_{stir}$ in the mixing time domain or un-stirring for $t_{stir}$ after stirring for $t_{stir}$, is equivalent to forward mixing for small additional time ($\left(\log 2/2\dot{\gamma}\right)$ for extensional flow, $\left(\sqrt[3]{2}-1\right)t_{stir}$ for simple shear flow $\forall\ \dot{\gamma}t_{stir}>>1$) beyond $t_{stir}$.

In figure 2(d) we show analytical solutions of equation 10 during the evolution of concentration from the initial square wave profile to the concentration profile after stirring and then the concentration profile after the un-stirring in an extensional flow [Fig 2(d)i], a simple shear flow [Fig 2(d)ii] and in the Ranz transformed space [Fig 2(d)iii] for the same mixing time $\tau_{stir}=0.02$ . This value of $\tau_{stir}$ corresponds to $\dot{\gamma}t_{stir}=1.89$ for the extensional case and $\dot{\gamma}t_{stir}=3.58$ for the simple shear case. After the stirring phase (green lines), we observe that the thickness of the strand (and the thickness of non-solute region between the strands) is smaller for extensional

flow relative to a simple shear flow. This difference captures, qualitatively, that seen in the chaotic [Fig.1(b)iv] and non-chaotic [Fig.1(c)iv] channel flows. After the un-stirring phase (red lines), concentration profiles are exactly the same for all three cases; this similarity again captures, qualitatively, that predicted for more general chaotic and non-chaotic flows [Fig.1(b-c)vi,vii].

To make quantitative assessments of the evolution during stirring and unstirring, we evaluate return fraction and the maximum selectivity. $RF(\tau_{stir})$ in the $\xi\tau$-domain is the ratio of the integrated concentration $c(\xi, 2\tau_{stir})$ [shaded area in Fig. 2(d)iii] within the interval $(-0.5 \le \xi \le 0.5)$ to the integrated initial concentration $c(\xi, \tau = 0)$ within the same interval. For the initial distribution in Fig. 2(d) [blue lines in Figs. 2(d)i-iii], we can perform these integrals analytically to find:

$$RF = \sum_n \frac{1}{(n\pi)^2} \sin^2\left(n\pi \frac{s_0}{\lambda_0}\right) \exp\left[-\left(\frac{2n\pi s_0}{\lambda_0}\right)^2 2\tau_{stir}\right] + \frac{s_0}{\lambda_0} \qquad \ldots 12$$

In equation 12, we find that *RF* has exponential dependence on mixing time, and decays exponentially to $s_0/\lambda_0$ at large $\tau_{stir}$. We emphasize that equation 12 holds for all linear flows (including pure extension and simple shear) and the purely diffusive case, given the same initial condition. To appreciate the impact of the Ranz transformation, we show the rapid decay of return fraction as a function of total strain $\dot{\gamma}t$ in an extensional flow [Fig. 2(e)i] relative to that in a simple shear [Fig. 2(e)ii] much like that observed in the simulation of a chaotic flow by Aref and Jones (4). Transforming to the $\tau$-domain in Fig. 2(e)iii [using equation 9], the decay of return fraction collapses into a single master return curve. Thus, using the Ranz transformation, we elucidate the underlying unity in all the measures of concentration evolution in all

convection-diffusion processes that are governed by equation 8. Similar to the master return curve, maximum selectivity $\phi_{\max}$ which in turn is based on the ratio of return fraction (equation 5), exhibits universal behavior as a function of the ratio of diffusivities for a given initial condition for all linear flows and solutes.

Following our discussion on convective diffusive irreversibility in linear flows, we will now discuss convective diffusive irreversibility in general chaotic and non-chaotic channel flows that we introduced in section II. As discussed earlier, extensional flow and simple shear flows represent the average local linear behavior of the chaotic and non-chaotic flow, respectively. Repeating our adaptation of the Ranz model for two dimensional sine flows in (5) to the three dimensional channel flow system, we provide a complete explanation towards an optimal implementation of the system for SCDI.

***Comparison: Simulation versus Ranz model***

We performed the numerical calculations in the realistic, non-linear chaotic and non-chaotic flows with fore-aft symmetry for solutes of D = $10^{-4}$, $10^{-5}$, $10^{-6}$, and $10^{-7}$. The evolution of the concentration profiles of solute with D = $10^{-7}$, when stirred and un-stirred in these flows is shown in Figure 3. We track and compare the evolution of concentration profiles in the two flows using a non-dimensional time. The non-dimensional time is defined as the average residence time $t_r = \frac{z}{U}$ multiplied by the average transverse shear rate $\langle \bar{\dot{\gamma}} \rangle$ in the respective flow (discussed later in this section). The non-dimensional time represents the transverse shear experienced by the solute when stirred for a time $t_r$. As the concentration profiles evolve with increasing $\langle \bar{\dot{\gamma}} \rangle t_r$, the irreversibly mixed regions in the unstirred concentration profiles (grey colored regions) increase in size. And these irreversibly mixed regions expand faster in the chaotic [Figure 3(a)] than the

non-chaotic flows [Figure 3(b)]. In the case of chaotic flows, the patterns generated by the gray contours in the unstirred concentration profiles are the un-stable manifolds of stirring flow which cover the entire cross-section at higher $\langle \bar{\dot{\gamma}} \rangle t_r$. In the non-chaotic flows, the regions with higher strain rate turn gray first whereas regions with nearly zero strain rates take order of diffusive time to turn gray. The supplementary information contains movies of the numerical simulation of the stirring and un-stirring in the two flows.

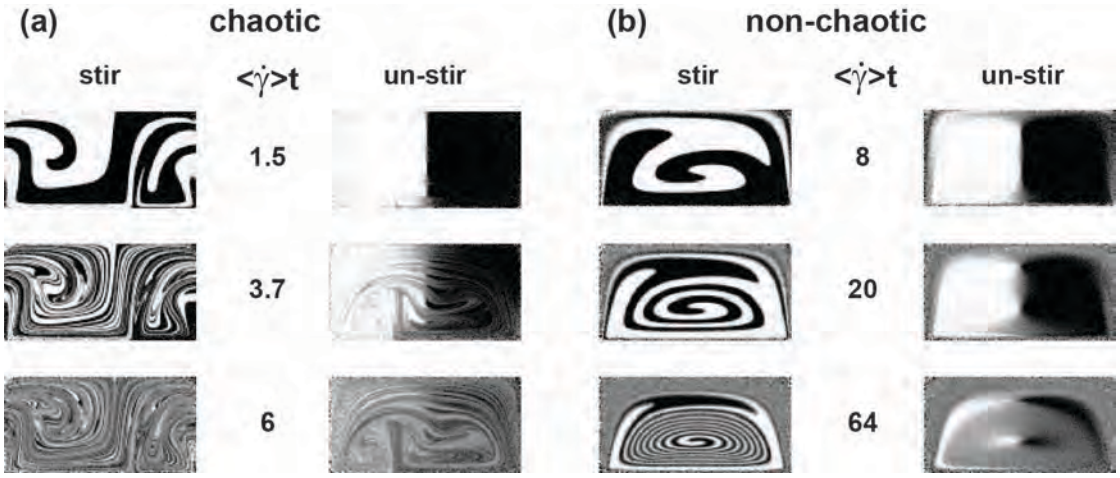


**Fig 3:** Concentration profiles after stirring and un-stirring in the 3-D, duct flows. **(a-b)** chaotic flow (a) and non-chaotic (b) flows at different average residence times $\langle \dot{\gamma} \rangle t$ selected to capture the early, intermediate and late stages of convective-diffusive irreversibility in the two flows for a solute with $D = 10^{-7}$.

Using equations 4 and 5, we then evaluated the figure of merits, return fraction and maximum selectivity in these flows. The value of return fraction at high $\langle \bar{\dot{\gamma}} \rangle t_r$ (when the solute is well homogenized across the channel cross-section) is the ratio of flux in the cross-section where the solute is originally found to the entire cross-section (Appendix A.1). Due to exponential amplification of the round off errors in the chaotic flows, even non-diffusive tracer trajectories will experience differences in the transverse position of the trajectory at the inlet and the exit of

the reversing flow channel. This numerical error increases with increase in $\langle \bar{\dot{\gamma}} \rangle t_r$. Since large numerical errors can lead to inaccurate mixing behavior, we estimate the relevance of the numerical error by calculating the decrease in return fraction for non-diffusive solutes ($D = 0$) as a function of number of cycles of stirring and un-stirring. In the absence of numerical error, *RF* should remain at 1 for all times. Due to numerical error, we found that after 15 cycles of stirring and un-stirring for non-diffusive solutes ($D = 0$), *RF* dropped by 6%, from 1 to 0.94. Since the solutes ($D = 10^{-4} - 10^{-7}$) are well mixed before 15 cycles, the numerical error is expected to have negligible impact on the *RF* for all the cases studied here.

In order to adapt the Ranz model for the three dimensional non-linear chaotic and the non-chaotic flows with fore-aft symmetry, we transformed the length of stirring and un-stirring into the mixing domain using the average residence time, average transverse strain rate in the flow, diffusivity of the solute and initial strand width. We note that the definitions of mixing time in equation 11 assume specific initial orientation of the strand for the sake of simplicity: for the extensional flow, the strand length is assumed to be oriented along the extensional axis; for the simple shear flow, the strand width is assumed to be aligned with the streamline direction. The validity of these assumptions for a variety of inlet conditions is discussed in later sections. The Eulerian estimate (order of magnitude) of the non-dimensional strain rate $\left( \dot{\gamma}_e = \frac{u_{slip}}{2h} \right)$ based on the transverse slip velocity of the floor is 0.05 and for the initial conditions used in Figure 1(b)iii and 1(c)iii, $s_0$ is $O(h)$. However, since the Ranz model is based on the Lagrangian frame of reference, we evaluate the Lagrangian mean strain rate in the two flows and use $s_0$ the initial strand width, as an adjustable parameter in the model. We found the Lagrangian average strain rate $\langle \bar{\dot{\gamma}} \rangle$ to be 0.0093 and 0.0145 for the chaotic and non-chaotic flows respectively (using the

Lagrangian line element calculation in the flows; see Section V.1.i). The initial strand width $s_0$ is evaluated using least squares fit of the *RF* data from numerical simulation and the prediction of the Ranz model. We note that the initial strand width is dependent on the concentration distribution in the channel and is the order of a characteristic length scale of the inlet solute distribution (i.e., ~*H*). We define the mixing time obtained using average strain rate $\langle \bar{\dot{\gamma}} \rangle$ at a given residence time and diffusivity as $\tau_m$ (Equation 11, $\tau_{ext}$ for the chaotic flow and $\tau_{ss}$ for the simple shear). In evaluating *RF* using equation 12, we use the ratio $\frac{s_0}{\lambda_0}$ is determined by the ratio of flux through the area occupied by the solute at the inlet to the total flux through the entire cross-section [Appendix, A.1].

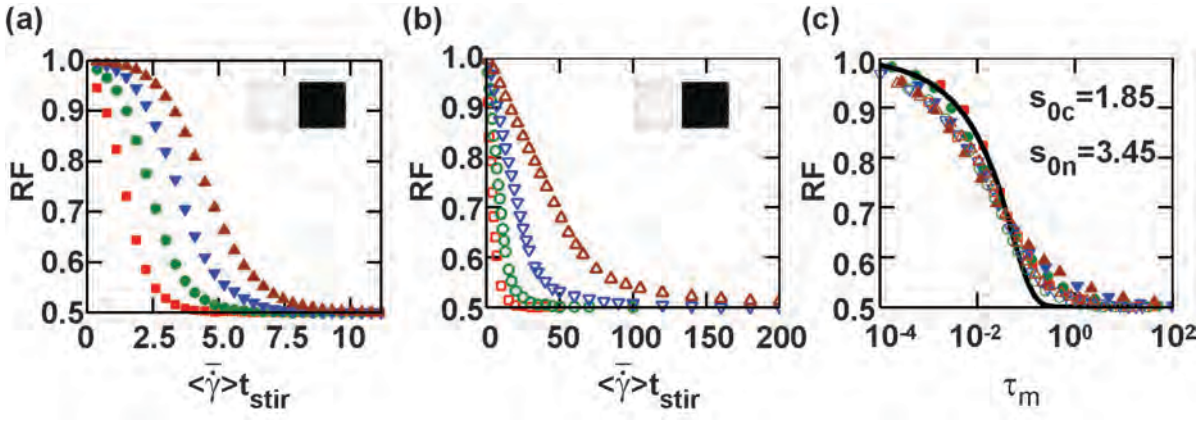


**Fig 4:** Return fraction and the Ranz model in 3-D, non-linear flows: **(a-b)** Comparison of *RF* based on flux (diffusivities represented are $10^{-4}$ –red square, $10^{-5}$ dark green circle, $10^{-6}$ – blue inverted triangle, $10^{-7}$ – brown triangle ) as a function of $\langle \dot{\gamma} \rangle t_{stir}$ in the chaotic flow (a) and the non-chaotic flow (b). All the symbols represent results from the numerical simulation. The open symbols represent chaotic flow, and the closed symbols represent the non-chaotic flow. The inset shows the inlet concentration profile for these return fraction curves. **(c)** Comparison of *RF* obtained from simulation for chaotic (a), non-chaotic flow (b) and the prediction of the Ranz model (black line) in the mixing time domain. The strand width parameter used in the model for the chaotic ($s_0$) and non-chaotic flow ($s_{0n}$) is shown in the inset of (c).

We first consider a simple inlet concentration distribution in which the solute is present in the left (or right) half of the channel inlet cross-section. The decay of return fraction (*RF*) obtained from simulation in the chaotic [Fig. 4(a)] and non-chaotic [Fig. 4(b)] flows is similar to the *RF* behavior observed in extensional [Fig. 2(d)i] and simple shear [Fig. 2(d)ii] flows, respectively. To study the effectiveness of mixing time $\tau_m$ [equation 11, $\tau_{ext}$ for chaotic and $\tau_{ss}$ for non-chaotic flows], we plot *RF* as a function of $\tau_m$ in figure 4(c) using $\langle \bar{\dot{\gamma}} \rangle$ and $s_0$ as an adjustable parameter. In this case, we found the best fit values of $s_0$ to be 1.85 and 3.45 for the chaotic and non-chaotic flows, respectively.

In Figure 4(c), we see that transformation into mixing time collapses the *RF* curves across various diffusivities for both the chaotic flow and non-chaotic flow, independently. The most evident variation across diffusivities that persists is seen in the slope around the inflection point for the chaotic flow (closed symbols in Figure 4(c)): the slope decreases with decreasing diffusivity. Relative to the dramatically different curves for the chaotic and non-chaotic cases in Figures 4(a) and 4(b), the transformation also goes a long way toward unifying the evolution for these two distinct flows in Figure 4(c): the sigmoidal form of all curves becomes evident, with an inflection point near $\tau_m \sim 0.1$. The transformation and adjustments of $s_0$ also bring the *RF* curves for these two non-linear flows close, in form and position, to the master curve for linear flows [black line in Figure 4(c)], although significant deviations remain.

Thus, our adaptation of SCDI in model linear flows using the Ranz model indicates that while there is similarity between the chaotic and non-chaotic flows when viewed in the mixing time domain, they exhibit differences that are not captured by the Ranz model. We will probe several

flow characteristics of the chaotic and non-chaotic flows in order to understand and predict the reversibility characteristics in these flows.

***Factors influencing convective diffusive irreversibility***

We notice that there exists a distribution of strand thicknesses in the chaotic and non-chaotic flows [Fig. 3(a, b)]. This distribution of strand widths could be due to the presence of different rates of strain in different regions in the flow which stretch the strands to different widths in some regions, and folds the strands to different thickness in other regions. Another character of the flow field where chaotic and non-chaotic flows differ is the periodicity of the trajectories. Chaotic flows are aperiodic, whereas our current non-chaotic flow is periodic in the transverse flow direction. To establish the generalized Ranz model, we will study the effect of these flow properties on the reversal characteristics of the chaotic and non-chaotic flows. We will incorporate the physical understanding obtained from results of the numerical simulation into our model.

**Distribution of strain rates**

As discussed above, distribution of strand widths in a general flow is likely due to the presence of different rates of strain in different regions in the flow which stretch the strands to different widths in some regions, and folds the strands to different thickness in other regions. Distribution of strain rates in a flow field results in a distribution of mixing times. The distribution of mixing times when operating on a given inlet concentration field results in a distribution of concentration gradient patterns; some with thick strands and thin strands with sharp concentration gradients, and some with diffusive remnants of strands. In this paper, we will explore the effect of distribution of strain rates to understand its effect on convective diffusive irreversibility of general flows.

Numerical calculation of strain rate distribution

In order to understand the local flow, we examined the streamlines of the transverse velocity field found in the chaotic and non-chaotic flows [Fig. 1(b)ii, Fig.1(c)ii]. In the Eulerian frame of the transverse flow field, we observe a variety of local linear flows within both these flows. For example, the regions near the center of vortices present a simple shear flow, whereas the corners near the slip wall present a strong extensional character. However, given that chaotic flows establish strong extensional local flow characteristics arising from switching the velocity field every half cycle, the gradients of velocity experienced along a Lagrangian trajectory play a greater role in defining the local flow behavior. Numerical simulations of a cloud of non-diffusive fluid particles in the chaotic flow and non-chaotic flow corroborate the local linear assumption of the Ranz model and suggest that the local strain rates along Lagrangian trajectories or the Lagrangian strain rates play a key role in the mixing and the reversal characteristics of the flow.

To evaluate the distribution of Lagrangian strain rates, we can track the growth of distance between pairs of fluid particles that continuously experience the same local linear flow. To track this process, we proceed as follows:

(a) We transform the governing equation for pairs of fluid particles ( $d\vec{x}/dt = \vec{u}$ ) to a governing equation for the distance between the pair of fluid particles or fluid line element $\vec{r}$ that advects with the flow [17-18], as shown in equation (13). $\vec{r}$ is non-dimensionalized by $h$ and $\vec{u}$ by $U$.

$$\frac{d\vec{r}}{dt} = \vec{r}.\vec{\nabla}\vec{u} \qquad \ldots 13$$

The growth of a line element $\vec{r}$ is governed by local velocity gradients and is equivalent (at the first order or at early times) to the instantaneous growth of distance between a pair of particles experiencing the same local flow. The simulation of growth of the line element using Eq. (19) accurately captures the local strain rate at all times.

(b) We populated the inlet cross-section with 1000 non-diffusive particles that represent the center of a line element $\vec{r}$, with unit initial length $r_0 \equiv 1$. The seeding of initial positions is random and simulates the axial flux distribution of a fully developed Poiseuille flow.

(c) We chose the initial orientation of the line element to be random for the chaotic flow because the line elements in a chaotic flow reorient themselves continuously. This continuous reorientation of the line element occurs because the extensional character of different regions of the flow explored by the trajectory attempts to orient the line element along its extensional axis within a short time of $O\left(\frac{1}{\dot{\gamma}(x,y,z)}\right)$, where $\dot{\gamma}(x,y,z)$ is the local strain rate in that region. In the non-chaotic flow, the rate of reorientation of the strand is a function of the current orientation. Attempting to match orientation of the strand with the interface of the solute and non-solute region at the inlet leads to the dependence of the extracted strain rate distribution on the inlet concentration. To simplify the adaptation of the Ranz model for the non-chaotic flow, we chose the line elements to be initially oriented perpendicular to the streamlines.

(d) We tracked the length $r$ of the line elements in the stirring section of our model chaotic and non-chaotic flow by integrating equation 13 along the trajectory of the center of the line elements. This is done by integrating equation 13 at each time step of the Lagrangian non-diffusive particle tracking simulation [based on integrating equation 2 (with $D = 0$), where the

particle is the center of the line element]. Since the stirring and un-stirring are governed by the transverse flows, we track the growth of the line element in the transverse directions ($x$,$y$) only.

(e) We defined a time averaged Lagrangian strain rate $\bar{\dot{\gamma}}(t_r)$ as follows. For every particle tracked, the time averaged Lagrangian strain rate is evaluated as the equivalent strain rate obtained in the model linear flow in order to achieve the same length $r$ in time $t$ as the general flow at hand. The extensional flow and the simple shear flow relation for the chaotic and non-chaotic flows, respectively, are shown in equation 14 and 15.

$$\bar{\dot{\gamma}}(t_r) = \frac{1}{t}\log\left(\frac{r}{r_0}\right) \qquad \ldots 14$$

$$\bar{\dot{\gamma}}(t_r) = \frac{1}{t}\left[\sqrt{\left(\frac{r}{r_0}\right)^2 - 1}\right] \qquad \ldots 15$$

These simplified definitions provide an average strain rate based on the length of the line element at time $t$. We also note that the instantaneous local Lagrangian strain rate at each particle position can be defined based on the local flow and growth of the line element in that time step. With this definition, we can evaluate the mixing time without any assumptions about the nature of the local flow. We evaluate mixing time by transforming the integral definition of $\tau$ given in equation 9 into equation 16 below, making no assumptions of the nature of the local flow.

$$\tau(t_r) = \int_0^t r(t')^2 \, D dt' \qquad \ldots 16$$

where $t_r = z/u_{ave}$, the average residence time and $t$ is the Lagrangian time required by the particle to reach a chosen axial distance z. In equation 16, we use the relation that total area of the fluid line element remains constant ( $r_0 s_0 = rs$, and assuming $s_0 = 1$) during the stirring process. Both definitions, the local Lagrangian strain rate and time averaged Lagrangian strain rate, provided consistent predictions of *RF*. From here on, we will refer to the time averaged Lagrangian strain rate as the strain rate.

(f). We calculated the distribution of strain rates $f\left[\bar{\dot{\gamma}}(t_r)\right]$ at any average residence time from the ensemble of strain rates at that average residence time.

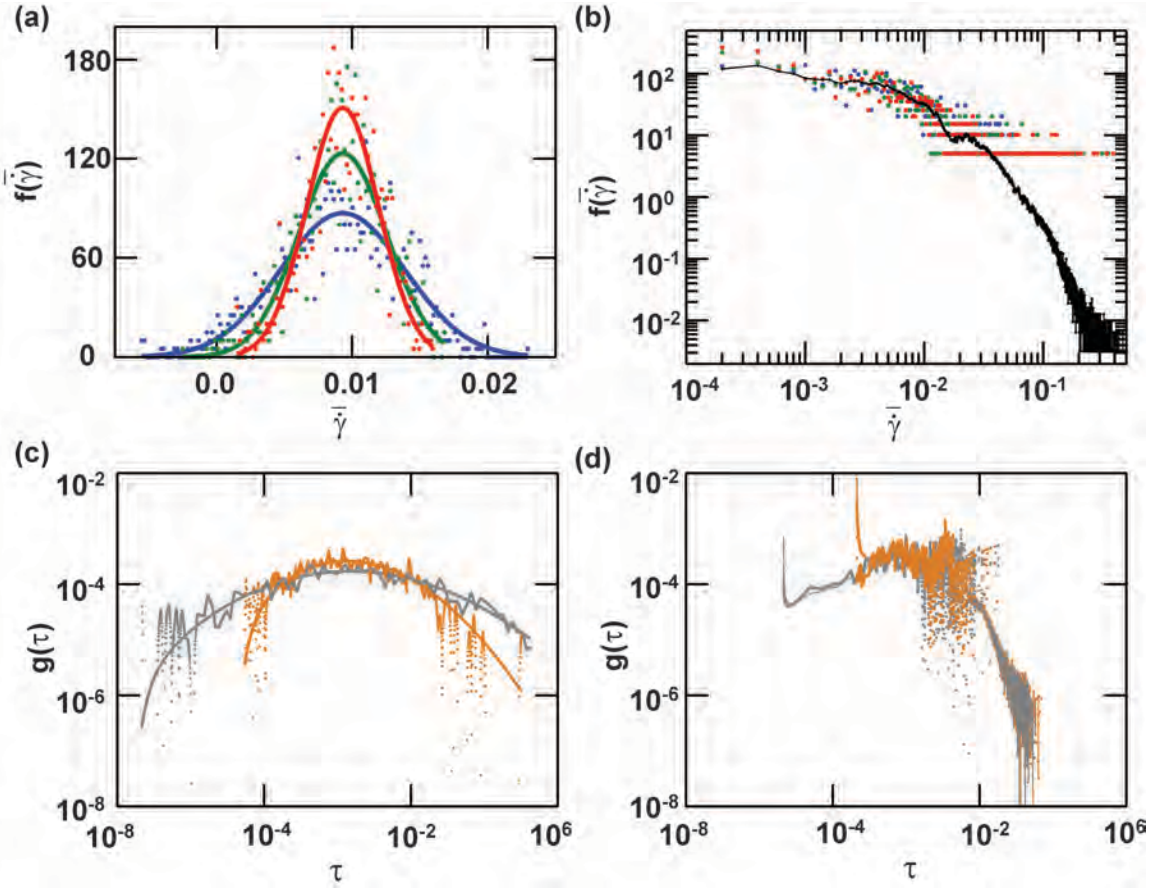

**Fig 5:** Strain rate and mixing time distributions: **(a-b)** Distribution of Lagrangian strain rates in the chaotic flow (a) at $\langle\bar{\dot{\gamma}}\rangle t = 3.72$ (violet), $\langle\bar{\dot{\gamma}}\rangle t = 7.44$ (green), $\langle\bar{\dot{\gamma}}\rangle t = 11.16$ (red), and in the non-chaotic flow (b) at $\langle\bar{\dot{\gamma}}\rangle t = 116$ (violet), $\langle\bar{\dot{\gamma}}\rangle t = 174$ (green), $\langle\bar{\dot{\gamma}}\rangle t = 232$ and (red). The dots represent the strain rate data from the line element simulations. The solid lines in (a) represent the Gaussian fit given in equations 17, 18 and show the evolution of the distribution of strain rate with time. The strain rate data from simulations in (b) shows that the non-chaotic flow settles to a single strain rate distribution after some time. The black line is obtained by using the simulation data at all time points to evaluate the distribution of strain rates (based on the assumption that the strain rate distribution settles onto a single curve after early time variations). **(c-d)** Distribution of the mixing times when $\tau_m$ is 0.02 ( orange – $D = 10^{-6}$, gray – $D = 10^{-9}$), in (c) the chaotic flow and in (d) the non-chaotic flow. The solid lines of the corresponding color were obtained from the Gaussian fit to strain rate distribution in the case of chaotic flow, and the black line for the non-chaotic flow.

Figure 5 presents the distribution of strain rates as a function of the axial length of the stirring section of the channel, calculated in this manner. The distribution of strain rates (dots - blue, green and red) in the chaotic flow [figure 5(a)] and the non-chaotic flow [figure 5(b)] are shown at three residence times. In the chaotic case, the mean strain rate of the distribution quickly reached the asymptotic value of $\dot{\gamma}_{asym} = 0.0093$ (equation 17) and the variance decayed inversely with the average residence time as shown in equation 18. Fitting $f\left[\bar{\dot{\gamma}}(t_r)\right]$ of the chaotic flow to a normal distribution with the mean strain rate of 0.0093, and variance as described in equation 18, we found that the best fit (least square error $R^2 = 0.85$) value of the prefactor $A = 0.9$. These are plotted in figure 5(a) (solid lines).

$$\langle\bar{\dot{\gamma}}\rangle \approx \dot{\gamma}_{asym}\left[1 - \exp\left(-2\dot{\gamma}_{asym} t_r\right)\right] \approx \dot{\gamma}_{asym} \qquad \ldots 17$$

$$\langle\bar{\dot{\gamma}}^2\rangle - \langle\bar{\dot{\gamma}}\rangle^2 = \frac{A\dot{\gamma}_{asym}}{t_r}, \dot{\gamma}_{asym} t_r > 1 \qquad \ldots 18$$

Equations 17 and 18 point to a stochastic sampling of strain rates with the mean strain rate relaxation time proportional to $\frac{1}{\dot{\gamma}_{asym}}$. This sampling arises from the ergodic character of chaos

which is characteristic of all globally chaotic flows. We have also verified this behavior in a chaotic sine flow, and we expect it to hold for all globally chaotic systems (5). Thus, in such systems, one only need to estimate two parameters $\dot{\gamma}_{asym}$ and $A$ to model the distribution of strain rates.

The non-chaotic flow [Figure 5(b)], on the other hand, has a strain rate distribution which does not change with the residence time $t_r$ after an initial transient. We do not expect all non-chaotic flows to have non-varying strain rate distribution after the initial transience. However, due to the periodicity of the current non-chaotic flow, the line elements experience similar strain rates when revisiting a region in the flow field. So, the strain rate distribution remains the same. We note that the noise in the strain rate distribution is high because of the number of line elements used to obtain the distribution was not sufficient. Further, the orbits have different periods and different spatial location might be visited at the chosen residence times in Figure 5(b). Hence, we increase the statistics of the distribution and reduce the noise, by combining the data at all times to generate non-varying strain rate distribution in the non-chaotic flow, as shown in the black curve. The average strain rate for the non-chaotic flow is $\langle \bar{\dot{\gamma}} \rangle = 0.0145$.

Having evaluated the Lagrangian strain rate distribution for both the flows, we will proceed to modify the Ranz model to incorporate these characteristics of the flows.

Modifying the Ranz model for distribution of strain rates

The Ranz model describes the convective-diffusive process in a linear flow with two parameters, strain rate and initial strand width $s_0$. As noted earlier, to adapt the Ranz model for non-linear flows, we incorporate the distribution of strain rates. To this end, we will evaluate the distribution of mixing time $g[\tau(t_r)]$ at a given axial position (or average residence time) in the

stirring region, in the chaotic and non-chaotic flows using Eq. (17), and using the relation in equation 19.

$$g(\tau) = f(\bar{\dot{\gamma}})\frac{d\bar{\dot{\gamma}}}{d\tau} \qquad \ldots 19$$

Figure 5(c, d) shows the mixing time distribution for diffusivities $D = 10^{-6}, 10^{-9}$ at $\tau = 0.02$ for the chaotic and non-chaotic flows, respectively. We first note that the distribution of mixing times grows wider with residence time for both flows, even though the distribution of strain rates narrows (chaotic flow) or remains constant (non-chaotic flow). This widening distribution of mixing time with residence time is expected because the mixing time increases (exponentially or by power law) with residence time. With this understanding, we expect that at a fixed $\tau_m$, the breadth of the mixing time distribution will increase with decreasing diffusivity because solutes with lower diffusivity require longer residence times to achieve the same $\tau_m$. For example in the chaotic case, when $\langle\bar{\dot{\gamma}}\rangle t_r >> 1$, $g(\tau_m) \sim \frac{1}{\tau_m\sqrt{8\pi A\langle\bar{\dot{\gamma}}\rangle t_r}} \sim \frac{1}{\sqrt{k_1 - k_2 \log D}}$, [where $k_1$ and $k_2$ are independent of diffusivity, obtained using equation 11] decreases with decreasing diffusivity. This scaling points to the trend that near the maximum of the mixing time distribution the value of $g(\tau)$ decreases with decreasing diffusivity. Accordingly, as the height of the distribution decreases, the width of the distribution $g(\tau)$ increases, thus leading to persistent growth of the tails as function of decreasing diffusivity.

In the non-chaotic flow [Figure 5(d)], on the other hand, since the distribution of strain rates does not change with time, $g(\tau) \approx \frac{f(\bar{\dot{\gamma}})\bar{\dot{\gamma}}}{2\tau}$ (when $\bar{\dot{\gamma}} t_r >> 1$), does not change with change in diffusivity

of the solute. Thus, but for minor differences (corresponding to small $\bar{\dot{\gamma}}$), the mixing time distribution of the non-chaotic flow is independent of diffusion.

We now develop the modified Ranz model for reversal processes in general flows. We define the quantitative measures of irreversibility as the weighted average of the respective measure for individual strands, weighted by the different experiences in the flow, as represented by the distribution of strain rates. We evaluate the modified Ranz return fraction ($RF_{MR}$) as the weighted average over all strain rates or mixing times as shown in equation 20.

$$RF_{MR}(\tau_m) = \int_{-\infty}^{\infty} RF\left[\tau\left(\bar{\dot{\gamma}}\right)\right] f\left(\bar{\dot{\gamma}}\right) d\bar{\dot{\gamma}} = \int_{0}^{\infty} RF(\tau) g(\tau) d\tau \qquad \ldots 20$$

In the calculations required for evaluating $RF_{MR}$ in equation 20, we use the Gaussian distribution approximation of strain rates for chaotic flow with the parameters given in equations 17 and 18, and the non-varying distribution of strain rates [black line, figure 5(b)] for non-chaotic flow. Maximum selectivity is defined using $RF_{MR}$ in equation 5.

Results and Discussion

In this section, we will compare the predictions of the modified Ranz model discussed above for quantitative measures of reversibility with the results obtained in the model chaotic and non-chaotic flows. Once again, we use the simple inlet condition of the solute being present in the left half of the channel cross-section.

For the chaotic flow, we evaluate the weighted return fraction (equation 20) using the Gaussian fit to the strain rate distribution described in figure 5(a), $\left\langle \bar{\dot{\gamma}} \right\rangle$ for the chaotic flow and the best fit value of $s_0$ of 1.7. The average mixing time $\tau_m$ is obtained using average strain rate $\left\langle \bar{\dot{\gamma}} \right\rangle$ at a

given residence time and diffusivity. Figure 6(a) and (b) plot the *RF* from the modified Ranz model with that from the numerical simulation of the chaotic flow as a function of the average non-dimensional residence time [Fig. 6(a)] and mixing time [Fig. 6(b)]. These figures highlight that the modified Ranz model predicts the trends in the decay of return fraction for different diffusivities quantitatively at early times for different diffusivities, and qualitatively at late times.

Similarly for non-chaotic flow, we compare *RF* in figures 6(c) and 6(d) predicted by the modified Ranz model with results from the strain rate distribution shown in figure 5(b). The fit parameters were $\langle \bar{\dot{\gamma}} \rangle$ and $s_0$. The best fit was achieved at $s_0 = 1.4$. The comparison of the model and numerical simulation in figure 6(c) as a function of average non-dimensional residence time shows that the prediction of the modified Ranz model is quantitative at early times, and qualitative at late times. Observing in the mixing time domain [Fig. 6(d)] we note that *RF* collapse to a single curve at lower diffusivities. However, unlike the chaotic flow where we identified A, the prefactor in the strain rate variance dependence on residence time, we have not identified an extra parameter from the strain rate distribution in the non-chaotic case to predict the entire curve accurately at all times.

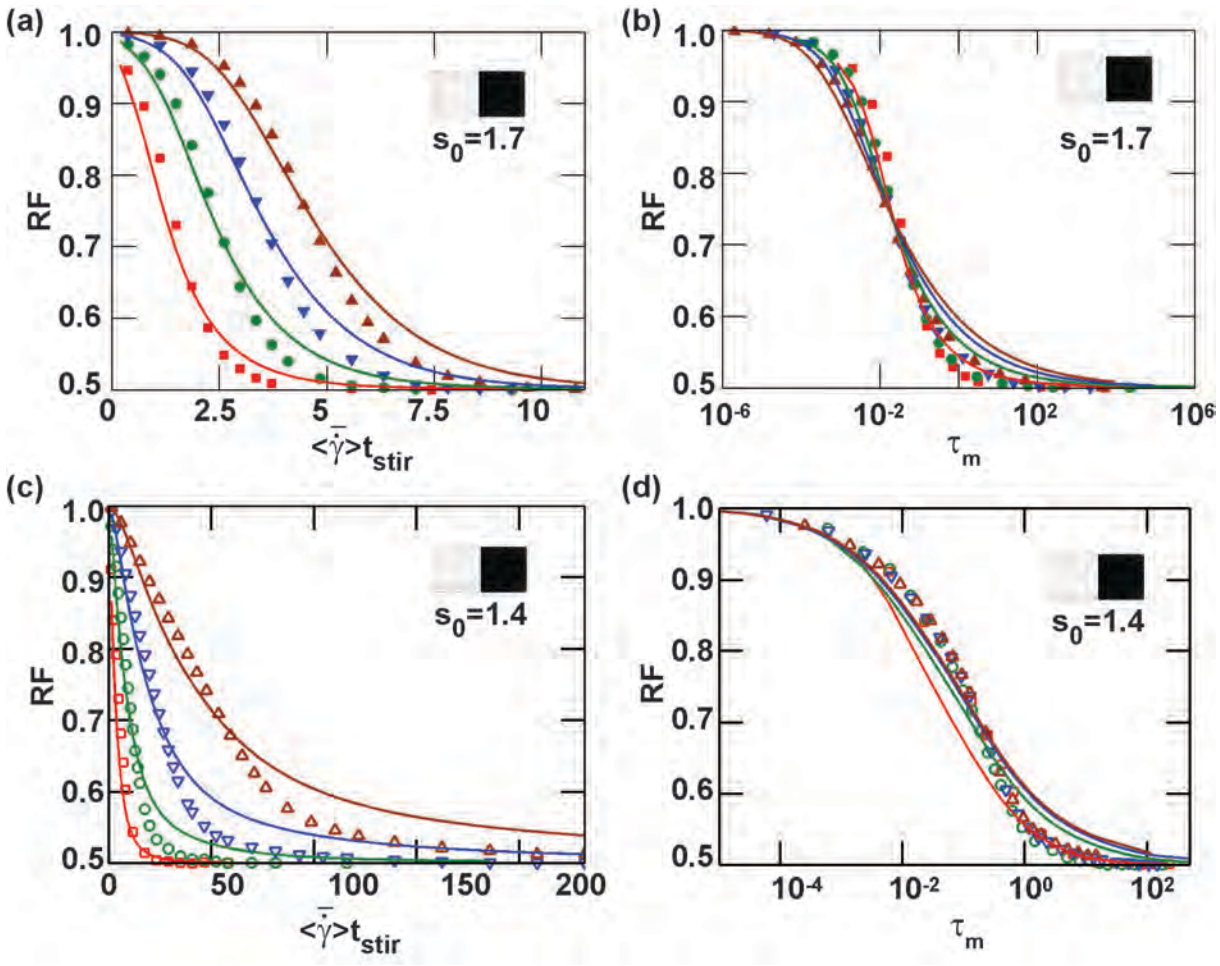


**Fig 6:** Return Fraction (*RF*) using modified Ranz model with distribution of shear rates: **(a-b)** *RF* in Chaotic flows. Comparison of *RF* obtained from numerical simulation (symbols) with the predictions of the modified Ranz model (lines) based on the Gaussian fit to the distribution of shear rates [Fig.6 (a)] as a function of the average non-dimensional residence time $\langle\dot{\gamma}\rangle t_{stir}$ in the flow (a), and as a function of mixing time $\tau_m$ (b). **(c-d)** *RF* in non-chaotic flows. Comparison of *RF* obtained from numerical simulation (symbols) with the predictions of the modified Ranz model (lines) based on the distribution of shear rates [Fig. 5(b), black line], as a function of the average non-dimensional residence time in the flow (c) as a function of mixing time $\tau_m$ (d). The inlet condition for (a-d) is the right half of the cross-section is filled with the solute, as shown in the inset. The initial strand width used in the modified Ranz model is given in the inset. Diffusivities represented are $10^{-4}$ (red squares), $10^{-5}$ (dark green circles), $10^{-6}$ – (blue inverted triangles), $10^{-7}$ (brown triangles).

We now turn our attention to a different inlet concentration distribution, namely a concentration field in which the solute is present in top half of the cross section only. We evaluate the

prediction of the Ranz model modified due to distribution of strain rates in this case. The figure of merit of the convective diffusive irreversibility, *RF* is plotted as a function of the residence time in figure 7(a, b). The value of best fit parameter $s_0$ was 1.7 in the chaotic case, and 3.6 in the non-chaotic case. As seen in figure 7(a) in the chaotic case, the prediction of the modified Ranz model was quantitative at early times, and qualitative at late times. For the non-chaotic flow in figure 7(b) at early times, the model predicts the behavior quantitatively. However, at late times , the model does not predict the behavior even qualitatively. The numerical results show a second slower rate of decay in RF at late times for the higher Peclet numbers.

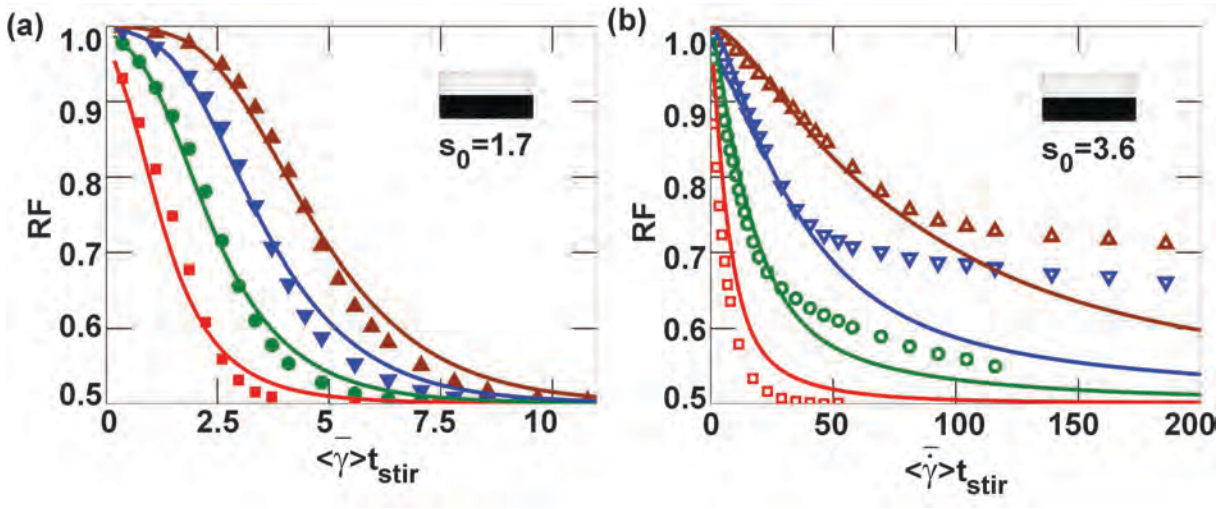


**Fig 7:** *RF* using Ranz model modified using distribution of strain rates for an inlet concentration distribution with solute in the top half of the cross section.**(a,b)** *RF* is plotted as a function of the average non-dimensional residence time $\langle\bar{\dot{\gamma}}\rangle t_{stir}$ in chaotic flows (a) and non-chaotic flows (b). Comparison of *RF* obtained from numerical simulation (symbols) with the predictions of the modified Ranz model (lines) based on the Gaussian fit to the distribution of strain rates [Fig.5 (a)] in the chaotic flow (a), and with predictions of modified Ranz model based on strain distribution shown in Fig. 5(b) in the non-chaotic flow (b). The initial strand width used in the modified Ranz model is given in the inset. Diffusivities represented are $10^{-4}$ –red square, $10^{-5}$ dark green circle, $10^{-6}$ – blue inverted triangle, $10^{-7}$ – brown triangle, solid symbols are used for the chaotic case and open symbols for the non-chaotic case.

Thus, at least based on these two inlet concentration distributions, we find that chaotic flow is not dependent on the inlet concentration distribution, as long as the ratio of fluxes in the solute to the total flux, $\frac{s_0}{\lambda_0}$ and the width of solute region, $s_0$ are similar. In order to understand the reason behind the second slower rate of decay in RF in non-chaotic flows, we will explore concentration profiles of the non-chaotic flow for this inlet condition. We will try to understand if the periodic nature of trajectories in the non-chaotic flow is responsible for this behavior and incorporate its impact into another modification of the Ranz model.

**Periodicity of the flow field**

To understand the difference in late stage decay of RF in the non-chaotic flow in the two cases, as observed in figure 6(b) and figure 7(b), we evaluate the difference in evolution of the concentration profiles in the two cases during the reversal process for the same residence time $\left(\bar{\gamma}t_r = 58\right)$ in figure 8. The two inlet concentration fields are shown in figure 8(a)i and 8(b)i. In both cases, the mixing has progressed very well near the orange outer trajectory during the stirring and un-stirring process, and the intermediate region contains poorly mixed region, and well mixed regions. The greatest difference between the cases is around and within the yellow inner trajectory. For the case (a) with solute (white, c=0) in the top half of the cross-section, no mixing is observed for the concentration field within the yellow inner trajectory in the figures 8(a)i-iii. For the case (b) with solute in the high half of the cross section (figure 8(b)i-iii), the mixing has progressed within and around the inner trajectory, albeit as slowly as the intermediate region.

Having laid out our preliminary observation of the differences in the concentration profiles, we probe the underlying flow characteristics that cause these differences. Our non-chaotic flow has

spiral trajectories. These trajectories, when observed in the transverse cross-section, are closed periodic orbits, each with a different period. Solute present on such periodic trajectory mixes faster along the streamline (diffusion is aided by convection) relative to the direction perpendicular to the streamline (diffusion only). So, solutes on the inner trajectory (near the center) take order of diffusive time scale ( $t \sim \frac{H^2}{D}$ ) to reach the outer trajectory (near the walls). As a result of periodic orbits of the transverse flow of the non-chaotic flow, qualitatively different mixing characteristics are observed for different inlet concentration distribution.

By overlaying the trajectories on the cross-sectional inlet concentration distributions (Figure 8), we note that in case (a), the interface between solute and no solute region does not intersect all orbits, especially those near the center of the vortex, whereas in case (b), the interface will intersect all the orbits. In the context of mixing between the black and white regions, on the one hand, regions where the solute/non-solute interface of the inlet concentration intersects the orbits turn gray faster due to mixing along the streamline direction. On the other hand, the regions where the interface of the inlet concentration does not intersect the orbits (central region within the yellow inner trajectory in case (b)) remain convectively disconnected since the mixing along the streamline direction does not bring it into contact with the solute. Hence, the choice of inlet concentration distribution affects the average concentration along each streamline. In case (b), the yellow inner trajectory with no solute remains black, while the orange outer trajectory is a shade of gray. The central core in case (b) region thus waits for diffusion perpendicular to the streamline direction to be homogenized with the rest of the cross-section. In case (a), the regions of poor mixing (right at the center of the vortex, and in a narrow region between the two trajectories) are due to nearly zero velocity in those regions. Hence, these regions are dominated strongly by diffusion than convection (in both cases a, b).

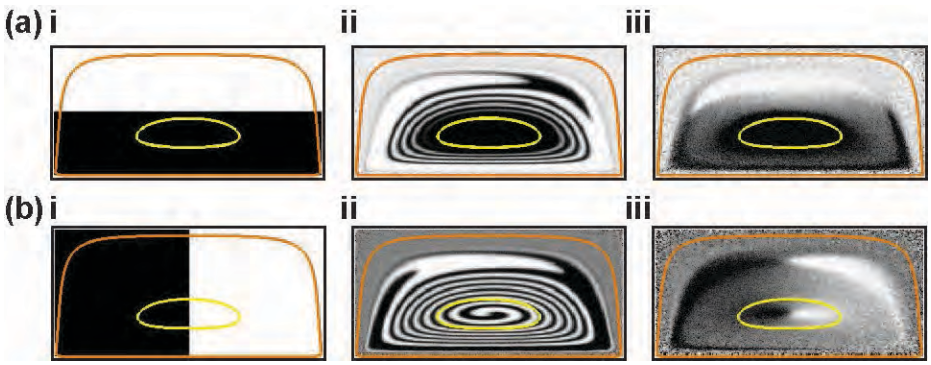


**Fig 8:** Impact of periodic streamlines and inlet conditions in non-chaotic flow. **(a, b)** Evolution of concentration distribution at the inlet (i), after stirring for $\left(\bar{\dot{\gamma}}t_r = 58\right)$ (ii) and after stirring and un-stirring (iii) when the inlet condition contains solute in the top half of the cross section as in (a) and in the right half of the cross-section as in (b). Two streamlines, one near the outer boundary of the cross section and one near the center point of the cross-sectional flow are highlighted in orange.

Thus, for inlet conditions with average streamline concentration (concentration averaged along each streamline) varying across the streamlines (case (a)), we expect two time scales: i. the initial stage of convection aided mixing along the streamlines, ii. the late stage diffusion dominated mixing perpendicular to the streamlines. For inlet conditions with uniform average streamline concentration [case (b)] has a single stage of mixing – a convective-diffusive mixing process.

In contrast, we note that a fully chaotic flow is ergodic in nature. And, the chaotic flow studied here is almost globally chaotic. Hence, the chaotic flows experience also experience a single rate of decay of return fraction during the reversal process as seen in figure 6(a) and 7(a).

Modifying the Ranz model for periodicity of flow field

Rhines & Young (19) previewed our qualitative observation above. They showed that, in closed streamline flows, if concentration averaged along every streamline $\bar{c}_0(\psi)$ (equation 21) is exactly the same for all streamlines, then mixing is dominated by stretching in the flow.

$$\bar{c}_0(\psi) = \frac{\oint c_0 ds/\nabla\psi}{\oint ds/\nabla\psi} \qquad \ldots 21$$

Where $\psi$ is the streamfunction of the flow and $c_0$ is the inlet concentration distribution, *ds* is the infinitesimal arclength along the streamline. In our case, it is the streamfunction of the transverse secondary flow.

Otherwise [like in the case shown in figure 10(c)i], the early time mixing occurs due to simple strain like stretching until $\left(\frac{\dot{\gamma}s_0^{\,2}}{D}\right)^{1/3}\frac{1}{\dot{\gamma}}$ whereas the late time behavior $t \sim \frac{s_0^2}{D}$ is a result of diffusion perpendicular to the streamlines. Following this work of Rhines & Young, we predict a simple trend for SCDI in non-chaotic flows when $\frac{\partial \bar{c}_0(\psi)}{\partial\psi} \neq 0$. At early times, based on the Ranz model for simple shear flow, we predict that *RF* follows the master return curve until $t \sim \left(\frac{\dot{\gamma}s_0^{\,2}}{D}\right)^{1/3}\frac{\tau_{ss}}{\dot{\gamma}}$ from equation 11). After the early time mixing is complete, and diffusion dominates the decay of reversibility, we predict that *RF* follows the master return curve defined for pure diffusion as given in equation 22.

$$RF = 2c'\frac{\lambda_0'}{s_0'}\sum_n \frac{1}{(n\pi)^2}\sin^2\left(n\pi\frac{s_0'}{\lambda_0'}\right)\exp\left[-\left(2n\pi\frac{s_0'}{\lambda_0'}\right)^2 2\tau_d\right] + \frac{s_0'}{\lambda_0'} \qquad \ldots 22$$

where $c'$ is the prefactor representing the *RF* at the end of shear stretching, $s_0'$ is new strand width, and period $\lambda_0'$ and $\tau_d$ is mixing time for pure diffusion (equation 11). Using these two parameters as fit parameters, we can attempt to predict the decay of *RF* for both regimes.

Results and Discussion

We tested the prediction of the Ranz model with the inlet condition given in Fig. 8(a). We compared the prediction of *RF* for the first and second stage on two different mixing time domains. The initial strand width fit parameter, $s_0 = 3.6$ is used for the early time behavior. The early time behavior is captured in the mixing time domain for simple shear flow (equation 11, $\tau_{ss_m}$) as shown in figure 9(a). The late time *RF* prediction as described in equation 22, involves two fit parameters, the "initial" strand width $s_0' = 1.1$ for the second stage, and *RF* prefactor $c' = 0.485$. Different values of initial strand width parameter for early time and late time behavior are expected because they correspond to different "inlet" conditions. $s_0$ is used for actual inlet concentration profile and is somewhat close to the width of cross-section. $s_0'$ is used for the concentration profile prior to the second stage of mixing. The second stage was captured in the mixing time domain for pure diffusion (equation 11, $\tau_d$) in figure 9(b). The comparison at early times indicates that the model predicts the behavior accurately for lower diffusivities, but the prediction is not accurate at higher diffusivities (red squares), possibly because of absence of clear transition between shear dominant stage and diffusion dominant stage for highly diffusive solutes. The model captures the trends at late times quantitatively.

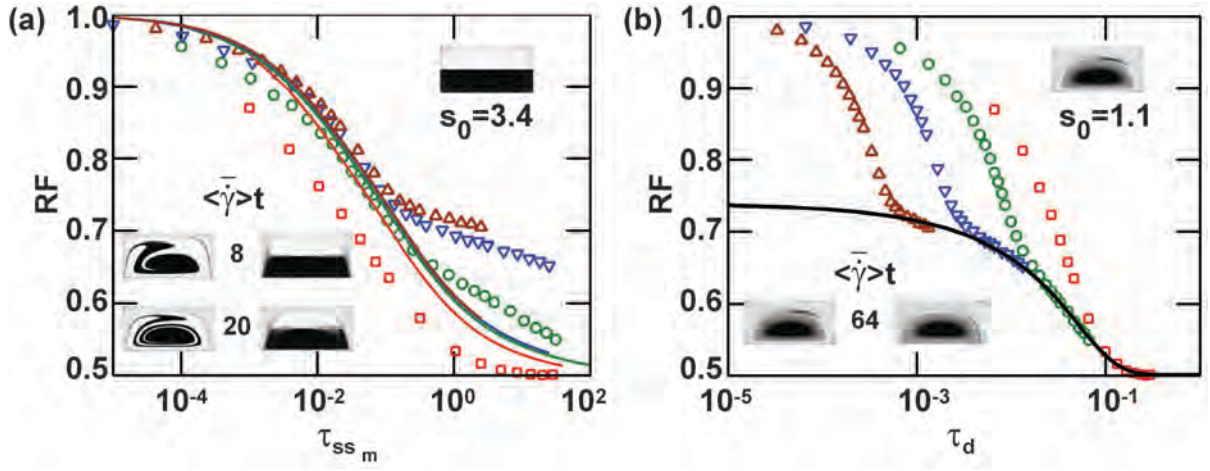

**Fig 9:** Impact of periodic streamlines and inlet conditions in 3D non-chaotic duct flow. **(a)** Return Fraction (*RF*) for early stage of shear dominated mixing in non-chaotic flow for the inlet condition shown in the top inset; this initial condition leads to non-uniform concentration averaged over a streamline ($\bar{c}_0(\psi)$). The symbols represent *RF* data from the simulation and lines represent the modified Ranz model at different diffusivities (red – $10^{-4}$, green – $10^{-5}$, blue– $10^{-6}$, brown – $10^{-7}$). *RF* is plotted as function of mixing time based on simple shear $\tau_{ss_m}$ (equation 11). **(b)** *RF* for the same flow and initial condition during the second stage of diffusion dominated mixing. The color code for the predictions of simulation (symbols) and modified Ranz (lines) are the same as in (a). *RF* is plotted as function of mixing time based on pure diffusion $\tau_d$ ( equation 11). The fit parameter $s_0$ is shown in the top right inset. The lower right insets show the concentration profiles for a diffusive solute ($D = 10^{-7}$) in the non-chaotic flow at different average non-dimensional residence time.

**General Initial Conditions**

We now go beyond the simplest inlet concentration distribution with half the cross section filled with solute. While the non-chaotic flows are expected to exhibit multi stage return behavior as described in the section above, the chaotic flows, due to their ergodicity are expected to have single stage return fraction behavior. Thus, the chaotic flows allow us to test the generality of the Ranz model for any inlet condition. We divided the inlet cross-section into 32 square boxes (box height = 0.25), with 8 squares along the width, and 4 along the height of the channel cross-section and studied 32 different inlet concentration distributions. As shown on the left side of the first panel of figure 10(a), for example, concentration profile labelled "row 1, col 1" represents an inlet concentration distribution in which a square box of height 0.25 in the top left corner (first row and first column of the 4 x 8 boxes) is filled with solute uniformly (white or 1), and the rest of the cross-section is without solute (black or 0). Similarly, we define all 32 inlet concentration distributions. The left side on the second panel of figure 10(a) shows the individual concentration profiles after stirring and un-stirring their respective inlet concentration distribution (shown in the first panel) for $\bar{\gamma}t_r = 3$. On the right side of two panels, we have

captured the composite picture of *RF* at the two conditions, the inlet and at $\bar{\dot{\gamma}}t_r = 3$. The color within each box of the composite image represents the gray scale value of *RF* for stirring and un-stirring the corresponding inlet concentration distribution for $\bar{\dot{\gamma}}t_r$. As expected, at the inlet, the composite picture has white color in each box, since $\bar{\dot{\gamma}}t_r = 0$. At $\bar{\dot{\gamma}}t_r = 3$, the composite image shows a different color (grayscale) in each box. The color of the box in the first row and first column represents the *RF* [using Eq. (12)] obtained using the concentration profiles named "row 1, col 1" at the inlet (left side, first panel) and concentration profile named "row 1, col 1" after stirring and un-stirring that initial condition for $\bar{\dot{\gamma}}t_r = 3$ (left side, second panel). The difference in the evolution of return fraction amongst the boxes is visible from the difference in the color in the boxes.

The evolution of composite *RF* is captured in the inset of figure 10(b) for three different residence times. We now test the Ranz model (no modifications) for such diverse initial conditions, by plotting the average *RF* from these boxes as a function of the mixing time along with the master return curve. The fit parameter used in mixing time calculation that change with inlet concentration distribution, $s_0$ was evaluated to be 0.26, close to the box height in the inlet concentration distribution. We find that the master return curve obtained from the Ranz model (black line) predicts the decay of the average *RF* from all the boxes at the four different diffusivities (solid symbols) very closely. We have shown the minimum and maximum *RF* for every mean value plotted using error bars on the symbols to represent the variety of return behavior that lies beneath the mean behavior. Even though the Ranz model (and the modified Ranz model, not shown here) captures the mean behavior of *RF* closely, the diversity of *RF* behavior in individual boxes cannot always be captured well by using the local linear flow model and its modifications, such as incorporating the distribution of strain rates for strands originating

in the box. We think that this is because the early time flow and the associated evolution of *RF* from small boxes is not an extensional flow. Additionally, effect of non-linear flow characteristics is not captured in this model.

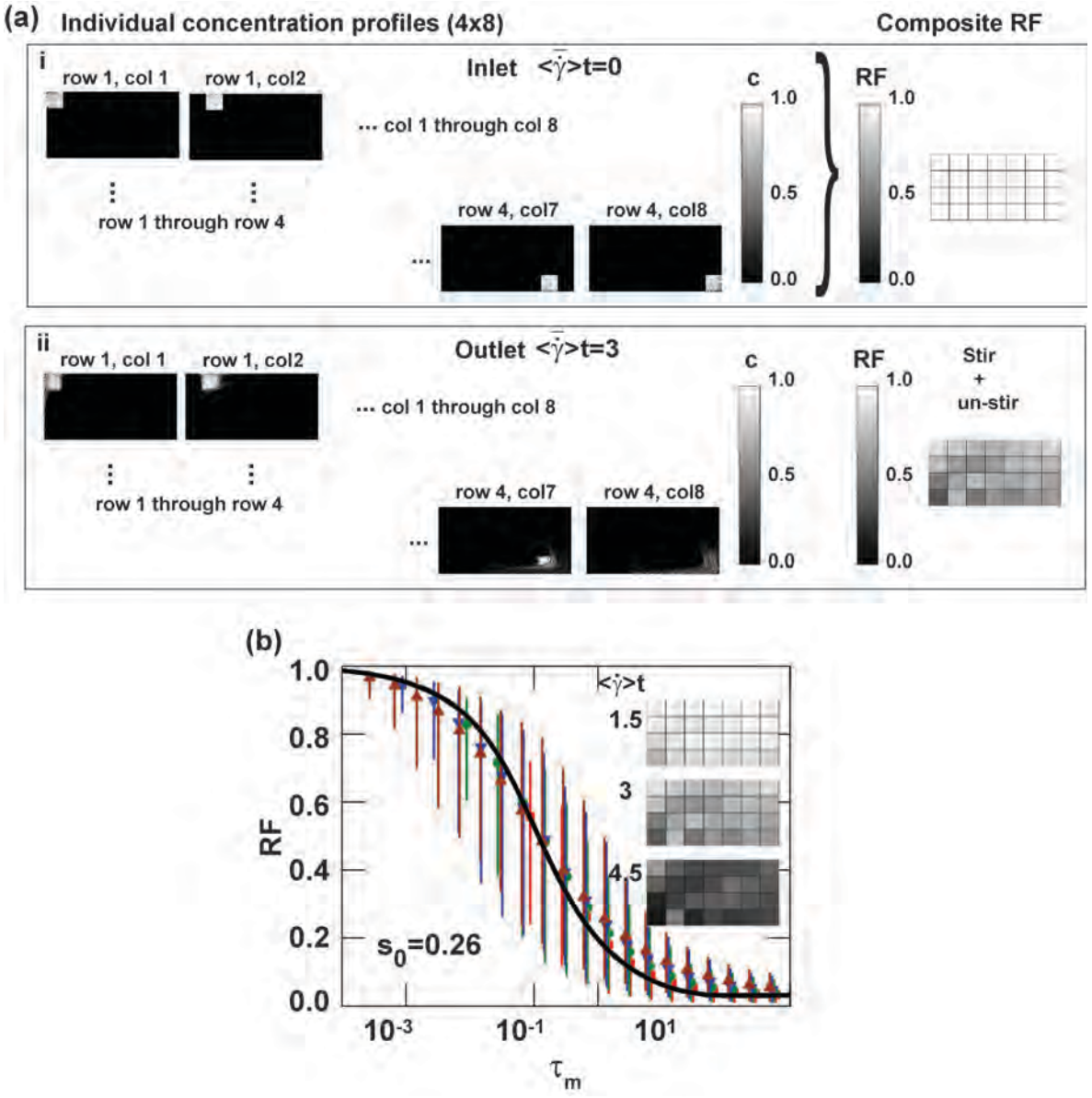


**Fig 10:** SCDI for smaller regions of solute in the chaotic flow. **(a)** Concentration profiles were evaluated within 32 square regions on a grid (4 high × 8 wide) covering the cross-section before stirring and after stirring + un-stirring. The label of each square region contains the row and column for that region as shown in the two panels. For each region, the inlet

distribution was stirred and unstirred for $\langle\bar{\dot{\gamma}}\rangle t$. Inlet (i) and outlet (ii) distributions are shown for boxes of the panels for the chaotic flow with $D = 10^{-7}$. *RF* is evaluated from each these 32 conditions for a given $\langle\bar{\dot{\gamma}}\rangle t$ and is combined into a composite gray scale image, with the shade in each box representing the *RF* in that region (i.e., the fraction of the solute that started and returned to that region), as shown on the right of the panels. **(b)** Comparison of *RF* averaged across all 32 regions (symbols) with the predictions of the Ranz model (black line), as a function of mixing time $\tau_m$. The mixing time is defined using $\langle\bar{\dot{\gamma}}\rangle$ and the best fit parameter $s_0$ = 0.28. The vertical line on each symbol represents the range of variation in *RF* (lowest to highest) across all regions. Diffusivities represented are $10^{-4}$ (red squares), $10^{-5}$ (dark green circles), $10^{-6}$ – (blue inverted triangles), $10^{-7}$ (brown triangles).

For the non-chaotic flow, we have not compiled the composite performance of similar set of smaller inlet conditions due to differences in transition time points for different spatial locations. As discussed in section V.2, the return behavior of non-chaotic flow in such cases has a multi-staged decay pattern.

***Separation Efficiency***

Having studied *RF* in detail, we now turn to assimilating our understanding about the character of the flow on return fraction to its effect on separation of solutes of different diffusivities. Maximum selectivity or separation efficiency, $\phi_{\max}$ follows the characteristics observed for the figure of merit, *RF*. However, unlike *RF*, $\phi_{\max}$ is a rate independent quantity, providing an unbiased comparison of flows with different mixing characteristics for its utility for implementing SCDI. From equation 2, we know that, $\phi_{\max}$ depends on the diffusivities of the two solutes, and the ratio of flux of solute to the total flux through the channel cross section.

We will compare the predictions of $\phi_{\max}$ from the simple Ranz model and modified Ranz model for the different cases that we have discussed in Section IV and V.

For the case of solute in the left half of the cross section, we plotted maximum selectivity as a function of the ratio of diffusivities in Figure 11(a). The simple Ranz model for linear flows predicts the unity in return behavior in the transformed Ranz space. Hence, the separation efficiency curve (black line) for a given inlet condition is a single line, independent of the actual value of diffusivities, and is a function of only the ratio of diffusivities. We find that the Ranz model prediction is higher than that obtained for our chaotic or non-chaotic flows. The numerical data shows that both chaotic (green squares) and non-chaotic flows (red squares) have poorer but similar maximum selectivity relative to linear flows. Since *RF* decays differently with mixing time for different diffusivities, the maximum selectivity would depend on the diffusivities of two solutes as well as the character of flow in general non-linear flows. The modified Ranz model (red line - chaotic and green line – non chaotic) due to distribution of strain rates predicts the numerical simulations quite well for the studied range of diffusivities ($10^{-4}$ to $10^{-7}$).

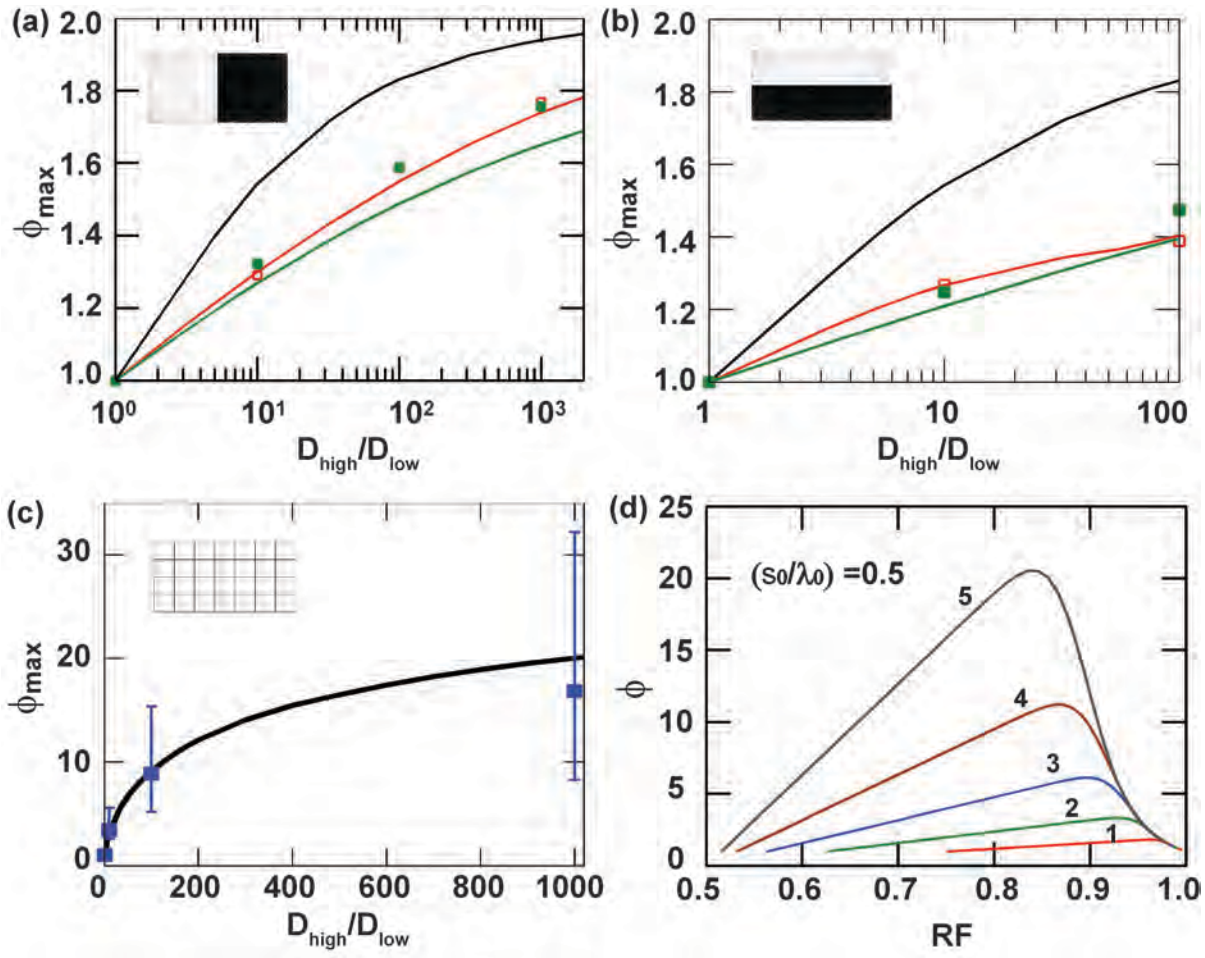


**Fig 11:** Selectivity: **(a,b)** Plot of maximum selectivity $\phi_{max}$ as a function of ratio of the diffusivities for a case where solute is present in left half of cross-section (a), and for a case where solute is present in top half of cross-section (b). The maximum selectivity obtained from numerical simulation are plotted as symbols (red squares – non-chaotic, green squares – chaotic, and $D_{high} = 10^{-4}$ in (a) and $D_{high} = 10^{-5}$ in (b)) . Predictions of $\phi_{max}$ by the simple Ranz model is black line, and by the Ranz model modified for distribution of strain rates in red (non-chaotic) and green (chaotic) solid lines in (a) and (b). **(c)** Comparison of maximum selectivity (averaged over all 32 regions, shown as symbols) and the prediction of the Ranz model (black line) as a function of the ratio of diffusivities (c). The vertical line on each symbol represents the range of variation in $\phi_{max}$ (lowest to highest) across all 32 regions. **(d)** Plot of selectivity $\phi$ as a function of *RF* in the ideal separation device, as predicted by the Ranz model Each line represents the number of times the solution is passed through the device, each time with fresh dilutant solution (red – 1 pass, green –2 passes, violet –3 passes, (d). brown – 4 passes, gray – 5 passes). The inlet condition is half the cross-section is filled with the solute.

For the case of solute in the top half of the cross section, we plotted maximum selectivity as a function of the ratio of diffusivities in Figure 11(b). Since we noted poor accuracy of prediction of RF curve for the non-chaotic case for highest diffusivity in Figure 9(a), we considered a smaller diffusivity range ($10^{-5}$ to $10^{-7}$) for testing the prediction of separation efficiency from the modified Ranz model for multi-stage decay of RF. The numerical data shows that both chaotic (green squares) and non-chaotic flows (red squares) have poorer but similar maximum selectivity relative to linear flows (black line, Ranz model). The modified Ranz model due to distribution of strain rates predicts the numerical simulations well for the studied range of diffusivities.

For the case of smaller inlet conditions (Figure 11(c), 32 square boxes, Section V.3), we evaluated the average separation efficiency from all 32 inlet conditions in the chaotic flow for all pair of diffusive solutes between $10^{-4}$ to $10^{-7}$. Additionally, we calculated the maximum and minimum separation efficiency, and plotted the data as a function of ratio of diffusivities. We find that the Ranz model predicts the average separation efficiency curve behavior fairly closely. However, we note that the Ranz curve does not predict the highest separation efficiency achieved in numerical experiments by solutes present in corner near wall regions. We think this difference could be difference in early time flow characteristics especially for solute of lower diffusivity.

Apart from understanding the behavior of chaotic and non-chaotic flows in context of SCDI, the Ranz model provides the guidelines for defining the characteristics of flow and initial condition to achieve very high selectivity quickly. One such flow is the baker's map – it is a chaotic map with a single lyapunov exponent. Hence it achieves the highest maximum selectivity predicted by Ranz, at an exponentially fast rate. Performing multiple passes into the separation device in

such a flow one can achieve high yield (*RF*) along with a high selectivity $\phi = \left( \frac{RF(D_{low})}{RF(D_{high})} \right)_{t_{stir}}$.

To perform multiple passes, the purified fraction of solute mixture from the outlet of the device is fed into the inlet of the next device, along with fresh dilutant. Figure 11(d) shows a plot of selectivity versus yield for several passes for the baker's map. Thus, one can make a judicious choice of the number of passes based on their requirement of yield and selectivity. Furthermore, reducing the ratio of area occupied by the solute to the entire cross-section can greatly improve selectivity.

***Conclusions***

We have tested the Ranz model and its modifications to understand the irreversibility of chaotic and non-chaotic flows under a variety of conditions. These models use a two-dimensional time reversible flow field and a strand which is infinitely long thus identifying the direction with strongest concentration gradient as the most important direction for studying convective diffusive irreversibility. The success of the Ranz model is that it is a unified treatment of chaotic and non-chaotic flows, treating the central challenges identified in the paper in a step-by-step manner. The model with the assumption of linear flow and parameters – strain rate and initial strand width is general. With inputs about the character of strain rate distribution, and the inlet conditions, the model brings out the influence of the qualitatively different flow characteristics such as ergodicity and exponential rate of separation of chaotic flows relative to periodic trajectories and power rate of separation of non-chaotic flows on the measures of mixing. Based on comparison of the model with results of numerical solution, we have identified the means to optimize the separation technique SCDI.

The limitations of these models are the flow characteristics that the modifications of the Ranz model failed to incorporate. General non-linear flows exhibit characteristics such as folding and merging of two or more strands. Further, some studies find that the presence of walls (20-21) changes the mixing character of chaotic flows at late times. The impact of these characteristics on the different inlet conditions is unaccounted for in the Ranz model and its modifications.

In conclusion, we studied here the interplay of convection and diffusion present in the reversal process (stirring + diffusion followed by un-stirring + diffusion) in chaotic and non-chaotic flows. From the work of Ranz, we identified mixing time as a tool that quantifies the progression of mixing and puts all classes of flows on the same plane – a purely diffusive framework. It is indeed a direction of time in the sense that mixing can never progress in the direction where the mixing time decreases. Furthermore, it enabled us to observe reversal as a mixing process in the mixing time domain. Our study uncovered the influence of coupling of average linear flow nature and the distribution of strain rates on the measures of mixing and irreversibility. We also uncovered the effect of distribution of inlet concentration in a flow with periodic trajectories, and proposed a modification in the late time decay of reversibility and mixing measures due to pure diffusion in such cases. Using the model, we were able to understand the principle required to build a microfluidic device for separation that is fast and efficient and can be optimized for the system of solutes under consideration – namely designing a chaotic separation device with single rate of stretching, like the chaotic baker's map.

*Appendix*

**A.1 Return Fraction after homogenization**

After stirring and un-stirring for , the solute is homogenized across the cross-section, and *RF* takes a final plateau value. We denote the region of the cross-section where the solute is originally found as region of interest (ROI*)*. We note that the total flux of solute passing through the channel is constant. Using Eq. (3), after homogenization at time $t_r$, the concentration is uniform and is given by

$$c_{ave} = \frac{N_+(t_r) - N_-(t_r)}{ua} . \frac{UA}{N_{tot}} \qquad \ldots \text{A1.1}$$

Hence the total flux of solute at time $t_r$ is given by

$$N_+ = c_{ave} \int_{CS} \frac{ua}{UA} . N_{tot} \, dxdy \qquad \ldots \text{A1.2}$$

where the integral is over the entire cross-section. Total flux can also be evaluated at the inlet.

$$N_+ = c_0 \int_{ROI} \frac{ua}{UA} . N_{tot} \, dxdy \qquad \ldots \text{A1.3}$$

Using these equations, we find that

$$\frac{c_{ave}}{c_0} = \frac{\int_{ROI} \frac{ua}{UA} . N_{tot} \, dxdy}{\int_{CS} \frac{ua}{UA} . N_{tot} \, dxdy} \qquad \ldots \text{A1.4}$$

Further, using the definition of $RF_c$ ,we find that

$$RF_c(t_r) = \frac{c_{ave}}{c_0} \qquad \ldots \text{A1.5}$$

Thus, Eq. (A1.4) and (A1.5) show that return fraction based on concentration and flux, both decay to the same final value, the ratio of fluxes in the region of interest to the flux in the entire cross section.

**References**


[1] Arnold VI., Comptes . Rendus. de I Academie des Sciences 261: 3719-3722, (1965)

[2] Aref H., Journal of Fluid Mechanics 143: 1-21, (1984)

[3] Ottino JM, Cambridge: Cambridge University Press, (1989)

[4] Aref H, Jones SW, Physics of Fluids A-Fluid Dynamics 1: 470-474, (1989)

[5] Sundararajan P, Kirtland J, Koch D, Stroock A, Physical Review E, 86,4, (2012)

[6] Taylor GI, Illustrated Experiments in Fluid Mechanics,pp. 47-54 , (1972)

[7] Heller JP. American Journal of Physics 280: 348-353,(1960)

[8] Dutta P, Chevray R, Journal of Fluid Mechanics 285: 1-16, (1995)

[9] Ranz WE., Aiche Journal 25: 41-47, (1979)

[10] Stroock AD, Dertinger SKW, Ajdari A, Mezic I, Stone HA, Whitesides GM, Science 295: 647-651, (2002)

[11] Stroock AD, McGraw GJ, Philosophical Transactions of the Royal Society of London Series a-Mathematical Physical and Engineering Sciences 362: 971-986, (2004)

[12] Kirtland JD, McGraw GJ, Stroock AD, Physics of Fluids 18: 13, (2006)

[13] Kirtland JD, Siegel CR, Stroock AD, New Journal of Physics 11: 075028, (2009)

[14] Batchelor GK, Townsend A, England: Cambridge University Press (1956)

[15] Villermaux E, Stroock AD, Stone HA., Physical Review E 77: 4, (2008)

[16] Meunier P, Villermaux E, Journal of Fluid Mechanics 476: 213-222, (2003)

[17] Cocke WJ, Physics of Fluids 12: 2488 (1969)

[18] Batchelor GK, Proceedings of the Royal Society of London Series a-Mathematical and Physical Sciences 213: 349 (1952)

[19] Rhines PB, Young WR, Journal of Fluid Mechanics 133: 133-145 (1983)

[20] Gouillart E, Kuncio N, Dauchot O, Dubrulle B, Roux S, Thiffeault JL, Physical Review Letters 99 (2007)

[21] Lebedev VV, Turitsyn KS., Physical Review E 69 (2004)

# CHAPTER 3

# EXPERIMENTAL STUDY OF CONVECTIVE DIFFUSIVE IRREVERSIBILITY IN LAMINAR FLOWS

## *Introduction*

Time reversibility of Stokes flows was experimentally demonstrated by G.I Taylor [1] using a cylindrical couette cell by stirring and un-stirring a dye in a very viscous fluid. The time reversibility of Stokes flows comes from the linearity and quasi-steady nature of the governing Stokes equations. We note that stirring refers to motion of the fluid driven by means of pressure gradient, moving boundary etc, whereas mixing refers to the coupled action of stirring and diffusion of a solute. Heller [2] observed that the reversibility of Stokes flows can be used to separate solutes with different diffusivities. This concept of separation by convective diffusive irreversibility (SCDI) involves the following: a) stir a mixture of solutes with different diffusivities into a dilutant using a Stokes flow for a time $t$, b) un-stir by reversing the motion of Stokes flow used for stirring for the same time $t$, c) collect the partially purified solute. If the time $t$ is chosen such that low diffusivity solute is not mixed, only stirred, but the high diffusivity solute is mixed, then upon un-stirring the solutes, the low diffusivity comes back to its original volume, whereas the high diffusivity is mixed across the entire volume, and hence, fails to return to original volume. The fraction of solute that comes back to the original volume is called return fraction.

Aref & Jones [3] numerically studied SCDI in an eccentric cylinder geometry that allowed them to compare the behavior of chaotic and non-chaotic Stokes flow. They observed that return fraction in chaotic flows decayed faster than non-chaotic flows.

We used the Ranz model [4], for studying reversal using chaotic and non-chaotic sine flows to generalize the results obtained by Aref & Jones [3] and found that the behavior of both chaotic and non-chaotic flows can be treated in a unified manner. Sundararajan et al [5] identified the figure of merit for this process, separation efficiency, and showed that the presence of distribution of strain rates in these general non-linear flows lowers the separation efficiency relative to linear flows.

In this work, we will focus on the experimental demonstration of Stokes flow reversibility and irreversibility by two possible mechanisms, namely diffusion and inertia. An extension of this work is developing a separation device based on the idea of SCDI for several chemical and biochemical applications. With the growth of lab-on-a-chip devices, the ability to convert these operations in to micro-fluidic devices that can be easily integrated with the other tools in a feasible manner has become a crucial engineering need. To satisfy this need for separation, there are several devices that perform capillary electrophoresis [6], dielectrophoresis [7], isotachophoresis [8, 9], magnetic beads [10], membrane based separation [11] etc. However, most of these devices use external electric, magnetic field or membranes for separation. Brody & Yager [12] developed the H-filter that uses pure diffusion to separate solutes by flowing the mixture of solutes into a channel along with a dilutant through the other inlet [Fig. 1(a)]. The high diffusivity solute diffuses across the cross-section to a greater extent relative to the low diffusivity solute. While this device represents the simplest implementation of SCDI, and can achieve the highest separation efficiency, one disadvantage is that length of the channel required to achieve separation of solutes by pure diffusion across the width of the channel is order of several meters. This is because the microfluidic regime is characterized by low Reynolds number and high Peclet number, where Peclet number is defined as $Pe = \frac{Uh}{D}$, and Reynolds

number is defined as $Re = \frac{Uh}{\nu}$. $h$ is the height of channel, $U$ is the maximum axial velocity in the channel, $D$ is the diffusivity of the solute, and $\nu$ is the kinematic viscosity of the fluid. The $Pe$ is the ratio of convection to diffusion in a flow, and $Re$ is the ratio of inertial to viscous stresses.

In the microfluidic context, we propose to implement a separation strategy based on SCDI that is passive (i.e without external fields) or external membranes, and much faster than pure diffusion. We will study SCDI in chaotic and non-chaotic flows. We will identify the different sources of irreversibility apart from diffusion, such as inertial and geometric irreversibility that might hinder the effective implementation of this strategy. We will identify a microfabrication technique that will reduce the effect of geometric irreversibility. The experimental results will serve as a test of the generality and feasibility of Ranz model and the modified Ranz model that we used for understanding SCDI. Finally, we will experimentally explore the inertial irreversibility of chaotic and non-chaotic flows during the reversal process.

***Experimental Method***

**Strategy**

Our strategy for implementing SCDI employs fore-aft symmetry in a microchannel. We note that fore-aft symmetry is another consequence of linearity and quasi-steady nature of the Stokes equations, when the boundary conditions are fore-aft symmetric like the flow around a sphere. Figure 1(a) is a schematic diagram of SCDI in a channel.

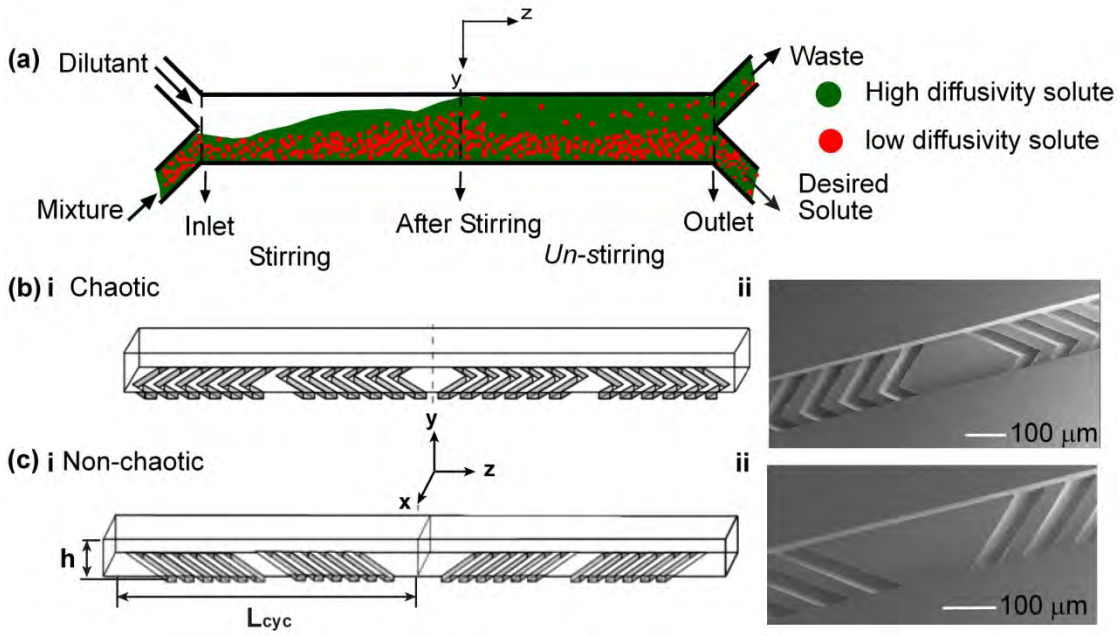


**Fig.1:** Separation by convective diffusive irreversibility (SCDI) in a microchannel: **(a)** A schematic showing a continuous flow separation strategy. A mixture of two solutes (red – low diffusivity solute, green – high diffusivity solute) is fed into a channel along with a dilutant. In the stirring section of the device, the low diffusivity solute gets stirred while the high diffusivity solute gets mixed. Then, they are un-stirred in the un-stirring section of the device. The low diffusivity solute returns to the original cross-sectional position after un-stirring, while high diffusivity solute gets mixed in the entire cross-section and does not return. At the outlet, the desired high diffusivity solute is partially purified and separated from the waste. **(b-c)**. Implementation of SCDI using fore-aft symmetry in (b) a chaotic flow (c) a non-chaotic flow. (b)i. Schematic of the staggered patterns of herringbone shaped grooves that result in a transverse chaotic stirring, and the reflection about the $z = 0$ plane results in transverse un-stirring. ii. SEM of a silicon fore-aft symmetric micro-channel with staggered herringbone grooves. (c)i. Oblique grooves create transverse non-chaotic stirring and its mirror image results in transverse non-chaotic un-stirring. ii. SEM of a silicon fore-aft symmetric micro-channel with oblique grooves. Each cycle of length $L_{cyc}$ consists of 12 grooves, the height of the channel h, is defined from half the groove depth to the top of the channel.

The mixture of solutes with different diffusivities (red- low diffusivity, green – high diffusivity) are fed into the channel along with a dilutant, stirred and then un-stirred as they flow through the

stirring section and un-stirring section of the channel and finally separated out as partially purified solute and waste. The mid-plane of the channel is at $z = 0$. In order to implement stirring and un-stirring using chaotic and non-chaotic flows, we use the staggered herringbone grooves (chaotic) and the oblique grooves (non-chaotic) [13] in the stirring section and their mirror reflection in the un-stirring section [Fig. 1(b)i, Fig 1(c)i]. The numerical simulation of these flows [14, 15] model the transverse flow produced by the grooves as transversely slipping floors. Hence, the fore-aft symmetric grooves produce transverse stirring $u_{x,y}(x, y, -z)$ in the first half of the channel, and transverse un-stirring $\left[u_{x,y}(x, y, z) = -u_{x,y}(x, y, -z)\right]$ in the second half of the channel. The direction of the axial flow in the channel is not reversed $\left[u_z(x, y, z) = u_z(x, y, -z)\right]$, thus resulting in a continuous flow separation device with ease of extraction of the partially purified solute.

**Fabrication of the device**

The most important challenge in fabricating the device is ensuring the geometric reversibility of the grooved structures. Geometric reversibility (fore-aft symmetry) is affected by several characteristics: variation in the shape of the grooves, depth of grooves, depth of channel and misalignment of the grooves axis and the channel axis. We explored different fabrication techniques to identify a strategy with lowest amount of geometric irreversibility.

Soft lithography using SU-8 photoresist and PolyDiMethylSiloxane (PDMS)

Soft lithography created features with significant variation in height of the channel and grooves. Further, channel area might change along the length of the channel (for long channel) due to pressure gradients, introducing geometric irreversibility in such a system.

Microfabrication in glass

Using isotropic etching of glass by Hydrofluoric acid was used to create multi-layer channel with grooves (rectangular channel layer, and groove layer). However, due to isotropic etching, the shape of the desired herringbone shaped grooves was not well realized, and hence was expected to not provide efficient transverse stirring. Further, inefficient masking of the edges of the glass channel by the silicon mask layer resulted in large scale defects along the channel. Hence, this method is not the ideal candidate for fabricating a separation device based on SCDI.

Microfabrication in silicon

Deep Reactive Ion Etching (DRIE) created mutli-layer topology with the least variation in groove and channel depth. It also did not alter the shape of the grooves, and preserved the fore-aft symmetry of the grooves. Hence, this method of fabrication was chosen to develop the microfluidic separation device.

The fabrication of channel involves the following: Two high resolution chrome masks define the channel and groove geometry. Silicon oxide layer of 0.7 microns is thermally grown on MOS cleaned silicon wafers. Positive photoresist (S1813, Shipley Microposit) is spun on the silicon oxide layer. Mask pattern with channels is exposed on the photoresist using a standard contact aligner and then developed and descumed. The exposed channel pattern on silicon oxide is etched away using Reactive Ion Etching (RIE) with $CHF_3$ and $O_2$ plasma, exposing the patterns of the channel in silicon. The photoresist is stripped away using oxygen plasma, and a different positive resist, SPR 220-3 (Megaposit) is spun on the patterned silicon oxide mask. The groove mask is then used to pattern the SPR 220-3 layer. The alignment is done using a standard contact aligner with an accuracy of 2 microns, thus, restricting misalignment of the channel and the groove patterns to less than $0.05^{o}$. The grooves are exposed on the photoresist and the

pattern is developed and descumed. The grooves are etched into the exposed silicon to a depth of 22.15 um using DRIE (standard Bosch process) with SPR 220-3 as the soft mask. The resist mask is stripped using oxygen plasma and exposing the channel region and etched groove region. This pattern is now etched again using DRIE (with some fine tuning of etch and clean times) for a depth of 51.6 um creating the desired geometry as shown in the SEM of chaotic and non-chaotic channels in Figure 1(b)ii, and 1(c)ii. The channels have isolated random defects whose dimensions are less than 5 $\mu m$. Holes are sand-blasted at the inlet and outlets, and the silicon oxide mask is then wet-etched using HF. The silicon wafer is then bonded to a 200 $\mu m$ thick borofloat glass wafer. Finally, nanoports (Upchurch Scientific) are bonded to backside of silicon and fitted with tubing.

**Materials and measurement of properties**

We used a mixture of glycerol and water in different ratios to obtain solutions of different viscosity. The mixture's pH is maintained at 8 by using tris (hydroxymethyl)aminomethane base and HCl (Fisher Scientific) to make a 20mM Tris-HCl buffer solution. The mixture is well homogenized by mixing the glycerol water mixture for 24 hours, following by heating at 60 $^{o}$C for a few hours and then mixing again for 4-5 hours. Using stock solutions of Sodium salt of Fluorescein, (Molecular Weight, 376.27 *Da*, source Fisher Scientific) and Fluorescein IsoThioCyanate labeled dextran (Molecular Weight, 2 *MDa*, source Sigma-Aldrich) in 20 mM Tris-HCl buffer solution in water, we made 25 $\mu M$ solutions of the solute in glycerol-water mixture. We matched the density of the fluorescent and non-fluorescent solution by heating and then mixing for several hours. The final density matching was confirmed. We measured the kinematic viscosity of the different glycerol water solutions using Ubbelohde viscometers, and

the diffusivity of the fluorescent solutes in the solutions of different viscosity using Multi-Photon Fluorescence Recovery After Photobleaching (MP-FRAP), developed by Brown et al [16].

**Experimental Setup**

The experimental setup consisted of the following a) a pressure delivery system with inline filters to feed clean fluorescent and non-fluorescent solution at maintain steady and equal flow rates into the two inlets of the microfluidic device, b) microfluidic separation device, c) inverted confocal microscope (Zeiss 510), on whose stage the microfluidic device is mounted for imaging the cross-section of the channel as the solute is stirred and un-stirred in the channel d) weighing balance to measure the mass flow rate from the outlet of the microfluidic device. The weighing balance is connected to Labview for obtaining a time series of mass of the solution leaving the microfluidic device.

We conducted the experiments in channels with different mixing protocols defined by the groove structures in the channels. A set of six grooves is a half cycle [Fig. 1(b)i, Fig. 1(c)i], and the length of stirring is defined using the number of cycles. We studied convective diffusive irreversibility in chaotic channels with 1,2,3 and 4 cycles and in non-chaotic channels with 1,2,3,4 and 6 cycles at different $Pe$ while keeping $Re \sim 0.04$. We also conducted experiments in the chaotic and non-chaotic channels with 1 cycle of stirring and un-stirring to study the inertial effects at different $Re$ while keeping $Pe > 10^6$ thereby decoupling convective-diffusive irreversibility and inertial irreversibility.

**Image Analysis**

The fluorescent images represent the distribution of concentration of the fluorescent solute. These concentration profiles are calibrated using a background image and fluorescent image of

the cross-section to remove the variation of intensity due to side walls, reflection at interfaces and other optical effects. The average concentration (cross sectional concentraion profile) is matched across all concentration profiles of each experiment.

For the experiments conducted at $Re \sim 0.04$, we calculated return fraction as a measure of convective diffusive irreversibility. Return fraction was defined for each experiment for the concentration profile at the end of un-stirring as the ratio of total concentration of solute at the end of un-stirring inside the cross-sectional area where the solute originated to the total concentration of solute before stirring. Since the interface between the solute stream and the stream without solute does not lie exactly at the mid plane of the cross-section, we compute the average *RF* obtained from the left and right hand side of the interface. In order to obtain return fraction from the right side when the left side was filled with solute, we invert the concentration profile $(c' = 1 - c)$, where $c$ is the original normalized concentration profile $c'$ is the inverted concentration profile. Further we also calculate a measure of mixing – the variance of concentration distribution at the end of un-stirring. These observables together will characterize the behavior of chaotic and non-chaotic flows during the reversal process.

***Model and Simulation***

**Ranz model and the modified Ranz model**

To understand the behavior of chaotic and non-chaotic flows in the context of SCDI, we used a simple mixing model proposed by Ranz (4) which is briefly described here. The work of Ranz indicates that, for weak diffusion, mixing of a periodic array of bands of solute in linear flows can capture mixing in the more general nonlinear flows because 1) the folding by a general flow typically results in an approximate spatial periodicity $(\lambda)$ in the concentration field over short

distances, and 2) the flow is approximately linear over short distances. We use extensional flow as the local linear flow in the chaotic flow, and a simple shear flow as the local linear flow in the non-chaotic flow. Using these assumptions, we can transform SCDI in a reversal process to a pure diffusion problem in a mixing time domain $\tau$ defined in Eq. (1).

$$\tau = \int_0^t D dt' / s(t')^2 \qquad \ldots 1$$

The mixing time, $\tau$ represents the time required for a distribution of solute undergoing pure diffusion to reach the same state as the distribution would in the flow under consideration after a dimensional residence time, $t$.

The mixing time for extension $\tau_{ext}$, simple shear $\tau_{ss}$, are

$$\tau_{ext} = \frac{D[\exp(2\dot{\gamma}t) - 1]}{2\dot{\gamma}s_0^2}, \quad \tau_{ss} = \frac{D[\dot{\gamma}t + (\dot{\gamma}t)^3/3]}{\dot{\gamma}s_0^2} \qquad \ldots 2$$

Where $D$ is the diffusivity of the solute, $\dot{\gamma}$ is the mean transverse strain rate in our flow and $s_0$ is the initial strand width.

The Ranz model predicts that all linear flows exhibit a universal decay of return fraction and variance in the mixing time domain. However, in chaotic and non-chaotic flows, the presence of distribution of strain rates destroys this universality of these observables in the mixing time domain. Instead the decay of return fraction has a lower slope and exhibits greater deviation from universal Ranz curve with lower diffusivity. This model captures the effect of convective-diffusive irreversibility in the limit of $Re \to 0$ (Stokes regime) using two fit parameters, the mean transverse strain rate in the flow $\dot{\gamma}$, and the initial strand width $s_0$.

Further, to quantify the separation of solutes of different diffusivities we define the separation efficiency in Eq. (3).

$$\phi\left(D_{high}, D_{low}\right) = Max\left(\frac{RF\left(t_{stir}, D_{low}\right)}{RF\left(t_{stir}, D_{high}\right)}\right)_{\forall t_{stir}} \qquad \ldots 3$$

It is the maximum of ratio of return fraction of solutes of two diffusivities with respect to the stirring time. The Ranz model predicts that the linear flows achieve the highest separation efficiency for a given pair of solutes and initial conditions. The modified Ranz model predicts lower separation efficiency for general non-linear flows with distribution of strain rates.

**Simulation**

Stroock [17] showed that transverse flow generated in a channel with oblique grooves can be described with an effective transverse slip velocity. Stroock & McGraw [14] and Kirtland & Stroock [15] have shown that the concentration profiles in the chaotic channel experimentally can be matched numerically using a superposition of an appropriate lid driven cavity flow and axial Poiseuille flow. We simulate the evolution of the concentration profiles of solutes whose *Pe* matches that used in the experiment with Lagrangian diffusive particle tracking [14, 15]. We chose the slip velocity for simulation by matching some feature of stretching in the first half cycle in the two flows. Briefly, the Lagrangian diffusive particle tracking method involves the following (a) populate the inlet flux of solutes using $10^6$ particles; (b) track the positions of the particles $\vec{x}$ in the chaotic and non-chaotic flows by solving for the particle trajectories $\frac{d\vec{x}}{dt} = \vec{u} + \vec{B}(t)$, where $\vec{u}$ is the velocity, and $\vec{B}(t)$ is the stochastic contribution to the velocity that represents diffusion; (c) obtain the concentration profiles by binning particle positions at chosen times, and dividing the flux in each bin by axial velocity in bin and the area of the bin.

We also obtain the distribution of Lagrangian strain rates in the chaotic and non-chaotic flow using the line-element simulation described elsewhere (Chapter 2). We find that $\langle \dot{\gamma} \rangle = 0.939 T_{cyc}^{-1}$ for chaotic case and $\langle \dot{\gamma} \rangle = 1.57 T_{cyc}^{-1}$ for the non-chaotic case. The numerical simulation provides us with the one fit parameter, the mean transverse strain rate $\langle \dot{\gamma} \rangle$. The other fit parameter, the initial strand width is chosen to obtain the best fit of the model to the data.

**Inertial Effects**

The inertial irreversibility arises from the non-linear $\left(\vec{u}.\vec{\nabla}\vec{u}\right)$ acceleration term in the Navier-Stokes equation given in Eq. (4).

$$\rho\left(\frac{\partial \vec{u}}{\partial t} + \vec{u}.\vec{\nabla}\vec{u}\right) = -\vec{\nabla}p + \mu\nabla^2\vec{u} \qquad \ldots 4$$

When the *Re* is very much smaller than 1, then the viscous terms balances the pressure term resulting in the linear Stokes equation. However, the limiting value of *Re* below which the Stokes approximation works well is still an open question for general flows. As suggested in [18] Re <1-5 is a valid approximation for Stokes regime for single phase flow. Flekkoy et al [19] observe inertial irreversibility even at $Re \sim 10^{-3}$ while performing a reversal experiment of a material line flowing past a cylinder in a Hele-shaw geometry. They find that the deviation of the material line after the reversal shows a linear dependence with *Re*.

The work by Dutta & Chevray [20, 21] studied the interplay of inertia and convective-diffusive irreversibility during reversal of chaotic flows for large amount of strain. In the chaotic reversal experiments and numerical simulation in an eccentric cylinder geometry, they compared the mean separation of particles (distance between initial and final position of particle after stirring and un-stirring a) diffusive particles with inertial effects b) diffusive particles without inertial

effects c) non-diffusive particles with inertial effects and found that a diffusive displacement with inertia was largely due to transience.

Here, we follow the work by Flekkoy et al [19] to decouple the effect of inertia from the diffusive irreversibility, and to achieve a regime with negligible inertial irreversibility. We will also characterize the behavior of the flow with increasing *Re*.

***Results and Discussion***

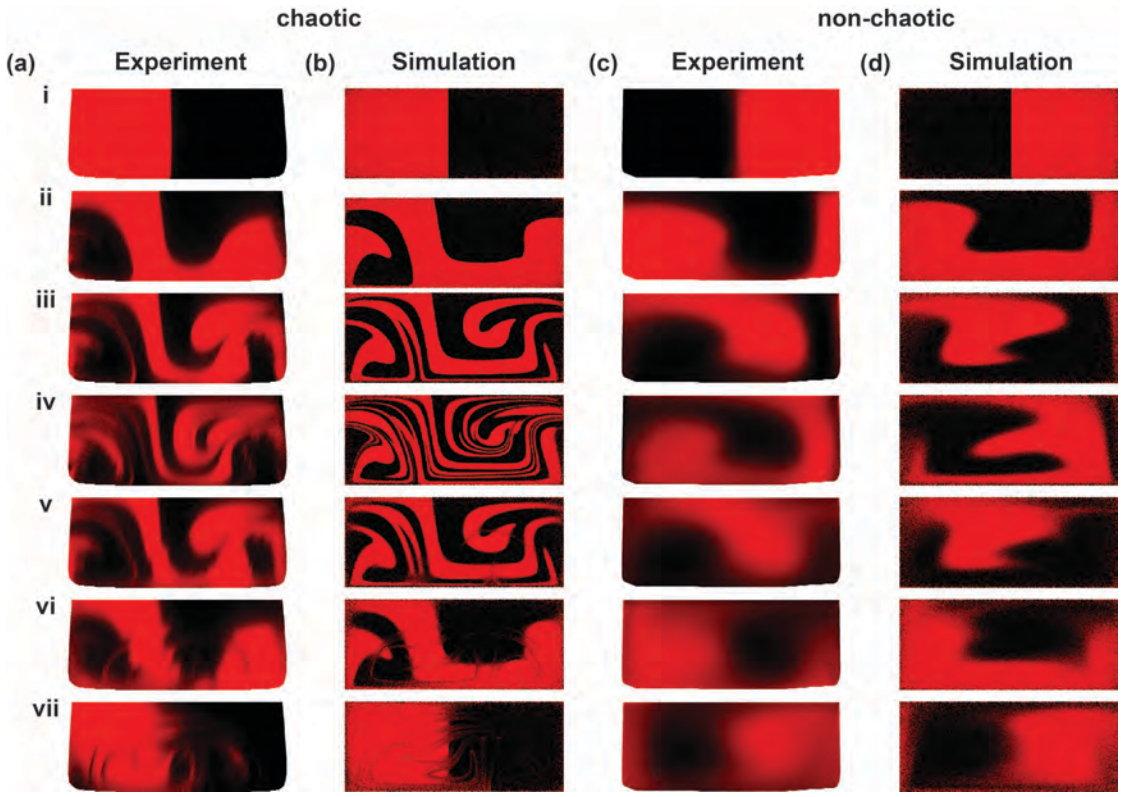


**Fig.2:** Comparison of concentration profiles during SCDI for 3 cycles: **(a-d)** Concentration profiles at the end of every cycle during the reversal of (a) chaotic flow obtained experimentally at $Pe = 3.4\times10^{6}$(b) chaotic flow obtained from numerical simulation at $Pe = 3.4\times10^{6}$ (c) non-chaotic flow obtained experimentally at $Pe = 3.7\times10^{4}$ (d) non-chaotic flow obtained from numerical simulation at $Pe = 3.7\times10^{4}$. The length of stirring section is 3 cycles. i represents the inlet condition, ii-iii represent stirring at the end of intermediate cycles, iv represents the concentration profile after stirring, v-vi represent

un-stirring at the end of intermediate cycles, and vii is the un-stirred concentration profile after 6 cycles of stirring and un-stirring. The solute is shown using red color. The slip velocity (0.12 times the maximum axial velocity) in the numerical simulation was chosen to match one or more features of interface (between red and black) at the end of the half cycle obtained experimentally.

The evolution of concentration profiles obtained from the experiments and the corresponding numerical simulation in the two flows is shown in Figure 2. The Peclet numbers in the two flows are different. Comparing the experiments and numerical simulation, we find that in both chaotic and non-chaotic cases, the numerical simulation create more stretching than that observed experimentally. Looking at the experimental results, we observe strongly non-uniform stretching in the chaotic flow [Fig. 2(a)iii-iv] with some regions with extremely thin strands, and other region with thick strands. As the flow un-stirs, the unstable manifolds [22] in the chaotic flow [Fig. 2(a)v-vii] is visible after seen as the diffusion along the unstable manifold results in convective diffusive irreversibility observed in chaotic flows. In the non-chaotic flow [Fig. 2(c)iii-iv], 3 cycles of stirring corresponds to early mixing time scales in non-chaotic flow. These concentration profiles show convective-diffusive irreversibility dominated by the effect of diffusion.

We seek to understand the influence of the chaotic and the non-chaotic flow using the modified Ranz model. We evaluate the mixing time for chaotic and non-chaotic flows using Eq. (2) using the Lagrangian mean strain rate of 0.939 $T_{cyc}^{-1}$ for both chaotic and non-chaotic values, and $s_0$=0.75$h$, where $h$ is the effective height of the channel defined as the height of the channel above half the groove depth [Fig. 1(b)]. In Figure 3(a,c) we compare the return fraction obtained from experiments (closed symbols) with the results from the numerical simulation (open symbols), the Ranz model (black line), and modified Ranz model (chaotic flow: green line

- $Pe$ ~$10^6$, blue line - $Pe$ ~$10^4$ ; non chaotic flow: red line – $Pe$ ~$10^4$). We use the same fit parameters mentioned above for numerical simulation.

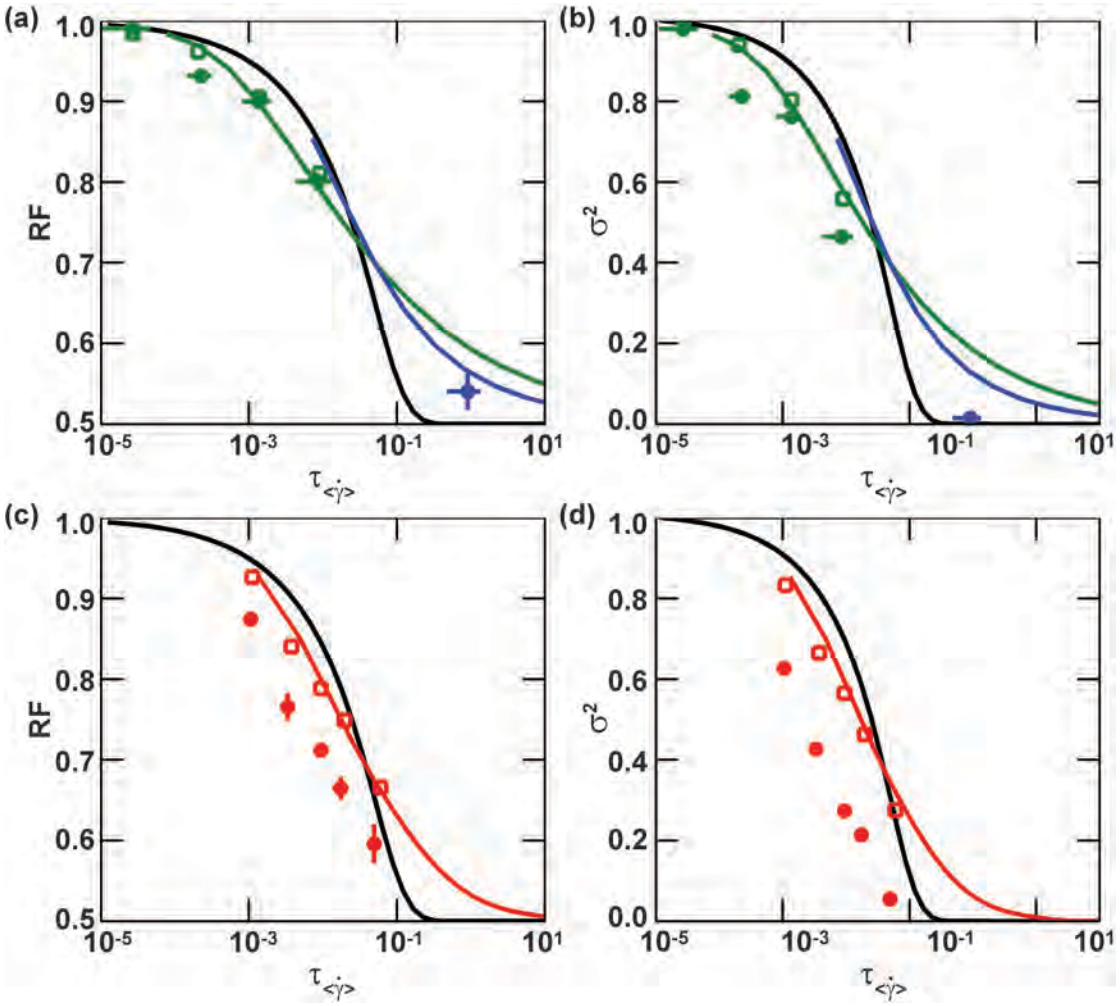


**Fig.3:** Comparison of experiments with simulation and model: **(a,c)** Average *RF* obtained from both chaotic (a) and non-chaotic flows (b) as a function of mixing time $\tau_{<\dot{\gamma}>}$ .**(b,d)** Variance of concentration distribution after un-stirring for both chaotic (b) and non-chaotic (d) flows as a function of mixing time $\tau_{<\dot{\gamma}>}$ . $\tau_{<\dot{\gamma}>}$ obtained using two fit parameters $\langle\dot{\gamma}\rangle = 0.939 T_{cyc}^{-1}, s_0 = 0.75h$, where $h$ is the height of the chaotic channel. The colors represent the following: green – chaotic flow at $Pe = 3.4\times10^6$, blue – chaotic flow at $Pe = 3.7\times10^4$, red – non-chaotic flow at $Pe = 3.7\times10^4$. The open symbols represent results from numerical simulation, closed symbols represent results from experiments, red blue and green curves represent the modified Ranz model (color representation given above). The black line represents the Ranz model.

In Figure 3(a,b), we observe that the behavior of chaotic flows follows the behavior observed in the numerical simulation both during early times (green symbols) and late times (blue symbol). Further, the modified Ranz model predicts the observed experimental decay of return fraction with the mixing time. In the case of the non-chaotic flow on the other hand, we observe that the experimental results do not follow Ranz curve or the modified Ranz curve relative to the simulation results for this choice of strain rate and strand width. We note that the slope of decay of *RF* observed experimentally is captured by the modified Ranz model. For the decay of variance of the concentration distribution at the end of the reversal process, we find a similar behavior in Figure 3(b) and 3(d). Once again, using the same fit parameters, we find that the behavior of chaotic flows (figure 3(b)) are better predicted than the non-chaotic flow (figure 3(d)) using modified Ranz and numerical simulation. We think that this error could arise partly from the diffuse interface at the inlet to the non-chaotic stirring. We also think that a more accurate match between experimental and numerical simulation would be obtained if we match the rate of interfacial growth rather than the features of interfacial shape.

We now turn to studying the effect of other sources of irreversibility. We identified geometric irreversibility and inertial irreversibility as the two sources of irreversibility that can couple with the convective-diffusive irreversibility to give different dynamics in comparison to the prediction in the Stokes regime.

**Geometric Irreversibility**

We note that the channel geometry is fore-aft symmetric with variations of about 4% in the effective height of the channel ($h$), and 6% variation in height of the groove. Hence, we assume

that their effects on the characterization of reversibility is negligible. We expect that the presence of geometric irreversibility would affect the behavior of chaotic flows more strongly than the non-chaotic flows.

**Inertial Irreversibility**

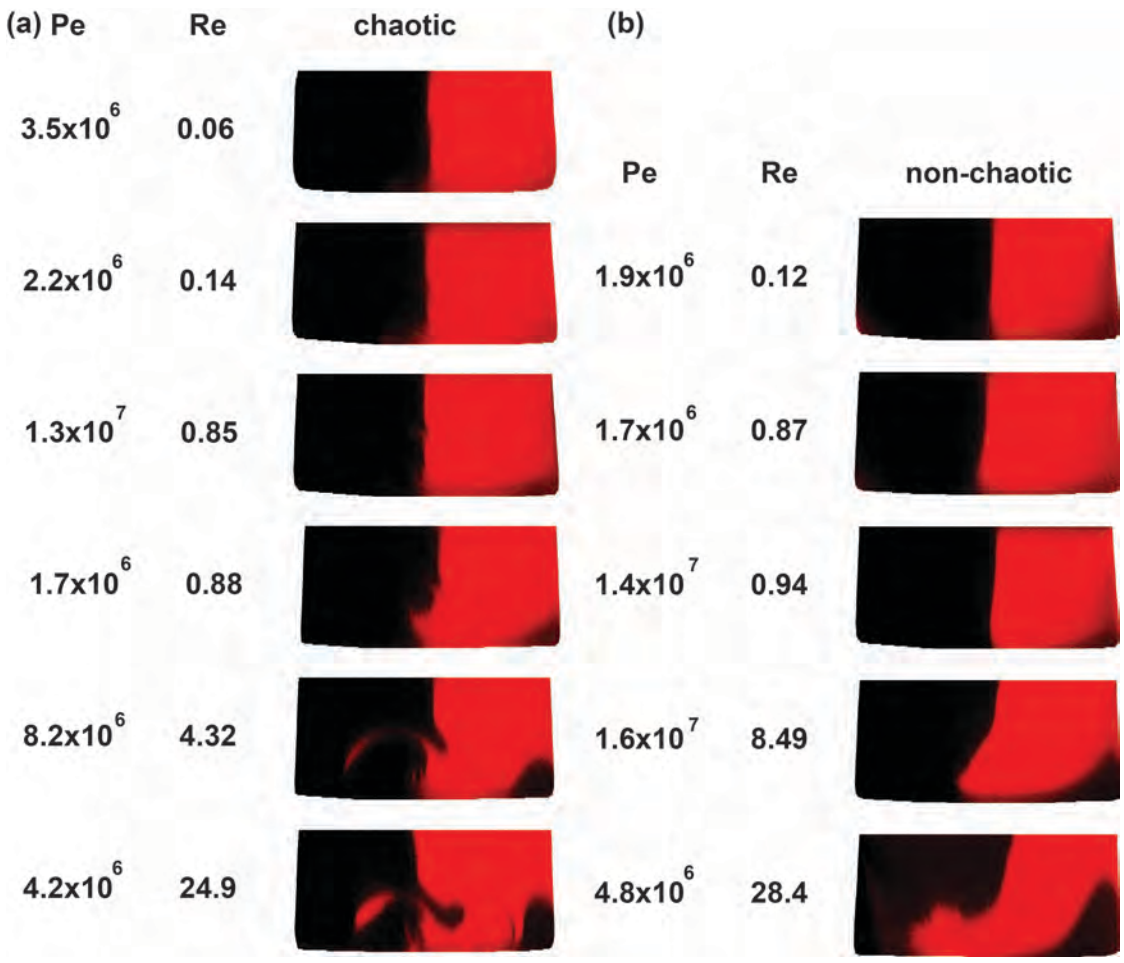


**Fig.4:** Inertial irreversibility in chaotic and non-chaotic flows. Concentration profiles of **(a)** chaotic inertial irreversibility and **(b)** non chaotic inertial irreversibility at high *Pe* as a function of increasing *Re* at the end of one cycle of stirring and un-stirring. Red color represents the solute.

Working in the high *Pe* regime, we attempt to decouple the effect of inertial irreversibility from convective diffusive irreversibility. Following the work by Flekkoy (19), we attempt to capture the effect of inertia. Varying *Re* over several decades, we find visible deviations arising from inertia in both chaotic and non-chaotic flow. We define f = (1 - *RF*) as the fraction of the solute that does not return to the original cross-sectional area. Figure 4 shows a summary of the inertial behavior for the two flows for 1 cycle of stirring and un-stirring. We notice that in the chaotic case, the deviations are found in several locations, and do not restrict themselves to the unstable manifold. We also note that experiment conducted at *Re* of 0.06, also has small indications of inertial irreversibility. However, we note that we cannot decouple the impact of slight geometric imperfections in the fore-aft symmetry from the inertial effects.

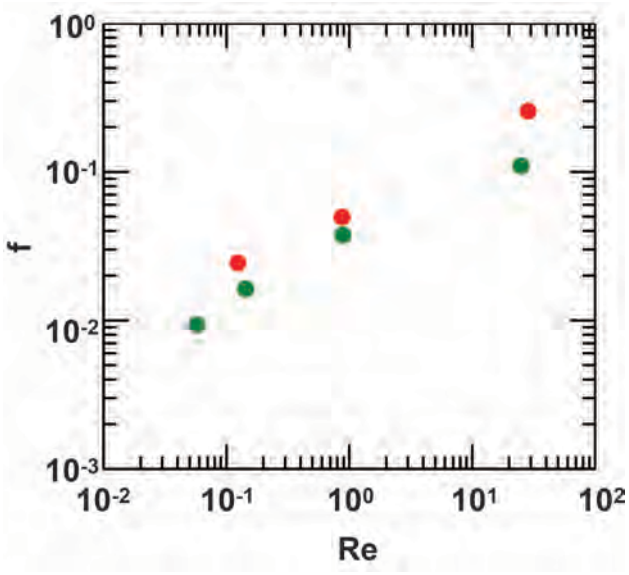


**Fig.5:** Inertial irreversibility in chaotic and non-chaotic flows: The fraction of solute that does not return to the original cross-sectional area *f* after one cycle of stirring and un-stirring in both chaotic and non-chaotic flows as a function of increasing *Re*. Green symbols represent chaotic flows. And red symbols represent non-chaotic flows.

Since the convective-diffusive irreversibility is negligible in this regime, we quantify the effect of inertia by measuring fraction of the total concentration of the solute that did not return to its

original position convectively in Figure 5. The key source of inertial reversibility in our flow is region of the channel where transverse flow switches from one to another. In the case of a chaotic flow, this switching happens every half cycle, when the pattern of staggered herringbone mixer changes [Fig 1(b)i]. In the non-chaotic flow, switching of the transverse flow occurs at the inlet, at mid plane and at the exit. At every instance of switching, there is a length $L_{trans} \propto ReH$ during which the transverse flow is developing. Understanding the impact of transience induced due to switching would be useful to quantify the effect of inertial reversibility on *RF*.

**Separation**

We have experimentally studied the behavior of one measure of reversal – return fraction (*RF*) and found that the modified Ranz model predicts the behavior of chaotic flows. Using the modified Ranz model, we can predict the separation efficiency achieved by the chaotic reversal process. Figure 6 is a plot of separation efficiency as a function of ratio of diffusivities obtained from the modified Ranz model for the chaotic (green) and the non-chaotic flow (red). In comparison, the separation efficiency curve (black) of the modified Ranz model indicates the maximum separation efficiency achievable for the given initial condition.

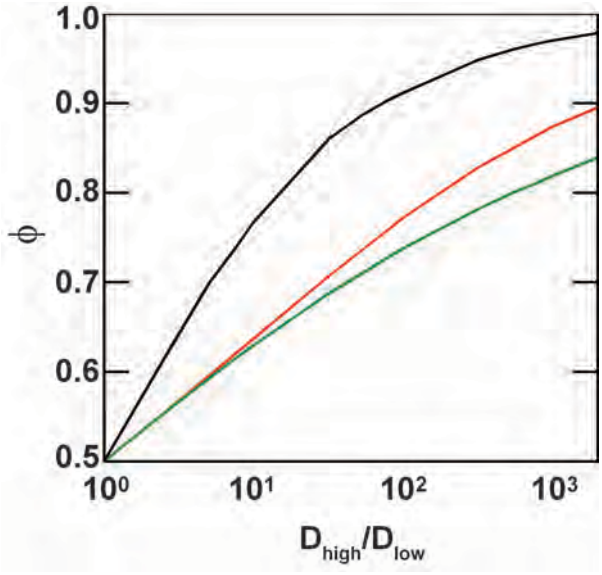


**Fig.6:** Separation efficiency in chaotic and non-chaotic flows using the modified Ranz model. Using the two fit parameters $\langle \dot{\gamma} \rangle = 0.939 T_{cyc}^{-1}, s_0 = 0.75h$ , we plot the separation efficiency of chaotic and non-chaotic flows based on the modified Ranz model as a function of the ratio of diffusivities. Green line represents the modified Ranz model for the chaotic flow. And red line represents the modified Ranz model for the non-chaotic flow. The black line represents the predictions of the Ranz model.

Further, to optimize the yield and the separation efficiency of the desired solute by passing the purified stream into separation device with new dilutant to achieve a high degree of separation. We would like to point that the channel flow with grooves is a proof of concept of the idea of SCDI. In order to make this technique, a practically viable one, we should find a flow that is closest to the Ranz model. We note that the chaotic baker's map is a flow with a single strain rate that achieves exponential stretching. Further, the SAR mixer introduced by Schoenfeld [23] is an implementation of chaotic baker's map. Thus, the design of SAR mixer can be used in the fore-aft symmetric format to develop a practically viable and technological useful separation device to achieve high return fraction with a high separation efficiency in a very short length scale.

***Conclusions***

In this study, we have shown proof of concept for a practical implementation of separation by convective diffusive irreversibility using the chaotic and non-chaotic stirring in a microfluidic channel. Further, we were able to validate the generality of modified Ranz model for chaotic using experiments and numerical simulations. We will match the rate of interfacial growth observed in the numerical simulation of chaotic and non-chaotic flows to show better comparison between the concentration profiles obtained in experiments. In the context of separation we used the modified Ranz model to predict the separation efficiency in these flows. Further, we probed the effect of inertia on reversibility of chaotic and non-chaotic flows. Our experimental results of inertial irreversibility in chaotic and non-chaotic flows might be a result of the irreversible transient flow whenever the transverse flow changes.

**References**


[1] G. I. Taylor, *Illustrated Experiments in Fluid Mechanics* (MIT Press Cambridge, 1972), p.47-54.

[2] J. P. Heller, American Journal of Physics **28**, 348 (1960).

[3] H. Aref, and S. W. Jones, Physics of Fluids A-Fluid Dynamics **1**, 470 (1989).

[4] W. E. Ranz, Aiche J. **25**, 41 (1979).

[5] P. Sundararajan, J.D. Kirtland, D.L. Koch and A. D. Stroock, Physical Review E **86,** (2012)

[6] V. Dolnik, S. R. Liu, and S. Jovanovich, Electrophoresis **21**, 41 (2000).

[7] R. Pethig, Biomicrofluidics **4**, (2010).

[8] S. Pedersen-Bjergaard, and K. E. Rasmussen, Anal. Chem. **71**, 2650 (1999).

[9] A. Wainright, S. J. Williams, G. Ciambrone, Q. F. Xue, J. Wei, and D. Harris, J. Chromatogr. A **979**, 69 (2002).

[10] M. A. M. Gijs, Microfluid. Nanofluid. **1**, 22 (2004).

[11] J. de Jong, R. G. H. Lammertink, and M. Wessling, Lab Chip **6**, 1125 (2006).

[12] J. P. Brody, and P. Yager, Sens. Actuator A-Phys. **58**, 13 (1997).

[13] A. D. Stroock, S. K. W. Dertinger, A. Ajdari, I. Mezic, H. A. Stone, and G. M. Whitesides, Science **295**, 647 (2002).

[14] A. D. Stroock, and G. J. McGraw, Philosophical Transactions of the Royal Society of London Series a-Mathematical Physical and Engineering Sciences **362**, 971 (2004).

[15] J. D. Kirtland, G. J. McGraw, and A. D. Stroock, Phys. Fluids **18**, 13 (2006).

[16] E. B. Brown, E. S. Wu, W. Zipfel, and W. W. Webb, Biophys. J. **77**, 2837 (1999).

[17] A. D. Stroock, S. K. Dertinger, G. M. Whitesides, and A. Ajdari, Anal. Chem. **74**, 5306 (2002).

[18] J. Happel, and H. Brenner, *Low Reynolds Number Hydrodynamics* (Prentice Hall Inc, Englewood Cliffs, 1965),

[19] E. G. Flekkoy, T. Rage, U. Oxaal, and J. Feder, Phys. Rev. Lett. **77**, 4170 (1996).

[20] P. Dutta, and R. Chevray, Experimental Thermal and Fluid Science **11**, 1 (1995).

[21] P. Dutta, and R. Chevray, J. Fluid Mech. **285**, 1 (1995).

[22] G. Haller, and T. Sapsis, Chaos **21** (2011)

[23] F. Schonfeld, V. Hessel, and C. Hofmann, Lab on a Chip **4**, 65 (2004).

# CHAPTER 4

# UNDERSTANDING MIXING IN THREE-DIMENSIONAL REVERSAL FLOWS

## *Introduction*

In the first three chapters, we have studied the interplay of convective diffusive irreversibility in a reversal process using the Ranz model. Separation by Convective Diffusive Irreversibility (SCDI) in a reversal flow is fundamentally a mixing problem. The Ranz model captures this similarity between mixing and SCDI by the observing that concentration evolution during stirring and un-stirring is equivalent to stirring for twice the mixing time $\tau_{stir}$. Finn et al [1] studied different measures of mixing and they note that *RF* and diffusive deviation after reversal of convective processes are measures of mixedness in a flow. We explored the behavior of RF extensively in the first three chapters. Here, we will apply the Ranz model and modifications to the Ranz model due to distribution of strain rates to other observables such as variance, and the evolution of distribution of concentration. We will use the same system of three dimensional chaotic and non-chaotic duct flows in Chapter 2 to predict the mixedness using the Ranz model and its modification due to strain rates.

## *Ranz model for mixing observables*

Variance or standard deviation is one of the most commonly used mixing observables. The strongest test of a mixing model is its ability to capture the complete evolution of distribution of concentration observed in the real flows. We will evaluate the evolution of variance and concentration distribution in the flows under consideration using the Ranz model.

**Variance**

When applied to the forward stirring process, the Ranz model predicts the decay of variance as given in Eq. (1) for a mixing time $\tau$ .

$$\sigma_s^{\,2} = \sum_n \frac{1}{(n\pi)^2} \sin^2\left(n\pi \frac{s_0}{\lambda_0}\right) \exp\left[-\left(2n\pi \frac{s_0}{\lambda_0}\right)^2 \tau\right] \qquad \ldots 1$$

We also calculate the prediction of the Ranz model for variance of the concentration profile after stirring and un-stirring. Following the calculations of the Ranz model for SCDI, we note that the variance at a mixing time of $2\tau$ [Eq. (2)] represents the variance at the end of un-stirring.

$$\sigma_{us}^{\,2} = \sum_n \frac{1}{(n\pi)^2} \sin^2\left(n\pi \frac{s_0}{\lambda_0}\right) \exp\left[-\left(2n\pi \frac{s_0}{\lambda_0}\right)^2 2\tau\right] \qquad \ldots 2$$

We expect the variance $\sigma_s^{\,2}$ to decrease during mixing. However, it is not intuitive to expect this prediction of the Ranz model that after stirring for $\dot{\gamma}t_{stir}$ and un-stirring for $\dot{\gamma}t_{un-stir}$, the strand width grows back to its original width whereas the variance $\sigma_{us}^{\,2}$ decreases to a value lower than $\sigma_s^{\,2}$, the variance after stirring for $\dot{\gamma}t_{stir}$. Nevertheless, the loss of variance during un-stirring occurs because the action is un-stirring is very much a convective-diffusive process. But, the loss of variance $\sigma_{us}^{\,2} - \sigma_s^{\,2}$ is much lesser compared to the variance $\sigma_s^{\,2}$ after stirring. To appreciate the details of the Ranz prediction for variance, we plot $\sigma_s^{\,2}$ and $\sigma_{us}^{\,2}$ as a function of transverse strain, $\dot{\gamma}t_{stir}$ at the end of stirring for extensional [Fig. 1(a)] and simple shear flows [Fig. 1(c)]. The effective forward stirring time corresponding to $\sigma_{us}^{\,2}$ can be evaluated using the $\sigma_s^{\,2}$ vs $\dot{\gamma}t_{stir}$ (blue) curve as shown in the Figure 1(a) and Figure 1(c). To visualize the extent of mixedness at these transverse strains, we included the concentration profiles after stirring, and

after un-stirring in the chaotic (extensional, Fig. 1(a-b)) and non-chaotic flows (simple shear, Fig. 1(c-d)) with the same transverse strain as the blue and green squares on these plots. Note that the variances of the concentration profiles in the inset are not plotted on the graph. In Figure 1(b) and 1(d), we plot the master curve for variance. The variance corresponding to stirring and un-stirring fall on the same curve at $\tau$ and $2\tau$.

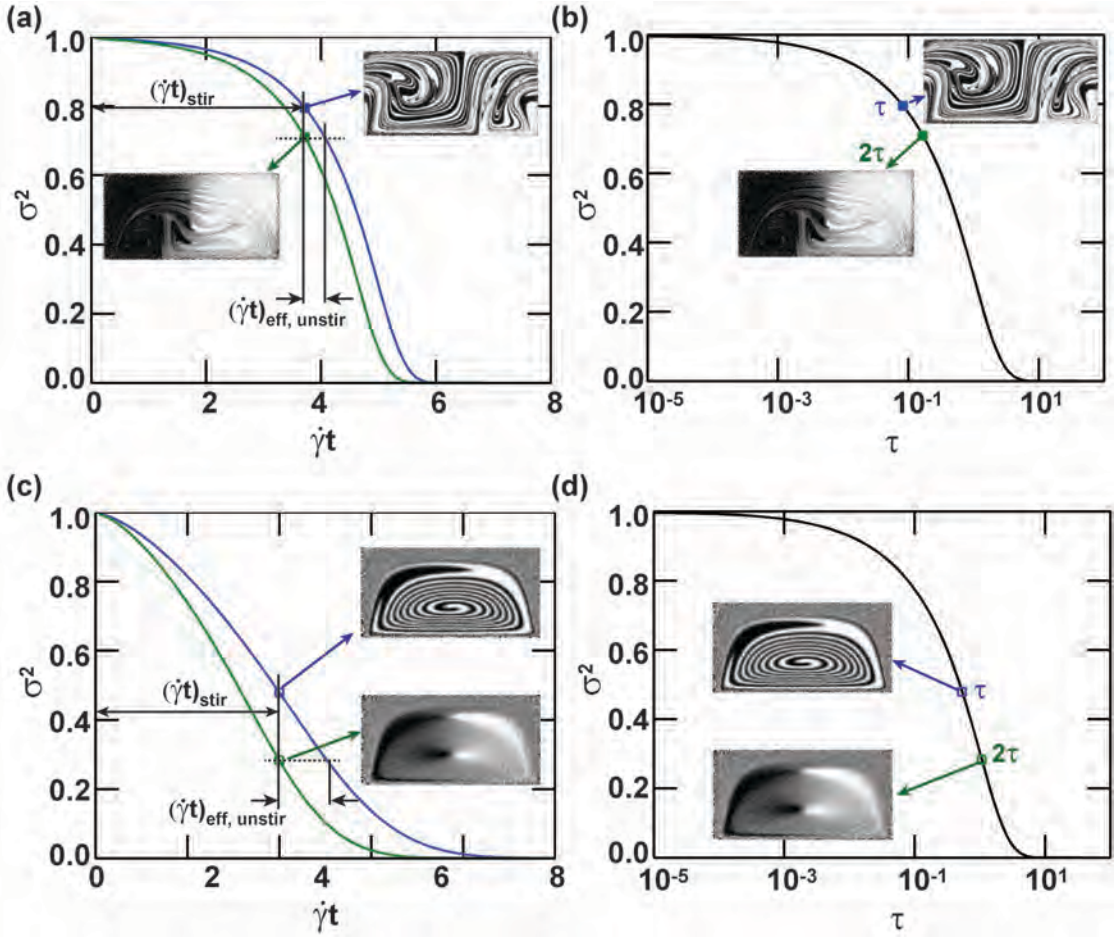


**Fig. 1:** Ranz model: Stirring and un-stirring – equivalent to mixing **(a)** Plot of variance at the end of stirring (blue) and variance at the end of stirring and un-stirring as function of the strain achieved during the forward stirring in an extensional flow. Using the plot we can observe the variance lost during un-stirring, and the effective strain that represents un-stirring. The insets show the concentration profiles in the chaotic flow after stirring for $\dot{\gamma}t = 3.72$ (blue square), and after stirring for $\dot{\gamma}t = 3.72$ and un-stirring for $\dot{\gamma}t = 3.72$ (green square) **(b)** Plot of variance as a function of mixing time $\tau$ .We observe that the variance at the end of stirring and the variance at the end of un-stirring fall on the same curve. **(c)**

Plot of variance at the end of stirring (blue) and variance at the end of stirring and un-stirring as function of the strain achieved during the forward stirring in a simple shear flow. The insets show the concentration profiles in the non-chaotic flow after stirring for $\dot{\gamma}t = 40$ (blue square), and after stirring for $\dot{\gamma}t = 40$ and un-stirring for $\dot{\gamma}t = 40$ (green square). **(d)** Plot of variance as a function of mixing time $\tau$ .The concentration profiles are shown to understand the loss of variance during un-stirring, although the variance might not be exactly predicted by the Ranz model.

In systems with high strains, evaluating the variance from the concentration profiles can be misleading, if the strand widths are lower than the bin widths. The Ranz model gives a prediction of strand width, and the modified Ranz model can used to predict the evolution of distribution of strand width. When a significant population of the strands has width less than the resolution of the concentration profiles, then the variances should be evaluated from such concentration profiles. However, evaluating the variance after stirring and un-stirring does not suffer from the malady of pixel resolution at moderate resolution of concentration profiles. Thus, the study of scalar variance after stirring and un-stirring is a valuable tool for accurately evaluating trends in variance evolution in flows with high strains.

**Concentration distribution**

As mentioned earlier, the strongest test of a mixing model is its ability to capture the complete evolution of distribution of concentration observed in the real flows. Given the simplicity of the model and its modifications, we do not expect the model to capture all the features of the concentration evolution. However, this test could point to the important flow characteristics that complete the model.

The distribution of concentration using the Ranz model is evaluated as the fraction of space occupied by solutes at concentration between *(c, c+dc)* [Eq. (3)].

$$p\left(c(\tau)\right)_R dc = \int_{c\in(c,c+dc)} \frac{d\xi}{2} \qquad \ldots 3$$

With $dc \to 0$, and using the symmetry of $c$ about $\xi = 0$, the distribution becomes

$$p(c(\tau))_R = \left|\frac{d\xi}{dc}\right| \text{ with } \xi \in [0,1] \qquad \ldots 4$$

Eq. (4) can be used to obtain analytical expressions for the distribution for sinusoidal initial concentration profile. However, it is simpler to evaluate the distribution using Eq. (3). For the modified Ranz model, the distribution is obtained using Eq. (5) below.

$$p\left(c\left(\tau_{\langle\dot{\gamma}\rangle}\right)\right)_{MR} = \int p(c)_R \, f(\dot{\gamma}) d\dot{\gamma} \qquad \ldots 5$$

We have described the Ranz model and its modifications for understanding the behavior of the flow in understanding SCDI, as well as understanding the mixing characteristics. We now turn to comparing the results of the model with the numerically simulated flow.

***Results and discussion***

As described in the model section, the Ranz and the modified Ranz model can be easily applied to variance. Figure 2 (a) and 2(c) are plots of variance obtained from numerical simulation as a function of the mixing time for the chaotic and the non-chaotic flow respectively. The plots include the variance at the end of stirring and variance at the end of stirring and un-stirring for both flows. We observe that in chaotic case, the variance at the end of stirring is lesser than the variance at the variance at the end of un-stirring. This is impossible since diffusion is irreversible. This is an artifact due to the following: a) unclear resolution of the interface, and b) strand width much less than the bin width. By the end of five cycles $(\gamma t = 3.72)$ in the chaotic flow, the mean strand width based on the Ranz model is the bin size. However, in the non-chaotic flow, the mean strand width (Ranz model) is equal to bin size at about 60 cycles at which point the normalized variance is 0.2 for a diffusivity of $8 \times 10^{-6}\left[H^2/T_{cyc}\right]$. Hence in the

comparison of the variance of chaotic flow with the modified Ranz prediction, we plot variance at the end of stirring and un-stirring from the numerical simulation in figure 2(b). Once again, like *RF*, we find that variance exhibits greater deviation from the modified Ranz model at large mixing times. In the case of the non-chaotic flow, we plot both the variance at the end of stirring, and variance at the end of un-stirring in figure 2(d) and find that they compare well with the modified Ranz model. We note that the strand width fit parameter changes from $s_0 = 2.35$ for *RF* to $s_0 = 1.1$ for variance. This difference in the strand width fit parameter arises because the *RF* is defined based on ratio of axial fluxes, whereas the variance is obtained from the concentration distribution. In conclusion, this study of variance brings out the observation made by the Ranz model that stirring and un-stirring is equivalent to mixing for $2\tau_s$, and that the reversal process is a promising tool to study mixing.

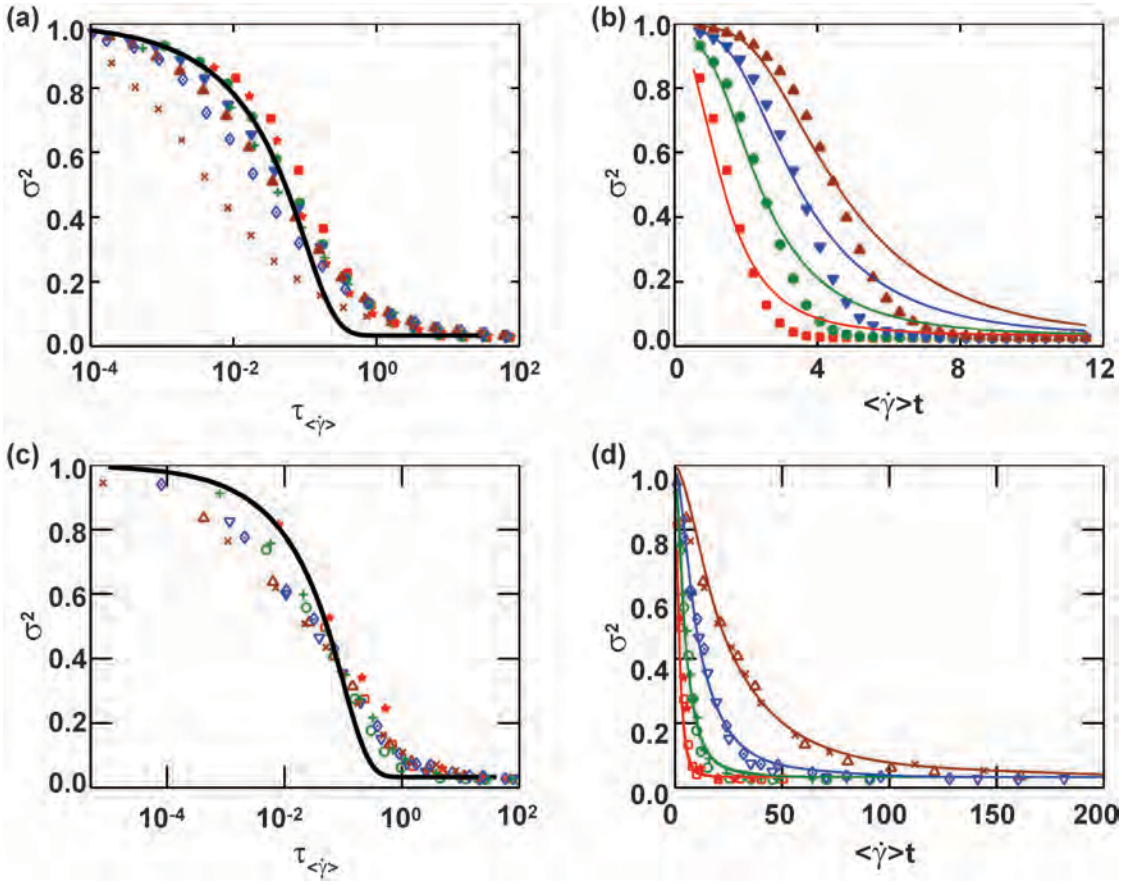

**Fig. 2:** Mixing in a reversal process: **(a)** Comparison of variance obtained from numerical simulation at the end of stirring, and at the end of un-stirring as a function of the respective mixing times $\tau_{<\dot{\gamma}>}$ in the chaotic flow with the prediction of variance by the Ranz model. **(b)** Comparison of variance at the end of stirring and un-stirring with the modified Ranz model based on the fit of the distribution to strain rates as a function of strain in the flow. The fit parameters $\langle\dot{\gamma}\rangle, s_0$ [0.744 $T_{cyc}^{-1}$, 1.05 H]. **(c)** Comparison of variance obtained from numerical simulation at the end of stirring, and at the end of un-stirring as a function of the respective mixing times $\tau_{<\dot{\gamma}>}$ in the non-chaotic flow with the prediction of variance by the Ranz model.**(d)** Comparison of variance both at end of stirring and at the end of stirring and un-stirring with the modified Ranz model based on the distribution to strain rates as a function of strain in the flow. The fit parameters $\langle\dot{\gamma}\rangle, s_0$ are [0.8 $T_{cyc}^{-1}$, 1.1 H]. The lines represent the modified Ranz model at different diffusivities.(red – $8x10^{-3}$, green – $8x10^{-4}$, blue– $8x10^{-5}$, brown– $8x10^{-6}$). Variance at the end of stirring for the different diffusivities are represented by (red star – $8x10^{-3}$, green plus(+) – $8x10^{-4}$, blue diamond – $8x10^{-5}$, brown cross – $8x10^{-6}$) and variance at the end of un-stirring by (red square – $8x10^{-3}$, green circle – $8x10^{-4}$, blue inverted triangle – $8x10^{-5}$, brown upright triangle – $8x10^{-6}$). The initial condition is the solute fills the right half of the cross-section.

We now look at the evolution of distribution of the concentration after un-stirring. The comparison of the modified Ranz and Ranz model with the results from numerical simulation is shown in figure 3(a) for chaotic flows, and figure 3(b) for non-chaotic flows. We observe that the Ranz model predicts the behavior of chaotic flows better than the modified Ranz model. The central feature of the concentration distribution in the chaotic flow is the shifting of the peaks of concentration profiles centered at $c$= 0 and $c$=1 towards intermediate values of concentration (between 0 and 0.5 for one peak, and between 0.5 and 1 for the other peak) before finally merging with a single peak at $c$=0.5. Whereas, the modified Ranz model predicts that the concentration distribution evolves through a stage with three peaks centered at c=0, c=0.5 and c=1 which is not seen in the evolution of the concentration field in the chaotic case. We find that the Ranz model predicts the behavior more closely than the modified Ranz model. In the non-

chaotic case in figure 3(b), the modified Ranz model with 3 peaks in the concentration profile predicts the behavior of the concentration field fairly well.

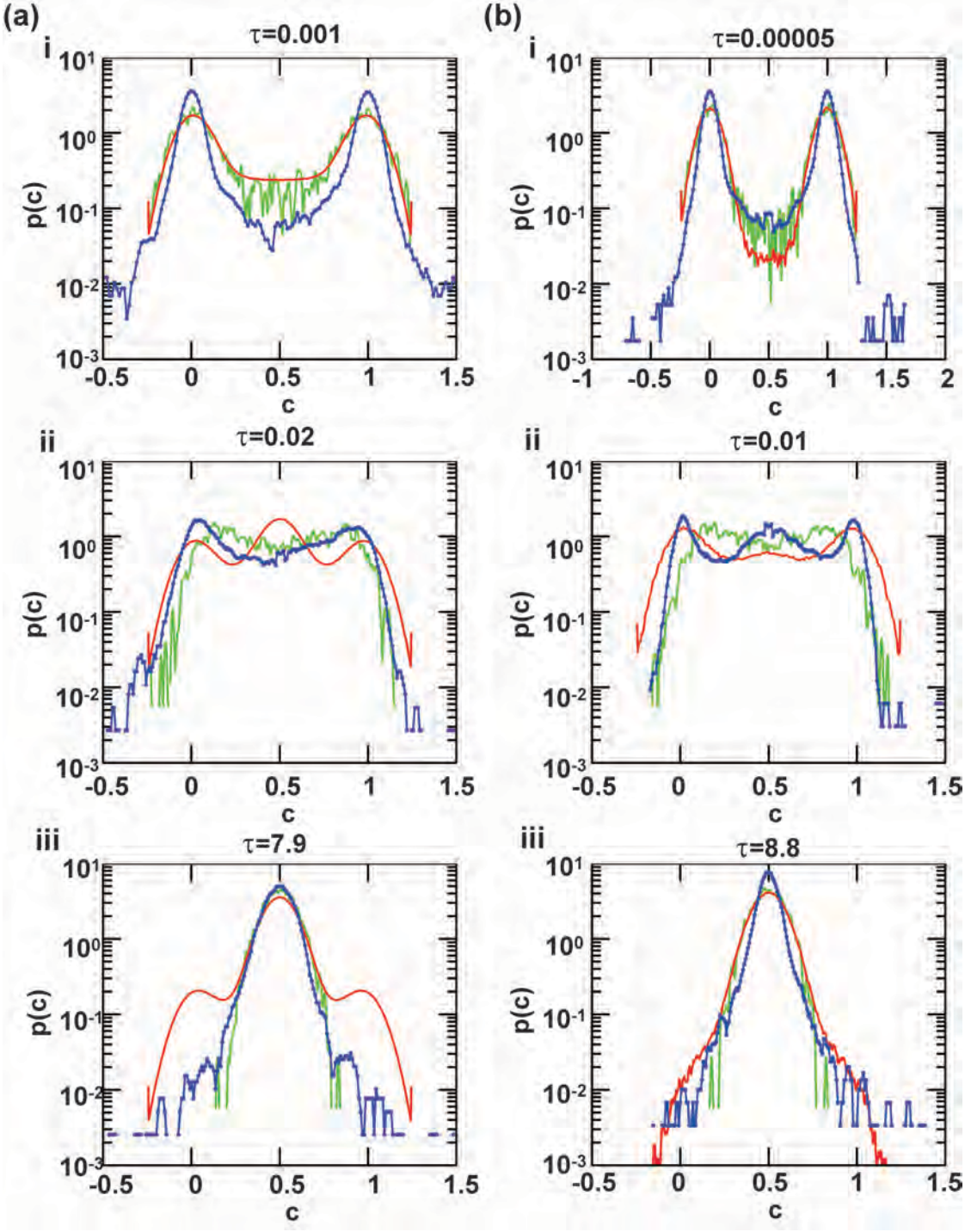


**Fig. 3:** Distribution of concentration in a reversal process: **(a-b)** Comparison of concentration distribution obtained from numerical simulation (blue dots) at the end of stirring and un-

stirring with Ranz (green line) and modified Ranz model based on fit of the distribution of strain $\tau_{<\dot{\gamma}>}$ (red line) in the (a) chaotic flow (b) non-chaotic flow.

In the chaotic case, the distinction between the modified Ranz model and the numerical simulation could arise from one of following possibilities: a) The additional source for the observed strand width distribution is the folding process. In the Ranz and the modified Ranz model we assume perfect local periodicity of the strands i.e,uniform $s_0/\lambda_0$ instead of a distribution of $s_0/\lambda_0$ as can be observed in the concentration profiles after mixing. The process that creates the distribution of $s_0/\lambda_0$ is the non-linear stretching [near the point of asymmetry of the cross sectional flow $(r=1/3, r=2/3)$], and folding which is a prominent feature of the chaotic mixing process. b) Random merging model: Random merging of strands in concentration space as suggested by Villermaux [3] who showed that the probability of concentration extracted from theory of random merging can predict the intermediate and late time behavior of forward mixing. c) Effect of boundaries as suggested by Lebedev & Turitsyn, Chertkov & Lebedev [4-5], and Simonnet & Groisman [6]. However, we observe that the models described in b) and c) cannot be used to treat the reversal process for understanding irreversibility.

***Conclusion***

We have studied the process of separation by convective diffusive irreversibility and shown that the reversal process can be treated as a mixing process. Using the Ranz model, we found that linear flows exhibit a universal decay in reversibility and mixing when viewed in the mixing time domain. The study of variance, distribution of concentration points to the usefulness of studying these quantities in a reversal process relative to the mixing process. Qualitative

differences in the prediction in the evolution of concentration distribution by the modified Ranz model and the results from numerical were observed, especially for chaotic flows. Our adaptation of the linear flow model captures the average characteristics of chaotic and non-chaotic flows, but failure to include the non-linear processes prevents it from capturing the details of the mixing process in a chaotic flow.

## References


[1] M. D. Finn, S. M. Cox, and H. M. Byrne, Journal of Engineering Mathematics **48**, 129 (2004).

[2] W. E. Ranz, Aiche J. **25**, 41 (1979).

[3] E. Villermaux, A. D. Stroock, and H. A. Stone, Phys. Rev. E **77**, 4 (2008).

[4] V. V. Lebedev, and K. S. Turitsyn, Physical Review E **69**, 11 (2004).

[5] M. Chertkov, and V. Lebedev, Physical Review Letters **90**, 4 (2003).

[6] C. Simonnet, and A. Groisman, Physical Review Letters **94**, 4 (2005).